AN ABSTRACT OF THE DISSERTATION OF

Esteban Bowles-Martinez for the degree of Doctor of Philosophy in Ocean, Earth, and Atmospheric Sciences presented on March 21, 2019.

Title: Magnetotelluric Studies of Tectonic Systems and Volcanic Areas of North America

Abstract approved: _____

Adam Schultz

Magnetotellurics is used in two geologic settings on scales ranging from 1000-km tectonic structures to local features hundreds of meters wide. These areas are the Midcontinent Rift System (MRS) and its related mantle plume in the northern Midwestern United States and Newberry Volcano in central Oregon.

The MRS study uses MT data to image structures of the midcrust to the upper mantle. In addition to the rift, an elongated conductor is present at the base of the lithosphere, interpreted as the hot spot track from the mantle plume that initiated rifting. This track terminates in southern Wisconsin at the 1.8-1.7 Ga Yavapai-Mazatzal accretion that was contemporaneous with a major change in the chemistry of subducted material. During this time, conductive sediment rich in metallic sulfide minerals that recorded a change in global ocean chemistry from iron-saturated to sulfur-saturated during the Proterozoic Great Oxygenation Event was deposited on the seafloor. Melting of sediment rich in metallic sulfide minerals during the onset of the Keweenaw mantle plume that initiated the MRS in western Lake Superior enabled interconnection of disseminated sulfide crystals to produce a hot spot track at upper lithospheric depths

that are in agreement with melting depths and temperatures inferred from petrologic studies of syn-rift flood basalts. The hot spot's location shows that pre-Yavapai accretion subduction was north-dipping and low-angle.

The Newberry work shows that magma within the caldera is unusually resistive and therefore must be felsic and dry if it is to agree with seismic models and with the petrology of recent eruptions. Using seismic and petrological constraints, we find that the magma reservoir has no more than 8.7% partial melt. A major component of the volcano's hydrothermal system is expressed along the caldera's south rim as a vertical conductive anomaly reaching from the magma chamber to the vent that produced the most recent eruption.

Magnetotelluric Studies of Tectonic Systems and Volcanic Areas of North America

by
Esteban Bowles-Martinez

A DISSERTATION

submitted to

Oregon State University

in partial fulfillment of
the requirements for the
degree of

Doctor of Philosophy

Presented March 21, 2019
Commencement June 2019

Doctor of Philosophy dissertation of Esteban Bowles-Martinez presented on March 21, 2019

APPROVED:

Major Professor, representing Ocean, Earth, and Atmospheric Sciences

Dean of the College of Earth, Ocean, and Atmospheric Sciences

Dean of the Graduate School

I understand that my dissertation will become part of the permanent collection of Oregon State University libraries. My signature below authorizes release of my dissertation to any reader upon request.

Esteban Bowles-Martinez, Author

ACKNOWLEDGEMENTS

I express my sincere appreciation to all of the people involved in putting me on a trajectory toward becoming a geophysicist. I am especially grateful for my parents Jenifer and Gene and sisters Alyssa and Jessica for supporting and encouraging me through my entire life. I am also grateful for the faculty at OSU who have helped me along the way, especially my advisor Adam Schultz and the lab managers Brady Fry and Tristan Peery. I am also grateful for faculty at other institutions who showed me how wonderful geophysics is before I came to OSU, especially George Jiracek at San Diego State University and Phil Wannamaker at University of Utah. I appreciate the chance I had to do over 600 days of OSU field work in interesting places with many excellent people, including Eric Kazlauskas, Katie Decker, Matt Cosatt, Drew Thomas, Jessica Bowles-Martinez, Dan Masters, Travis Fultz, Margie Cording, Dylan Collins, Kyle McDonald, Corey League, Tom Bonofiglio, Jon Powell, Hilary Ross, Gerald Buxton, William McNichols, Luke Blom, Ben Bloss, Kevin Mendoza, Taryn Bye, L Roy Bonner IV, Emily Hart, Beth Burton, Bryce Neal, Rebeca Gurrola, and Kate Scholz. This work benefited from conversations with many other scientists, including Gary Egbert, Shan de Silva, Naoto Imamura, Anna Kelbert, Ben Heath, Naser Meqbel, Ninfa Bennington, Paul Bedrosian, Kerry Key, Bo Yang, Ben Murphy, Nopsiri Chaiyo, Andrew Meigs, Andrew Thurber, Rick Colwell, Marty Fisk, Kellie Wall, and Jared Peacock. I also thank my previous employer Zonge International and especially the legendary crew chief Mark Reed for patiently setting an example of how to lead difficult field campaigns with maximum safety and efficiency. Finally, I want to thank my friends in Oregon who have made this a great place to spend the last six years.

I gratefully acknowledge the support of the following research grants and contracts: For work at Newberry Volcano, US Department of Energy funding via URS/AECOMM Subcontract No. RES1100426/Task Release 4 “Novel Use of 4D Monitoring Techniques to Improve Reservoir Longevity and Productivity in Enhanced Geothermal Systems”. For work at the Mid Continent Rift System, National Science Foundation Grant EAR-

1147970 “Collaborative Research: Geophysical investigation of the Mid-Continent Rift system”.

This work used data from the USArray MT TA project, led by PI Adam Schultz and Gary Egbert. They would like to thank the Oregon State University MT team and their contractors, lab and field personnel over the years for assistance with data collection, quality control, processing and archiving. They also thank numerous districts of the U.S. Forest Service, Bureau of Land Management, the U.S. National Parks, the collected State land offices, and the many private landowners who permitted access to acquire the MT TA data. USArray TA was funded through NSF grants EAR-0323311, IRIS Subaward 478 and 489 under NSF Cooperative Agreement EAR-0350030 and EAR-0323309, IRIS Subaward 75-MT under NSF Cooperative Agreement EAR-0733069 under CFDA No. 47.050, and IRIS Subaward 05-OSU-SAGE under NSF Cooperative Agreement EAR-1261681 under CFDA No. 47.050.

TABLE OF CONTENTS

Page

TABLE OF CONTENTS (Continued)

Page

TABLE OF CONTENTS (Continued)

Page

LIST OF FIGURES

LIST OF FIGURES (Continued)

Figure Page

DEDICATION

To Noyna Chaiyo, whose kindness and intelligence made me a better scientist and a better person. I will always be thankful that we were a part of each other's lives.

แด่น้อยหน่าผู้ที่อ่อนโยนและเป็นคนที่ฉลาดทั้งสติและปัญญา

น้อยหน่าทำให้ผมเป็นนักวิทยาศาสตร์และคนที่ดี

ขอบคุณในชีวิตนี้ที่เราเป็นส่วนหนึ่งของกันและกัน

Chapter 1: Introduction and overview

The Earth can be described by its inductive response to the time-varying geomagnetic field using the magnetotelluric (MT) geophysical method. This information tells us about the electrical resistivity of the subsurface, but that is only the first step in determining the contents of the Earth's interior. During my doctoral studies I have worked on many projects that are united by their use of this geophysical method to answer geologic questions. These projects focus on different regions of the lithosphere at different scales, from as small as hundreds of meters to study individual features within a single volcano, to hundreds of kilometers to study the relationship between large-scale tectonics and one of the largest volcanic eruptions in Earth's history. Throughout this dissertation I emphasize the importance of not relying on MT alone in making geologic interpretations. I demonstrate that when interpreting a resistivity anomaly, it is crucial to consider a variety of other geophysical, tectonic, and petrological information.

In this dissertation I will describe two of my studies. The first study is an investigation of Newberry Volcano in central Oregon, where I use seismic and petrological information to challenge the usual interpretation of magma as a low-resistivity target. I also use MT to image a conductive anomaly that is a key piece of Newberry's hydrothermal system. The second study is an investigation of the remnants of an ancient mantle plume in the Midwestern United States, a region that has been tectonically stable for over one billion years, yet still appears as a clear high-conductivity anomaly. Explaining its continued existence requires a consideration of how fundamental Earth processes were different at the time of rock formation compared to the present.

I introduce the physics of MT in a chapter that was accepted for publication in an American Geophysical Union monograph on space weather and geomagnetically induced currents as an infrastructure hazard, titled "Geomagnetically Induced Currents from the Sun to the Power Grid." This chapter was written to introduce scientists in other fields to MT, describing the entire workflow from the basic physics of the method to making geologic interpretations. It was written from a perspective that it is important to

understand and mitigate the risk that geomagnetically-induced currents pose to electrical infrastructure. Minor modifications have been made to adapt it to better fit the contents of this dissertation.

In subsequent chapters are two articles on the aforementioned geophysical studies. The Newberry Volcano chapter and the Keweenawan mantle plume chapter will both be submitted to Journal of Geophysical Research. Additional details of data and misfits are given in appendices.

In addition to the work presented here, a large portion of my doctoral research has been on an intermediate scale study of a volcanic region in the southern Washington Cascades with colleagues at the United States Geological Survey. The major results of this study were published in a Nature Geoscience article called “Crustal inheritance and a top-down control on arc magmatism at Mount St Helens” By Paul Bedrosian, Jared Peacock, Esteban Bowles-Martinez, Adam Schultz, and Graham Hill (Bedrosian et al., 2018). Research for this project is ongoing, and I am currently preparing a manuscript describing secondary features including a previously unknown extension of the West Rainier Seismic Zone and the potential for renewed magmatism between Mount Rainier and Mount Adams.

I am also preparing a manuscript on a second study at Newberry volcano. Instead of a geologic investigation, this study uses MT to monitor the movement of injected water in an enhanced geothermal system on the west flank of Newberry. Unlike traditional MT, this monitoring method uses time-series analysis of the electric and magnetic field vectors that are the fundamental elements of MT data. This type of analysis is necessary in settings where noise is so strong that the MT impedance tensor cannot be reliably determined for the frequencies of interest. The work in the Newberry geothermal monitoring study builds on a CO_2 injection and storage monitoring study for the United States Department of Energy (DOE), in which I emphasized the characteristics of each component of the MT impedance tensor that change as a fluid reservoir grows. This was presented in a DOE report titled “A Multisensor Plume Monitoring Schema for

Carbon Sequestration Sites in Subsurface Engineered-Natural Systems” by Paul Vincent, Esteban Bowles-Martinez, and Adam Schultz (Vincent et al., 2018).

The three articles presented in this dissertation show how measurements of the Earth’s electromagnetic signals reveal the internal structure of the Earth, focusing on volcanic regions. What I will show is the importance of relying on more than just one method of analysis, the importance of considering long-term changes in Earth processes, and that the best results come from a synthesis of all available data.

Geomagnetically Induced Currents from the Sun to the Power Grid

Esteban Bowles-Martinez and Adam Schultz

American Geophysical Union Monograph Series

2000 Florida Avenue N.W. Washington, DC 20009-1227 USA

Chapter 2: Geomagnetically Induced Currents from the Sun to the Power Grid

2.1 Abstract

The electric power transmission infrastructure is exposed to hazards from geomagnetically induced currents (GIC) in the Earth. We review the theory of geomagnetic induction and how electromagnetic (EM) signals measured on the surface are used to create magnetotelluric (MT) impedance tensor data, which describe how the relationship between the electric and magnetic fields measured on the Earth's surface depends on the Earth's internal electrical conductivity. MT data are usually used to create subsurface resistivity models from which geologic interpretations are made, but they can also be used to predict ground electric fields induced by disturbances to the geomagnetic field, such as those produced by a solar coronal mass ejection. This chapter describes the complete MT workflow with attention to GICs, including the basic theory and physics of MT, instrumentation, data acquisition, data processing, inversion, and geologic interpretation of resistivity models.

2.2 Introduction

The relationship between Earth's electric and magnetic fields can be used to determine the electrical properties of the subsurface (Cagniard, 1953; Tikhonov, 1950) This chapter introduces the magnetotelluric (MT) geophysical method, which is used to create electrical resistivity models of the Earth's interior as well as for modeling electric fields related to geomagnetically induced currents (GICs). Thorough reviews of magnetotellurics are provided by Ward and Hohmann (1988), Vozoff (1991), Simpson and Bahr (2005), Chave and Jones (2012), and Zhdanov (2017). MT employs the principle of electromagnetic induction where the Earth's time-varying magnetic field (H) produces an electric field (E) within the conductive materials of Earth's interior. These signals are analyzed in the frequency domain over a spectrum that typically ranges from tens of kHz to sub-mHz, with lower-frequency signals corresponding to greater depth of penetration into the Earth's subsurface. This broad frequency range allows the crust

and upper mantle to be investigated. This chapter provides an introduction to MT by covering the following topics: the physics of geoelectromagnetic induction, how electromagnetic (EM) signals are used in MT, data acquisition, data processing and inversion, and a brief overview of resistivity model interpretation.

Estimating ground-level electric fields for GIC hazard assessment requires measuring electromagnetic (EM) signals with specialized instruments and converting the electric and magnetic field data to MT data in the frequency domain. MT data are typically represented as the impedance tensor Z, a frequency dependent 2×2 matrix that relates electric and magnetic fields through the equation E=ZH. The mapping between inducing magnetic fields and induced electric fields depends on the volumetric variations in subsurface electrical conductivity (see section 2.4.3 for more information on the impedance tensor). Data acquisition must be on a time-scale—and therefore within a frequency band—of relevance to the natural signal content of space weather events that are known to impact the power grid. Broadly speaking, to monitor the response to geomagnetic disturbances associated with GICs, current practice suggests that MT impedances are required over a frequency band spanning approximately 10^{-4} Hz – 10^{-1} Hz. Such a band yields information of adequate spatial resolution on electrical conductivity structure from mid-crustal depths (~10 km below ground surface) to the upper mantle (~300 km depth), depending on the vertically integrated conductivity (conductance) of the overburden. While such data have reduced resolving power at shallow crustal depths, they remain sensitive to the conductance from the surface to the upper mantle, as well as to unresolvably fine-scale, near-surface galvanic scattering or distortion effects that impact the electric field. Obtaining MT data in the aforementioned frequency band is the province of long-period MT, typically, although not exclusively, obtained by combining observatory-quality triaxial fluxgate magnetometer measurements of the magnetic field with horizontal electric dipole measurements, typically at a sample rate of 1-10 samples per second.

Through the impedance tensor, GICs can be predicted from magnetic field measurements. Space weather events that cause geomagnetic disturbances (GMDs)

strong enough to produce dangerous GICs are a rare occurrence, but occur frequently enough and with high enough potential for infrastructure damage that it is important to predict their effects using MT data. The earliest and strongest GMD known to affect infrastructure occurred in 1859, causing damage to telegraph systems (Boteler, 2006; Carrington, 1859; Shea & Smart, 2006), with other significant events in 1989, 1972, 1958, 1940, 1921, and 1872 (Boteler, 2001; Silverman, 2006). There is also current interest in the problem of intense, but geographically more localized GMDs and related GICs induced by exo-atmospheric detonation of nuclear devices, also called electromagnetic pulse (EMP) weapons. The signal produced by an EMP weapon has three stages (Foster et al., 2004). The first, or E1 stage, occurs as a high-amplitude impulsive EM energy burst within the first nanoseconds after detonation and is capable of damaging electronic devices. The intermediate E2 stage follows within the first second, with lower amplitude energy and an effect similar to a weak but widespread lightning strike affecting an area thousands of kilometers wide (Foster et al., 2008). The final stage, E3, lasts for a minute or more and rather than propagating as an electromagnetic wave, it results from distortions to the Earth's magnetic field caused by the nuclear detonation, inducing currents that can damage infrastructure in an area about half as wide as the E2 stage (Foster et al., 2008). The frequency range of the E3 stage of these disturbances requires the use of EM signals that extend to higher frequencies than those created by GMDs, generally in the band of 10^{-3} Hz – 10^{3} Hz, and that involves electromagnetic inductive responses in the upper ~10 km of the Earth's crust as well as in the deeper crust and upper mantle. By using instruments sensitive to this frequency range, the same methods used for estimating ground electric fields from GMDs can be applied to these artificially induced signals.

2.3 The Magnetotelluric Method

2.3.1 EM induction in the Earth

Electric and magnetic fields within the Earth, like elsewhere, are governed by Maxwell's equations. In MT, the range of frequencies used and assumptions about the plausible range of the electrical conductivity of geologic materials under crust and upper mantle

conditions allow us to simplify the relationships between the fields. Variables and units are defined in Table 1. The reduced governing equations for MT are therefore Faraday's Law:

$$\nabla \times \mathrm{E} = -\mu_0 \frac{\partial \mathrm{H}}{\partial \mathrm{t}}.$$

Equation 1

and Ampere's Law:

$$\nabla \times \mathrm{H} = \sigma \mathrm{E} + \varepsilon_0 \frac{\partial \mathrm{E}}{\partial \mathrm{t}}.$$

Equation 2

In this text, we will refer to the magnetic field H with units of V/m rather than magnetic flux density B, which is equal to μ_0 H and has units of Teslas. We will also neglect small differences in permeability μ, which varies only by parts per thousand for most materials, whereas conductivity varies by orders of magnitude. We therefore assume free space permeability ($\mu = 4\pi \cdot 10{-}7$ H/m) for all cases for the remainder of this chapter.

We will also use Gauss's law to relate electric field divergence with charge density β:

$$\nabla \cdot \mathrm{E} = \frac{\beta}{\varepsilon_0}.$$

Equation 3

Faraday's Law Equation 1 shows that a time-varying magnetic field produces a circulating electric field in a plane orthogonal to the magnetic field. Similarly, Ampere's law Equation 2 shows that a circulating magnetic field is produced by an electric current and/or a time-varying electric field.

Taking the curl of both sides of Equation 1, we have:

$$\nabla \times (\nabla \times \mathrm{E}) = -\mu \frac{\partial}{\partial \mathrm{t}} (\nabla \times \mathrm{H}).$$

Equation 4

Applying the curl of curl vector identity to the left-hand side gives:

$$\nabla \times (\nabla \times \mathrm{E}) = -\nabla^2 \mathrm{E} + \nabla(\nabla \cdot \mathrm{E}).$$

Equation 5

Using Equation 3 and assuming charge density β is uniform, the final term of Equation 5becomes zero. The derivation shown in equations 4 through 7 describe a homogeneous medium, where charge density is uniform, though this is not necessarily true in realistic environments that may have gradients in the conductivity of materials. Returning to Equation 4 and substituting Equation 2 on the right-hand side, we now have:

$$\nabla^2 \mathrm{E} = \mu \sigma \frac{\partial \mathrm{E}}{\partial \mathrm{t}} + \mu \varepsilon_0 \frac{\partial^2 \mathrm{E}}{\partial \mathrm{t}^2},$$

Equation 6

which is the electromagnetic wave equation. Before continuing, two assumptions about MT must be specified. The first is that the EM signals used in MT are at such low frequencies that the fields change at rates slow enough that they can be considered static fields. This quasi-static assumption along with the very small values of the constants μ_0 and ε_0, makes the second derivative term in Equation 6 negligible. The second assumption is that the Earth is sufficiently conductive that the first term on the right-hand side of Equation 6 is much larger than the second term. While there is wide variability in conductivity of individual crystals and fluids in the Earth between about 10^{10} and 10^{-10} S/m, the most resistive rocks on a scale large enough to be measured by MT have bulk conductivities above 10^{-5} S/m, with typical rocks ranging from 10^{0} to 10^{-4} S/m (Pommier & Le-Trong, 2011; Tyburczy & Fisler, 1995; Yoshino, 2010). Therefore, the

second term becomes negligible relative to the first. Discarding it results in the diffusion equation for electric fields:

$$\nabla^2 \mathrm{E} - \mu\, \sigma \frac{\partial \mathrm{E}}{\partial \mathrm{t}} = 0.$$

Equation 7

A similar procedure can be followed to give the equivalent equation for magnetic fields. Thus, in the quasi-static approximation, in both time- and frequency-domains, it is common practice to approximate the MT governing equations as diffusion rather than wave equations. It should be noted, however, that a transformation exists into the fictitious wave domain (Mittet, 2015) in which the low frequency electromagnetic induction problem can be expressed to a close approximation as a wave propagation rather than diffusion phenomenon.

Variable	**Description**	**Units**
E	Electric field	V/m
H	Magnetic field	A/m
B	Magnetic flux density	Tesla
t	Time	s
T	Period	s
ω	Angular frequency	s^{-1}
μ_0	Magnetic permeability of free space	$4\pi \times 10^{-7}$ V s A^{-1} m^{-1}
ε	Electrical permittivity	8.85×10^{-12} F/m
β	Charge density	C/m^3
J	Current density	A/m^2
σ	Conductivity	S/m
ρ	Resistivity	Ωm
S	Electrical conductance	1/Ω

Table 1.Units used in electromagnetism.

2.3.2 2D and 3D MT

Induced electric currents flow primarily horizontally, and their behavior upon encountering a material of contrasting resistivity is the subject of two-dimensional (2D)

and three-dimensional (3D) MT. The charge-free assumption is not valid when current can travel across boundaries between materials of contrasting conductivity. In 2D MT, where MT measurements are taken along a line of stations traversing a target of interest, it is common to separate the orthogonal E and H signals into two sets of data. The first set involves current that travels across conductivity boundaries (across geoelectric strike) with magnetic fields that are measured parallel to strike, called the "transverse magnetic" or TM mode. The second set of signals is the "transverse electric" or TE mode, whose magnetic field measurements are taken across strike and electric fields are measured parallel to strike. Because the TM mode involves current that crosses a conductivity boundary, and current is continuous, the Ohm's Law relationship $\sigma E = J$ (where J is current density) requires charge to exist along conductivity boundaries because E must be discontinuous if σ is discontinuous. Because TM mode accounts for boundary charges, complex structures are usually resolved better using the TM mode (P. Wannamaker et al., 1984). However, the TM mode can also be very strongly affected by small-scale near-surface features that alter the observed conductivity at all frequencies (see section 2.4.5 for more on distortion), which do not affect the TE mode as strongly. Additionally, the TE mode may be more useful in resolving structures that are resistive rather than conductive (Berdichevsky et al., 1998). It is common to solve both modes simultaneously to obtain a robust 2D solution.

The presence of surface charge in 2D and 3D MT requires that Equation 4 (containing the analytically cumbersome $\nabla\times\nabla\times E$ term) is solved. This is usually done with the integral form of Maxwell's equations and/or in the frequency domain for mathematical simplicity. A common way of solving these problems is with a finite difference approach. E and H can be approximated in two or three dimensions by subdividing the Earth's interior into a grid of rectangular blocks (rectangles or prisms for 2D and 3D, respectively) and integrating E and H along simple rectangular loops through the block faces (or edges). While this is not as accurate as solving Maxwell's equations at every point, this simple geometry eases the computational burden sufficiently that a large enough number of blocks can be used to obtain a satisfactorily accurate solution within

a reasonable time (e.g. Egbert & Kelbert, 2012; Mackie et al., 1994; Siripunvaraporn et al., 2005; Smith, 1996; Yee, 1966). Additional information about dimensionality in MT will be given in section 2.4.4.

2.4 MT fundamental principles

2.4.1 Signal source

The source of MT data is ideally modeled as a time-varying magnetic field produced at a sufficiently great distance above the Earth's surface (e.g. at ionospheric heights of 90 km or greater) that it is assumed to be a plane wave when it reaches the surface, inducing an electric field in the same horizontal plane as the incoming magnetic field. Conventional wisdom holds that this assumption is valid at mid-geomagnetic latitudes distant from the auroral current systems and equatorial electrojet. However, studies in Antarctica have shown that high-quality data is obtainable despite close proximity to geomagnetic poles for periods between 0.01 s and 4000 s (Beblo & Liebig, 1990; Peacock & Selway, 2016; P. E. Wannamaker et al., 1996, 2004). Nonplanar source effects at polar latitudes are present only intermittently and can be identified and removed through time-frequency analysis (Chant & Hastie, 1992; Peacock & Selway, 2016).

2.4.2 Skin Depth

Because MT is most typically implemented as a frequency domain method, E and H are considered periodic signals with an $e^{i\omega t}$ time dependence. Whereas previous sections of this paper used time domain expressions, this section will use the frequency domain. Equation 7 is then restated as:

$$\nabla^2 \mathrm{E} - i\omega\,\mu\,\sigma \mathrm{E} = 0.$$

Equation 8

To consider how this frequency-domain expression maps into the spatial domain as the electric and magnetic fields penetrate into the Earth, we must consider it in the

wavenumber domain as well as the frequency domain. The iωμσ term in Equation 8 is the square of the complex wavenumber $k^2 = i\omega\mu\sigma$, or $k = \sqrt{i\omega\mu\sigma}$, which is a value that describes EM field attenuation in a conductor and has units of m^{-1}, where ω is the radian frequency ($\omega = 2\pi f$), μ is the magnetic permeability of the geologic material (usually taken to have the free space value $\mu_0 = 1.257 \times 10^{-6}$ H/m), and σ is the electrical conductivity (S/m), with its reciprocal being the electrical resistivity $\rho = \sigma^{-1}$ (Ωm), and i is $\sqrt{-1}$. It should also be noted that some geophysics texts use the convention that $k^2 = -i\omega\mu\sigma$ (Ward & Hohmann, 1988). The frequency-to-spatial mapping described here uses the reduced, or quasi-static form of the wavenumber. The full form needed for higher frequencies beyond those typically used in MT (generally above the audio band f > 20 kHz) is $k^2 = i\omega\mu\sigma - \mu\omega^2\varepsilon$.

The reciprocal of the real part of this expression gives the skin depth δ(ω,σ), the depth to which an inducing magnetic field of a given frequency ω at the surface of a conducting body decays in amplitude to 1/e of its surface amplitude. The real part of the expression for k is as follows:

$$\mathrm{k} = \sqrt{i\,\omega\,\mu\,\sigma} = \sqrt{i}\sqrt{\omega\,\mu\,\sigma} = \frac{1+i}{\sqrt{2}}\sqrt{\omega\,\mu\,\sigma} = \sqrt{\omega\,\mu\,\sigma\,/2} + i\sqrt{\omega\,\mu\,\sigma\,/2}.$$

Equation 9

With the reciprocal of the real part of Equation 9 being $\sqrt{2/\omega\,\mu\,\sigma}$. Rather than using units of conductivity, its reciprocal—resistivity—is preferred in modern studies. Furthermore, the EM signals produced by GICs vary over such long time scales that it is appropriate to work with period rather than frequency. Restating the previous expression in terms of resistivity and period gives:

$$\delta = \sqrt{2/(8\,\pi^{\,2} \times 10^{-7})}\sqrt{\rho\,\mathrm{T}} \approx 503.29\sqrt{\rho\,\mathrm{T}}.$$

Equation 10

The skin depth is often used as a rough estimate of the depth of sensitivity for data at a given period for an assumed half-space resistivity.

2.4.3 Impedance tensor

The magnetotelluric impedance tensor is a complex 2×2 matrix that represents the relationship between the electric and magnetic fields at a specified frequency. This relationship depends on the resistivity of the subsurface, and the ratio E/H at a given frequency defines resistivity in a half-space. More complex subsurface resistivity structures will be discussed in the next section. Generally, a rank-2 tensor relates two vectors in every combination of the basis vectors in which they exist. However, the assumptions used in MT eliminate terms in the impedance tensor involving the vertical direction, leaving only the x and y basis vectors, which represent the north and east directions, respectively. The complete 3×3 impedance tensor using x, y, and z directions is shown in Figure 1a. Because electric fields measured at the surface have no vertical component, the bottom row is eliminated. And because the MT method uses only the electric fields polarized in the x and y directions and a vertical magnetic field would create circulating electric fields, the right column is eliminated. This results in the simplified 2×2 impedance tensor that is used in MT, shown in Figure 1b.

Even though the vertical magnetic field is not used in MT for GIC estimation, it is worth mentioning that it is helpful in resistivity modeling to use the vertical magnetic transfer function (VTF), also called the tipper, which relates the vertical and horizontal magnetic fields according to the relationship $B_z = T_{zx}B_x + T_{zy}B_y$. VTFs are complementary to MT data by helping to indicate dimensionality, highlight lateral resistivity boundaries, and for creating frequency-dependent induction vectors that point toward (or away from,

depending on the direction convention used) conductive bodies (e.g. Parkinson, 1962; Gregori & Lanzerotti, 1980; Weaver & Agarwal, 1991).

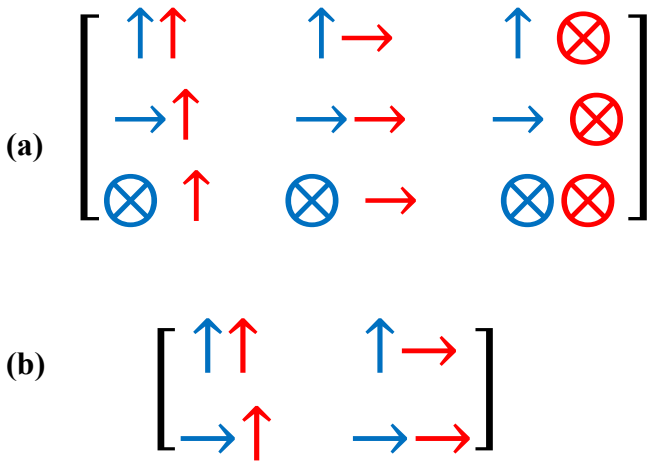

Figure 1. (a) Vector combinations used in the impedance tensor when vertical fields are considered. Blue arrows represent electric field directions, red arrows represent magnetic field directions. Conventionally, x is positive north, y is positive east, and z is positive down. (b) Eliminating tensor components that are not used in MT gives the simplified 2×2 impedance tensor, which has only horizontal electric and magnetic fields.

In the following discussion, variables that represent matrices are identified by bold font. The impedance tensor, **Z**, is used as a transfer function that relates the electric and magnetic fields according to Equation 11 below, where **Z** is simply **E**/**H**. Since **Z** and **H** are multiplied in the frequency domain, **Z** can be thought of as the transfer function that describes a filter producing the output **E** from the input **H**. Equation 12 gives the impedance tensor and its relation to the E and H fields when the independent x and y polarizations are both used. As illustrated in Figure 1, the off-diagonal Z_{xy} and Z_{yx} components come from orthogonal E and H fields. When E and H fields have a parallel component, the diagonal Z_{xx} and Z_{yy} impedance tensor elements are nonzero. This holds where the geoelectrical structure is three-dimensional, which is generally the case to varying extent in real data. Dimensionality will be discussed in more detail in the next section.

$$\mathbf{E} = \mathbf{ZH}.$$

Equation 11

$$\begin{bmatrix} \mathrm{E_x} \\ \mathrm{E_y} \end{bmatrix} = \begin{bmatrix} \mathrm{Z_{xx}} & \mathrm{Z_{xy}} \\ \mathrm{Z_{yx}} & \mathrm{Z_{yy}} \end{bmatrix} \begin{bmatrix} \mathrm{H_x} \\ \mathrm{H_y} \end{bmatrix}.$$

Equation 12

Impedance is closely related to apparent resistivity ρ_a, which is the resistivity of a uniform half-space for data at a given frequency. Impedance can be converted to apparent resistivity through the equation:

$$\rho_{\,\mathrm{a}} = \frac{1}{\omega\,\mu}\,|\mathbf{Z}|^2,$$

Equation 13

where each component of **Z** is calculated independently. The phase of the impedance tensor is also calculated from **Z**, referring to the phase delay of the magnetic field relative to the electric field. Phase is calculated as follows:

$$\Phi = \tan^{-1}\frac{imag(\mathbf{Z})}{real(\mathbf{Z})}.$$

Equation 14

The phase above a half-space of uniform resistivity is 45° at all frequencies. This comes from $\sqrt{i}$ term in Equation 9, which has a phase angle of 45°. Phase angle remains at 45° for all frequencies in a half-space, and in settings with geologic structure it increases when the signal penetrates into a more conductive material and decreases when a more resistive material is reached.

2.4.4 Dimensionality

An important part of any MT study is analyzing the dimensionality of the subsurface electrical structure. One-dimensional (1D), two-dimensional (2D), and three-dimensional

(3D) structures have characteristic properties in the impedance tensor and allow for different assumptions to be made that can greatly simplify modeling and analysis. However, it is never appropriate to use lower dimensionality analysis methods on data that shows strong higher dimensionality characteristics, such as 1D methods on data with a 2D geoelectrical structure. While the savings in processing time may be tempting, one must be aware that the resulting interpretation is inevitably inaccurate and possibly misleading.

Other than a uniform half-space, the simplest resistivity model is that of a 1D earth. In this model, only horizontal layers of infinite lateral extent exist. The ratio E/H is the same in every direction and the resulting impedance tensor has equal amplitudes for the two components whose E and H fields are orthogonal (Z_{xy} and Z_{yx}), and their phases are 180 degrees apart, resulting in:

$$\mathbf{Z} = \begin{bmatrix} 0 & Z_{1D} \\ -Z_{1D} & 0 \end{bmatrix}.$$

Equation 15

For a 1D Earth, the horizontal electric and magnetic fields are always orthogonal to each other, so any rotation in the polarization of the inducing magnetic fields leads to an identical relative rotation in the polarization of the induced electric field. Furthermore, the intensity of the induced electric field does not change under such a rotation of the magnetic field, if the intensity of the magnetic field does not change. This simple relationship between inducing magnetic and induced electric field is unique to the 1D induction problem, and does not hold for higher dimensional cases.

It is useful to mention that present day power utility industry practice is to apply regional-scale 1D conductivity models to the problem of estimating the predicted intensity of GICs due to geomagnetic disturbances. The impact of the forced orthogonality between electric and magnetic fields, as well as the azimuthally independent response of such a 1D structure to inducing magnetic fields of different polarizations on estimates of GICs

in a real world where 3D resistivity structures are ubiquitous is an area of considerable research.

A 2D geoelectrical structure arises when the resistivity varies with depth and horizontally in one direction, with structures extending infinitely in the other horizontal direction. A geologic analog is a fault, where rock properties change going across the fault but do not change parallel to the fault over distances that MT data are sensitive to. In this setting, the E and H fields orthogonal to the fault are independent of those measured parallel to the fault, and $Z_{xy} \neq Z_{yx}$. With resistivity structure varying in only one horizontal dimension, there is still no way for a magnetic field to induce a parallel electric field, so the diagonal elements of Z remain zero and the impedance tensor reduces to:

$$\mathbf{Z} = \begin{bmatrix} 0 & \mathrm{Z_{xy}} \\ \mathrm{Z_{yx}} & 0 \end{bmatrix}.$$

Equation 16

A 3D geoelectrical structure is one where resistivity can vary with depth and with position in both x and y directions. All geologic settings exhibit this behavior to some extent, but it is often ignored if the 3D effect is small enough to justify 2D or even 1D analysis. 3D MT data exhibits magnetic fields that can induce electric fields in any direction, including parallel to the inducing magnetic field. This can happen when, for example, a magnetic field induces current in a conductor running diagonally to the magnetic field vector. This can occur when the conductor is arcuate or amorphous, or if the data are not rotated to align the x polarization with geoelectric strike. The full impedance tensor is required to describe these situations:

$$\mathbf{Z} = \begin{bmatrix} \mathrm{Z_{xx}} & \mathrm{Z_{xy}} \\ \mathrm{Z_{yx}} & \mathrm{Z_{yy}} \end{bmatrix}.$$

Equation 17

It is important to note that for the general 3D induction case, even a small rotation of the inducing magnetic field can lead to large rotations in the induced electric field as well as large changes in the electric field intensity, even if the intensity of the inducing magnetic field is constant during the change in its polarization. This has profound consequences when calculating the GICs induced in electric transmission lines by GMDs since the coupling of induced ground electric fields into transmission lines depends on the instantaneous polarization of the ground electric field and the degree to which it is aligned with the direction of each transmission line segment. Ground electric fields resulting from 3D conductivity structures may have entirely different field polarizations at a given moment during a GMD than those from a 1D structure. Whereas the peak GIC for a 1D scenario always occurs during the peak of a GMD, this is not the case in 3D, since the instantaneous polarization of the electric field, as well as its intensity, determines the intensity of the GIC (e.g. Bonner & Schultz, 2017).

2.4.5 Distortion

The assumption that charge density is uniform is only true in a half-space and in 1D models. Higher dimensional models allow current to cross an interface between materials of contrasting resistivity. Because current density is the product of conductivity and electric field, conservation of current requires an electric field discontinuity at the interface. This is accommodated by accumulation of charge on the interface to counter the electric field on the conductive side and strengthen it on the resistive side of the interface. 2D and 3D MT implements the complete $\nabla \times \nabla \times E$ solution without the charge-free simplifications described in section 2.3.1. However, local heterogeneities in the conductivity structure can be too small to be accurately measured or modeled. Accumulated charge along local resistivity boundaries with lateral dimensions much smaller than a skin depth deflects currents in ways that the data cannot account for, known as galvanic distortion. This non-inductive component to the data distort it in several ways, though some of the effect is recoverable (Bahr, 1988; Jiracek, 1990). One of these effects is amplification of the electric fields in one direction, changing the impedance in the affected direction so that the apparent resistivity curve is shifted to

appear higher or lower by a constant amount for every frequency, an effect known as static shift. Another effect is an apparent rotation or twist to the data when shallow current flow is diverted to follow a curved path near the measurement location. The effect of distortion is evaluated in terms of a 2×2 distortion tensor **D** that operates on the true impedance along with a rotation matrix **R** to create the measured impedance as follows (Groom & Bailey, 1989):

$$\mathbf{Z_{distorted}} = \mathbf{RDZ_{true}R}^{\mathrm{T}}.$$

Equation 18

Determining the contents of **D** and **R** was the great challenge of the 1D and 2D eras of MT, while the application of distortion removal methods in 3D MT is an area of considerable discussion, with some practitioners explicitly removing distortion terms prior to inversion (see Section 2.6.2 for inversion information) of the impedance tensor (Ledo et al., 1998; Utada & Munekane, 2000; Sasaki, 2004; Zhdanov et al., 2011) and others adding shallow scattering layers into their 3D model to accommodate the effects of unresolvably small electric field distorting structures (e.g. Meqbel et al., 2014).

It is not possible to fully determine **D** and **R**, but distortion can be decomposed into components that isolate the determinable parts from the indeterminable parts (Groom & Bailey, 1989). This allows as much of the unknown near-surface behavior to be removed as possible, helping to remove small-scale apparent 3D effects from data that is otherwise 2D. The distortion tensor **D** is real, so it leaves the phase of **Z** unaffected (Bahr, 1988). Therefore, MT analysis methods that seek to fit the impedance phase as a discrete step in the modeling process, such as phase tensor analysis (Caldwell et al., 2004; Booker, 2014) and phase tensor inversion (Patro et al., 2013; Tietze et al., 2015), are also helpful in solving distortion problems. In practice, 3D inverse modeling is able to account for distortion if shallow parts of the model are finely discretized and allowed to change as necessary to satisfy the distortion, while the user must be aware that the shallow features thereby created do not represent true geologic structures.

Caution must be used when using impedance tensors for GIC prediction if their distortion components were removed for inverse modeling. If the distortion components have been stripped from the impedance tensor, then the tensor no longer fully represents the electrical properties of the site where it was measured and predictions will produce undistorted electric fields that do not match the observed, distorted electric fields (Bonner & Schultz, 2017). This could be a problem if electric fields are predicted using methods that use a modeled impedance tensor rather than an observed impedance tensor in areas where the subsurface materials have strong anisotropy.

2.5 Data acquisition

2.5.1 Array Design

The process of acquiring MT data begins with designing an MT station array of appropriate aperture, inter-station spacing and frequency bandwidth suitable to discriminating the location and properties of geoelectric target features in the crust and, when appropriate, the mantle below. The frequency bandwidth is determined by the desired range of depths of penetration beneath ground level required to delineate the survey targets. This determines the period of time a given MT station must operate before removal and relocation to another location on the survey grid, since lower frequency data will require a longer duration of data acquisition than higher frequency data. In order to obtain MT impedance tensor data of sufficient quality (for instance, nominally 5% confidence limits in apparent resistivity and less than 3 degrees uncertainty in phase) over a frequency band of 10^{-4} Hz – 10^{-1} Hz, as is characteristic of data from the EarthScope MT Transportable Array (Schultz et al., 2006-2018), typically requires anywhere from 5 days to 28 days of continuous recording at each site, depending on the level of GMD activity during the recording period and the level of local electromagnetic noise sources. This further determines the selection of MT data acquisition hardware to use, since different sensor and data acquisition technologies are optimized for different frequency ranges. Thus, this first stage of array design is foundational to the data acquisition process.

The goal of most MT investigations is to address hypotheses that have been posed in relation to potential targets, such as the economic viability of specific geothermal energy (e.g. Fitterman, 1988; Newman et al., 2008; Peacock et al., 2012; P. E. Wannamaker et al., 2004), groundwater (e.g. Bernard et al., 1990; Nichols et al., 1994), mineral or hydrocarbon resources (e.g. Stevens & McNeice, 1998; Tuncer et al., 2006); or the relationship of deep-seated crustal and upper mantle hydrous and magmatic fluids to regional seismicity or surface volcanic features (e.g. Bedrosian et al., 2018; McGary et al., 2014; Meqbel et al., 2014; Peacock et al., 2016). To-date, there has been an paucity of MT data acquisition efforts specifically designed to address the concerns of the electric utilities in determining ground electric fields associated with GMDs. The use of MT data for this application has been *a posteriori* and opportunistic, and involves data from MT array designs optimized to address geologic targets that might be somewhat different than array configurations optimized for power grid resilience purposes.

Increasingly MT surveys are components of integrated, multidisciplinary data acquisition efforts, where MT data are combined with seismic, potential fields, and other observations in order to better constrain the geological process of interest (e.g. Pritchard et al., 2018). Up until the mid-2000s such investigations had been limited to 2D interpretations and survey designs that restricted data acquisition to a small number of transects along lines believed to be parallel or orthogonal to regional geologic and geoelectric strike directions. There are many cases at present where 2D survey designs persist, in large measure because of the greater cost of acquiring 3D data on a grid relative to acquiring 2D data on specific profiles along a line as well as the high computational demands of 3D inverse modeling compared to 2D.

Such 2D survey arrays have increasingly given way over the past fifteen years to 3D surveys, where MT stations are deployed in quasi-regular latitude, longitude grids. The transition from 2D to 3D surveys has been made possible in part by the availability of 3D MT inverse modeling codes designed to produce images of resistivity structure from arrays of impedance tensors (Egbert & Kelbert, 2012; Kelbert et al., 2014; Siripunvaraporn et al., 2005). The development of large MT facilities capable of

deploying many tens of MT instruments simultaneously has made possible the collection of the large array data sets required for 3D interpretation. The long-running National Science Foundation (NSF) EarthScope Magnetotelluric Program (Schultz et al., 2006-2018) and the subsequent SinoProbe (Dong et al., 2013) and AusLAMP (Robertson et al., 2016; S. Thiel et al., 2016) MT Programs were the first to carry out continental-scale 3D MT reconnaissance mapping with large arrays, further promoting the adoption of 3D MT survey designs. In contrast to previous, more targeted 2D surveys, these large array efforts can provide broad-scale identification of targets of follow-on interest in otherwise unexplored areas.

The ability to resolve structural details in electrical resistivity is determined by the aperture of the MT array both inline and broadside to potential subsurface targets, the spacing between MT stations, and the frequency bandwidth of the recorded MT data. In practical terms, the main limitations in optimal array design are economic, with the cost of operations being the key factor.

While it is possible to install permanent or quasi-permanent MT instrumentation to enable continuous monitoring of the electric and magnetic fields over periods of months and years, this is rarely done. There have been a limited number of such installations at a handful of widely-spaced magnetic observatories (coordinated through the International Association of Geomagnetism and Aeronomy's INTERMAGNET program), and also within the NSF EarthScope program, seven "Backbone" MT stations of this type were operated for a number of years, following earlier ultra-long period MT work in deep lakebottoms (Schultz et al., 1987, 1993). The many advantages of using long-term, continuous monitoring of the ground electric and magnetic fields include the following: to study the spatial variability of Earth-ionospheric coupling; to obtain constraints on deep mantle electrical resistivity structure; to study temporal changes in resistivity structure associated with transient events; and to obtain a set of baseline observations for monitoring ground electric fields for GIC studies. However, the challenge of maintaining stable long-period electric field measurements—as well as the cost of maintaining such stations—inhibits their general use. Rather than permanent

installation of MT equipment, the general deployment mode is for the temporary installation of a relocatable array of MT instruments.

Broad-scale 3D reconnaissance mapping surveys are typically done using temporary installations of long-period MT instruments to create baseline 3D models and potentially to identify targets for subsequent higher-resolution studies. In order to cover a large territory efficiently, survey designs trade-off potential spatial resolving power against the cost and efficiency of operations by using as large an inter-station spacing as possible, up to the point where aliasing of potential resistivity target signatures becomes a dominating factor. For example, the EarthScope MT Transportable Array station spacing of 70 km has proven adequate for delineation of major structural features in the mid-crust to upper mantle, while shallower structures tend to have a speckled appearance, reflecting the station distribution more than the underlying geology (Bedrosian, 2016). With somewhat greater interest in shallower mineral resource questions, the AusLAMP array employs ~55 km (1/2 degree) station spacing. Serendipitously, broad-scale MT data sets have proven extremely important to those researching space weather effects on the power grid (e.g. Bonner & Schultz, 2017; Love et al., 2016, 2018; Lucas et al., 2018).

Also common are wideband MT arrays, potentially with even finer inter-station spacing (<1 km – 20 km). These surveys can be designed to discriminate features in the upper crust, including the near-surface and even in the critical zone. While no studies exist to show if densely-spaced wideband MT survey data provide meaningful improvements to the accuracy of GIC estimates, physical scaling relations suggest that this MT survey data would provide improved GIC estimates for artificially induced GICs caused by exo-atmospheric detonation of nuclear devices, i.e. electromagnetic pulse or “EMP” weapons, since the signature of the artificially induced GMDs from these events includes intense signals at higher frequencies than for natural GMDs, thus also generating electromagnetic induction effects at finer scales within upper crustal resistivity structures.

2.5.2 MT sensors and data acquisition systems

The MT signal band can be divided into the long-period band associated with space weather modulations of ionospheric and magnetospheric electric fields (typically below ~1-10 Hz) and wideband variations associated with ionospheric waveguide propagation of signals due to global lightning activity (above 10 Hz). The natural background power spectral density for geomagnetic field variations follows a 1/*f* law at long periods, but in the transition between these two bands, known as the “long-period MT dead band”, the signal level drops off sharply, but rises again at about 1 Hz and above (Vozoff, 1991). Available technologies for measuring vector magnetic fields also follow similar low and high frequency bandwidth divisions, and while a variety of different magnetic field sensor technologies have been employed in the past, contemporary surveys generally use one or both of induction coil and/or fluxgate magnetometer technologies to cover one or both bands.

Induction coil magnetometers (Pronenko & Korepanov, 2009; Tumanski, 2007) employ fine solenoidal windings surrounding highly magnetically permeable core material in a linear configuration, so that each induction coil is sensitive to time-variations ($\partial B/\partial t$) of the magnetic field in the direction of the axis of the solenoid. In order to measure the full vector magnetic field variation, three coils are employed and typically deployed with each pointing in one of the three cardinal directions of the compass. Since induction coils are directly sensitive to time rate of changes in the magnetic field rather than to the field directly, their sensitivity drops off at lower frequencies, although this is compensated for by conditioning circuitry that amplifies and integrates the signal. The induction coils can be tuned for sensitivity over a given frequency bandwidth by modifying various design parameters, such as the length, configuration and mass of the permeable core material and surrounding windings, and the number, gauge and resistance of the windings (the latter factor impacting the Johnson or thermal noise limit of the sensors). All other things being equal, longer induction coils tend to have improved long-period sensitivity than shorter coils, whereas the reverse is also true; shorter coils tend to have improved high-frequency sensitivity than longer coils.

Induction coils are suitable for crustal MT surveys that are used for power grid GIC applications, but in order to cover the 10^{-4} Hz – 10^{-1} Hz frequency bandwidth needed for such studies, wideband coils must be employed. The current state-of-the-art for such wideband coils are designs that can exceed 1 meter in length for each coil. The major disadvantages of induction coils are their bulk and weight, their cost, and to a lesser extent, their power consumption.

The fluxgate (Primdahl, 1979; Ripka, 1992, 2003) is the other predominant magnetic field sensor technology used in contemporary MT, which generally comes in two configurations: linear core and ring core. Fluxgates are directly sensitive to the magnetic field rather than its time-derivative. A highly permeable magnetic core is surrounded by a winding (either solenoidal for linear cores, or helical for ring cores). An alternating current is imposed in the winding that generates a magnetic field that drives the core into and out of magnetic saturation. The Earth's magnetic field influences the time during each AC cycle at which the core is saturated, leading to a detectible hysteresis that is picked up by a secondary winding surrounding the core. The phase (time lead or lag relative to zero external magnetic field saturation) of the signal scales with the intensity of the external magnetic field. In order to boost sensitivity, some of the highest quality fluxgate sensors are approximately nulling sensors, where most of the main part of the external magnetic field is bucked out by an artificially imposed magnetic field generated by Helmholtz coils that surround the fluxgate, and the residual hysteresis signal is then digitized.

A vector fluxgate sensor consists of three sets of cores and windings, with each set oriented to be sensitive to one vector component of the magnetic field. Fluxgate sensors can be extremely low power, with <10 mW power consumption for a precision three-component vector fluxgate instrument representing the current state of the art. Fluxgates are also compact, with a three-component sensor fitting within a cube of less than 7 cm on a side. These attributes, as well as relatively low cost (roughly half to one-third the cost of a wideband set of three induction coils) make fluxgates a popular choice for long-period MT surveys, although a complicating factor in recent years has

been the difficulty in securing high-quality permeable core material suitable for construction of the highest quality fluxgate sensors. Whereas induction coils can be configured for sensitivity to the natural MT signal at frequencies extending into the kHz band, the current state-of-the-art for precision fluxgates limits them to sampling frequencies below ~10 Hz or lower.

The MT method requires measurement of the horizontal vector components of the electric field at the ground surface. Most typically, pairs of carefully matched non-polarizing electrodes (Petiau, 2000) are grounded to the soil to make low impedance galvanic/electrolytic contact, separated by a certain distance (100 m being a commonly used separation). With a sufficiently large amplifier input impedance, the flow of electric currents between the electrode pairs can be inhibited, therefore maintaining their stability by preventing the electrodes from becoming polarized by electrolytic deposition of metal salt compounds from one electrode serving as an anode to the other's cathode. Two electrode pairs are usually used, with one pair orthogonal to the other, or otherwise with a large angle separating the pairs so the data from them may subsequently rotated and projected to orthogonal coordinates. Continuous recordings are made of the voltages between the matched electrode pairs, which—divided by the electrode separation distance—provides a very close approximation to the electric field at the mid-point of the cable connecting the electrodes.

The signal-to-noise level of the electric field measurements is directly impacted by the distance between electrode pairs, with larger separations producing larger signal levels of the electric field (units: V m^{-1}). Obtaining stable electric field measurements is progressively more challenging at lower frequencies, since a variety of environmental factors can produce spurious potentials at the electrodes, including thermal drift effects, streaming potentials and changes in the electropotential of topsoil related to flowing surface water, etc. These effects manifest as time-variable self-potentials (SP) that are superimposed on the induced electric fields of interest. SP effects can be mitigated to an extent by careful attention to detail, such as preparing shallow holes for electrode installation with mud made from native soils, introducing an intermediate medium such

as water-saturated (hydrophilic) bentonite or kaolinite clay, which can optionally be mixed with a salt solution and then buried and thermally insulated. In areas that are extremely arid or frozen, it can be difficult to achieve good, low-impedance electrolytic coupling with ground, and alternative approaches can be taken, such as the use of high impedance buffer amplifiers (Wannamaker et al., 1996), or capacitively coupled electrodes (Hibbs et al., 2012), but generally at a cost of poor performance at frequencies below about 1 Hz. Given this consideration, for surveys appropriate for GIC studies, which require good low frequency coupling, conventional galvanically coupled electrodes are preferred.

Variations in the MT installation design include use of non-orthogonal electric dipole sensors, or magnetic field sensors installed in coordinates rotated from the cardinal directions, or electrodes and magnetic field sensors placed on the surface of the ground rather than buried, with special measures taken to achieve stable measurements and to rotate the resulting MT data into cardinal directions. Such sub-aerial installations can simplify permitting requirements for sites where ground disturbances are to be avoided. Two versions of a typical MT station installation are shown in Figure 2. Both versions have the same electric dipole lengths, but with the center points in different locations to accommodate different field conditions where one configuration might be preferred for convenience or accessibility in difficult terrain. Some instruments may be designed in a way that favors the use of a centrally-located receiver, while others allow for flexibility in the receiver’s location. Both are shown in Figure 2.

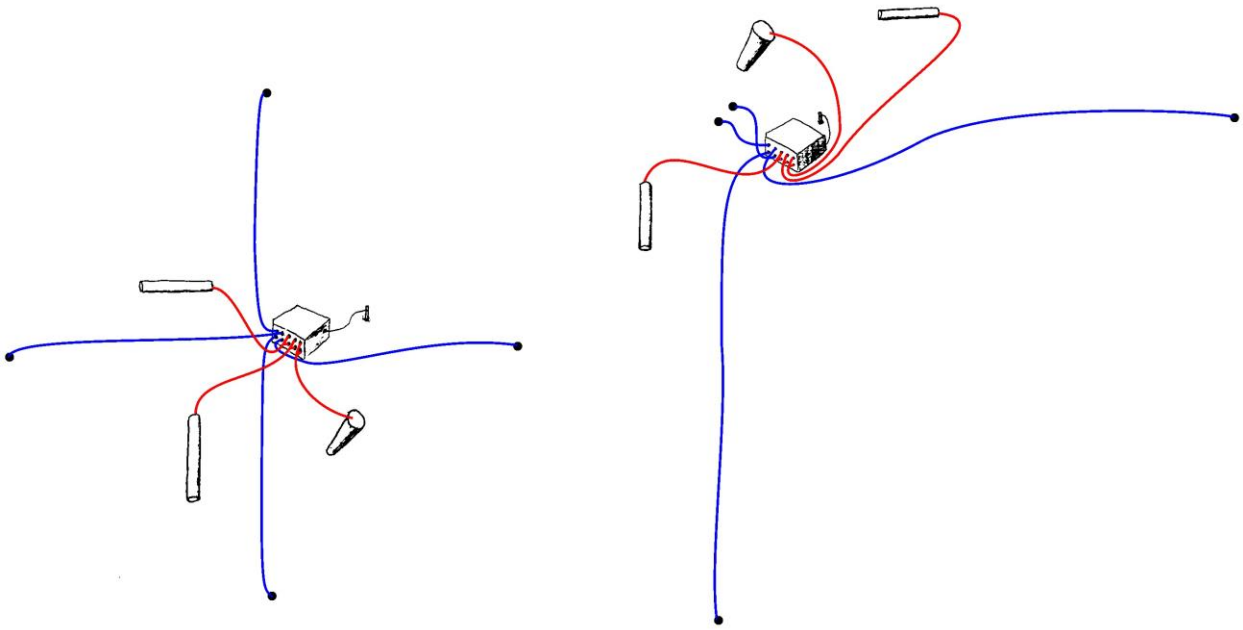

Figure 2. Schematic of typical MT station installation geometry. (left) Two sets of matched electrode pairs are aligned in cardinal coordinates (north-south and east-west) each forming an electric dipole sensor ~100 m in length. A fifth electrode is shown, which is a grounding rod for the recording system ground plane. Three magnetic field sensors (induction coils, as shown, or a unitary tri-axial fluxgate sensor (not shown) are buried in shallow trenches or holes. The magnetic field sensors are aligned to cardinal coordinates typically with an accuracy of $\pm$ 1º, and the electrodes are positioned with an accuracy of 0.5 m over a distance of 100 m. (right) as in figure at left, but rather than a cross-shaped electric dipole array, an “L” shaped array is used instead.

2.6 Data processing and inversion

Converting time-series EM field data to impedance is not as simple as dividing E by H in the frequency domain. Resulting from complex natural phenomena, MT source signal strength is highly variable and out of the user’s control, and noise is always present. Noise can be natural, such as swaying trees or groundwater flow, or manmade, such as electrical infrastructure, and its effects can be either highly localized or contaminate data over 100 km away from the noise source (Egbert & Livelybrooks, 1996; Egbert et al., 2000; Kappler et al., 2010). To minimize noise contamination, uncorrelated noise is rejected and an ensemble averaging approach is used to estimate impedance tensors

and their variances. An example of MT time-series data recorded during a two-day period of moderately strong geomagnetic activity is given in Figure 3.

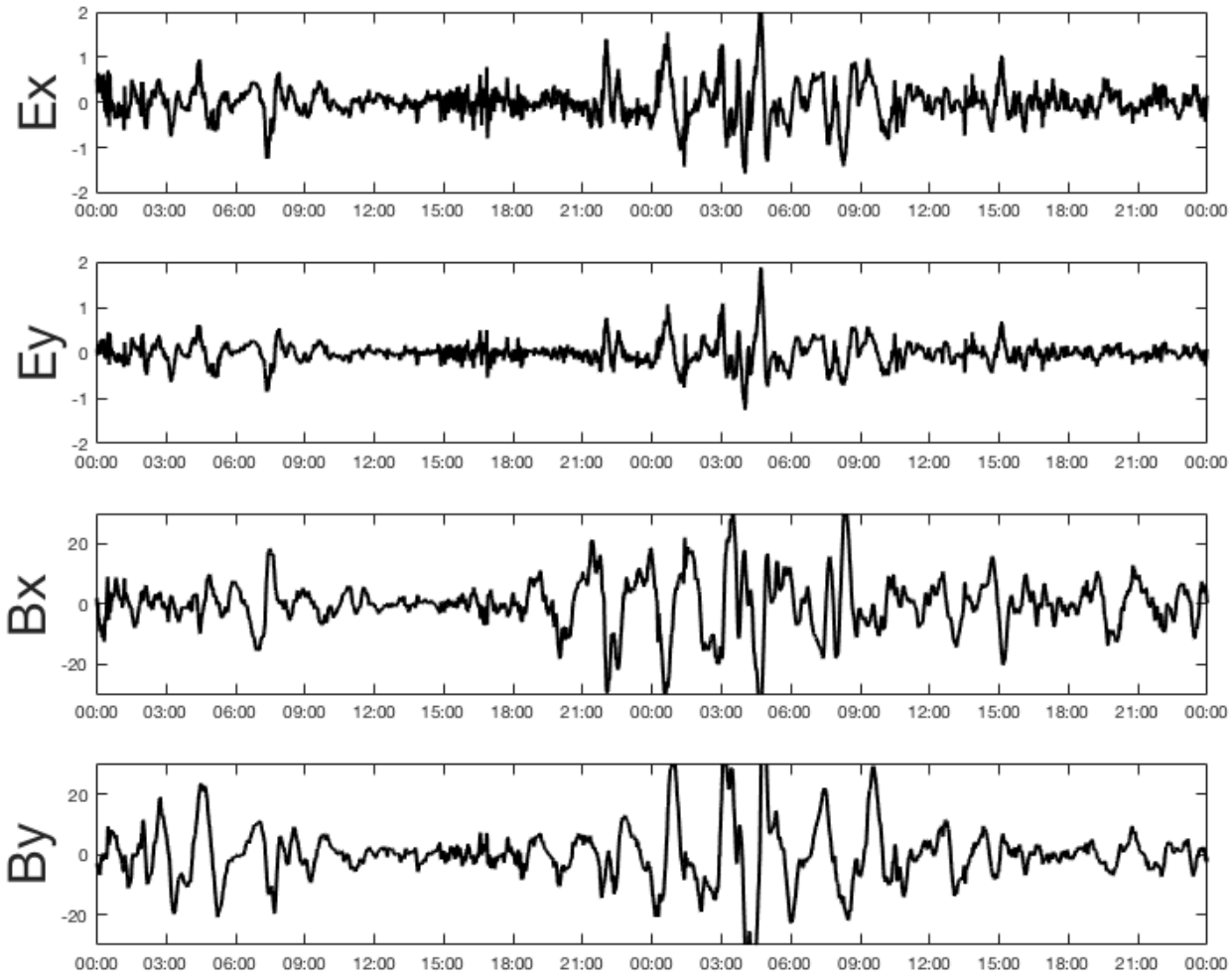

Figure 3. A two-day recording of raw, uncalibrated MT time series data from a site in southwestern Idaho, USA, during a time of strong geomagnetic activity. Data were recorded in a coordinate system where positive x is north and positive y is east.

2.6.1 Processing Methods

Impedances are estimated through the following steps, although there are several variations in approaches taken by different practitioners:

1. Divide the EM time-series data into short segments of equal length, detrend each segment and apply other prewhitening methods, then use a windowing function to

taper the start and end of each segment in order to reduce spectral leakage. Although the entire time-series can have many millions of samples, each segment usually has only hundreds-to-tens of thousands of samples.

2. Fourier transform each segment, producing an ensemble of Fourier coefficients for the range of frequencies covered by the segment length. Data calibration is usually done in this step to correct for sensor and amplifier responses.

3. For each segment, calculate the impedance tensor and variance by solving Equation 19 for the four components of **Z**. With ideal, noise-free data, the solution is given by:

$$\mathbf{Z} = \langle \mathbf{E}\mathbf{H}^{*} \rangle \langle \mathbf{H}\mathbf{H}^{*} \rangle^{-\mathbf{1}}$$

Equation 19

Where $\langle \boldsymbol{EH}^{*} \rangle$ is an outer product resulting in a 2x2 matrix of cross powers. Likewise, $\langle \boldsymbol{HH}^{*} \rangle$ gives auto powers. The brackets denote averages over the time windows. Therefore, the impedance comes from the coherence of **E** and **H**. The ideal impedance estimate is the one that minimizes uncorrelated noise. The equation that must be minimized for each frequency and **Z** component is the squared residuals *r* calculated from observed E-fields and the E-fields predicted by **H** through the transfer function **Z**.

Cross- and auto powers of frequencies within a narrow band can be binned together in this step, such that each decade of the spectrum is represented by no more than a small number (typically ~8-10 frequencies). There is always a tradeoff between the number of discrete frequencies over which MT impedances are calculated, and the variance of those estimates, so by binning a larger number of auto- and cross powers over adjoining frequencies over a wider frequency band, a smaller confidence limit can be placed on the resulting impedance estimate but at the cost of the ability to resolve finer scale variations vs. frequency. Using more frequencies allows for more subtle features to be seen, but when site spacing is wide and data

coverage is sparse, which is usually the case, the diffusive nature of EM fields limits how small of a feature and how sharp of a boundary can be sensed, thus the marginal utility of using more frequencies diminishes quickly. It is also sometimes necessary to use fewer frequencies per decade with very noisy data, allowing a broader band of Fourier coefficients to be averaged in each bin. It can also be useful to discard certain frequencies that are noisy in order to avoid having them contaminate the frequency band that they would be binned into.

4. Longer time-series segments are used to estimate impedances of longer periods. Processing time is reduced by using cascade decimation, in which the time-series is lowpass filtered and downsampled, and the previous steps are then repeated.

Additional steps can be followed to improve the quality of the impedance estimates. In this method of MT data processing we are assuming that the data are drawn from a normal distribution, but this assumption is usually violated. Outliers are considered to be data drawn from a different population than the main population, and ordinary least-squares fitting can give outliers a strong influence over the final impedance. Outliers must therefore be downweighted using a robust regression method to reduce their influence. One approach to this is Huber weighting, in which data whose residuals exceed some threshold are downweighted based on the size of their residuals. Once weights are determined, the impedance is estimated again using the weighted residuals. This process is repeated iteratively until the residuals do not change significantly (Chave & Thomson, 1989; Egbert & Booker, 1986). Additional weighting or deselection of individual auto- and cross powers can be made on the basis of the coherence between the E and H fields associated with those estimates, or other factors such as violations of the causality between E and H fields that are required for 1D and 2D Earth models (Sutarno, 2005). Robust processing of MT data provides much higher quality impedance estimates (Jones et al., 1989). MT data are usually plotted as apparent resistivity and phase as functions of period or frequency using logarithmic axes (Figure 4).

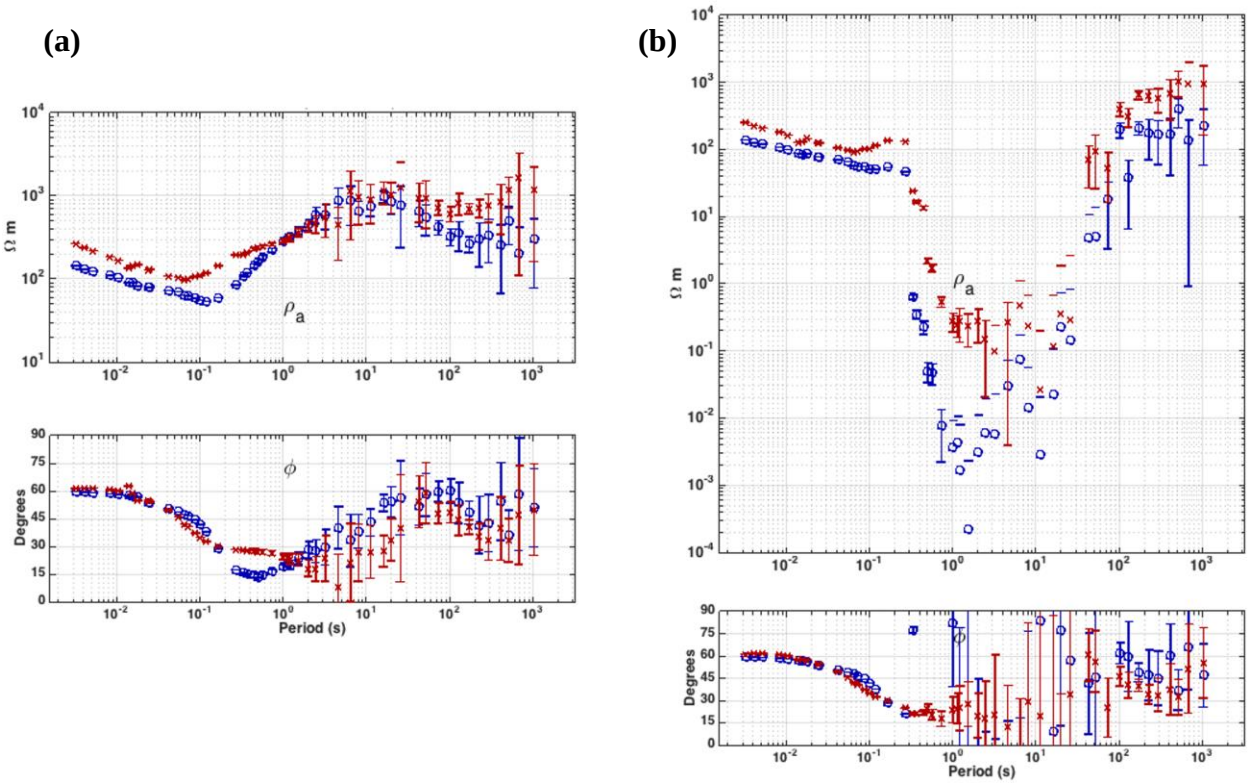

Figure 4. (a) Example of MT data with error bars. Only the Z_{xy} (blue) and Z_{yx} (red) components of the impedance tensor are shown, converted to apparent resistivity (top) and phase (bottom). The slight offset in apparent resistivity at the shortest periods illustrates static shift resulting from distortion. Remote referencing has been used to correct the effects of noise. The uncorrected data are shown in (b). Without remote referencing, the data at periods between about 10^{-1} and 10^{2} seconds reflect noise in the magnetic field data rather than the internal structure of the Earth. After corrections, data quality at periods greater than about 3 s is poor but may be usable. Error bars that extend beyond the axis limits are not plotted. These plots were made by processing approximately 24 hours of time-series data (from dataset of Schultz et al. (2018)).

The effects of noise in MT data can be reduced by using magnetic field data from a second site. Noise at one MT site will not be correlated with the signal at a second MT site if the second site is sufficiently far away from the first. If the magnetic field signal H is the sum of the true regionally coherent magnetic field signal H_{true} and a local noise component H_{noise}, then $H = H_{true} + H_{noise}$. During times of weak geomagnetic activity when the signal to noise ratio is small, the H_{noise} component can make the overall power of H significantly greater. This results in impedances that suggest a more conductive

subsurface in the noisy frequencies. The solution to this is remote reference processing (Gamble et al., 1979). The magnetic field signal does not change significantly over distances that are greater than the scale of most noise sources, therefore two sites will have nearly the same H_{true} but different H_{noise}. Remote referencing keeps only the coherent part of the two magnetic sites, removing incoherent noise from H. Remote reference processing is very important in noisy settings and in low-noise settings during times of weak source signal and should be done whenever possible. It is therefore advantageous to conduct an MT survey with more than one site in operation at all times or with a dedicated remote reference site operating through the duration of the survey. If this cannot be done, it may be possible to use data from a permanent geomagnetic observatory for a remote reference, such as the observatories operated by the Geomagnetism Program of the United States Geological Survey in the U.S. or the global INTERMAGNET Program.

Remote referencing is done by modifying Equation 19 to include the cross powers of the local and remote reference sites as shown in Equation 20:

$$\mathbf{Z} = \langle \mathbf{E}\mathbf{H}_{\mathbf{R}}^{*} \rangle \langle \mathbf{H}\mathbf{H}_{\mathbf{R}}^{*} \rangle^{-1}$$

Equation 20

where $\mathbf{H_R}$ is the remote reference magnetic field. Using remote referencing, incoherent noise averages to zero in the autopower term, eliminating the downward bias in impedance when the signal-to-noise ratio is poor. An example of remote referencing corrected noisy data is shown in Figure 4.

2.6.2 Inversion

The process used to generate models of the Earth from geophysical data is called inversion. Inversion is a major branch of geophysics whose full scope cannot be covered in this paper. This section will provide a short overview of MT inversion. Detailed examinations of 3D MT inversion are given by Egbert & Kelbert (2012) and Avdeev (2005). For a comprehensive review of inversion in general, see Aster et al.

(2013). Inversion is an optimization procedure that seeks to minimize the misfit between the observed data and synthetic data calculated from a geophysical model, subject to constraints. The inversion routine then updates the model to reduce the residuals in subsequent iterations until a satisfactory misfit is reached. For 3D MT inversion, a popular inversion program is ModEM (Egbert & Kelbert, 2012; Kelbert et al., 2014), which implements a nonlinear conjugate gradient algorithm (NLCG; Rodi & Mackie, 2001). The NLCG algorithm uses the gradient of a nonlinear function to find a local minimum. As implemented in ModEM, the function that is minimized (Equation 21) is not only comprised of the data residuals, but it also includes a regularization term that minimizes the deviation from a reference model to avoid abrupt and physically unrealistic boundaries. The reference model is usually a very smooth and simple model, such as a uniform half-space. The inversion multiplies data residuals by an inverse data covariance matrix to downweight the influence of poor-quality data points on the inversion results. Model smoothing is implemented by multiplying model parameters by a covariance matrix that controls coupling of model parameters so that model structures are spread out among adjacent cells and isolated cells of extreme contrast are avoided. The function Φ that is minimized is thus:

$$\Phi(\mathbf{m}, \mathbf{d}) = \big(\mathbf{d} - \mathrm{f}(\mathbf{m})\big)^{\mathbf{T}} \mathbf{C_d^{-1}} \big(\mathbf{d} - \mathrm{f}(\mathbf{m})\big) + \lambda(\mathbf{m} - \mathbf{m_0})^{\mathbf{T}} \mathbf{C_m^{-1}} (\mathbf{m} - \mathbf{m_0}),$$

Equation 21

where $\mathbf{m}$ is the model at the current iteration, $\mathbf{m_0}$ is the reference model, $\mathbf{d}$ is the observed data, f is a function that solves the MT forward problem to calculate synthetic data from the model, $\mathbf{C_m^{-1}}$ and $\mathbf{C_d^{-1}}$ are the model and data covariances, respectively, and λ is a tradeoff parameter that balances data misfit and model smoothness. The inversion treats the data and model residuals as L2 vector norms, $\|\mathbf{d} - \mathrm{f}(\mathbf{m})\|_2$ and $\|\mathbf{m} - \mathbf{m_0}\|_2$, thus minimizing the vector lengths. During inversion, a larger value of λ is used in early iterations to promote model smoothness. As the inversion progresses and $\mathbf{m}$ becomes optimized to minimize $\mathbf{d} - \mathrm{f}(\mathbf{m})$ gradually with each iteration, λ is reduced to a smaller value when subsequent iterations provide minimal improvement in data fitting,

thereby shifting the priority of $\Phi(\mathbf{m}, \mathbf{d})$ toward minimizing $\mathbf{d} - \mathrm{f}(\mathbf{m})$. Gradual reduction of λ helps guide $\Phi(\mathbf{m}, \mathbf{d})$ to a smaller minimum than the local minimum that would be reached using an initially small λ, while suppressing unrealistically large contrasts in model resistivity.

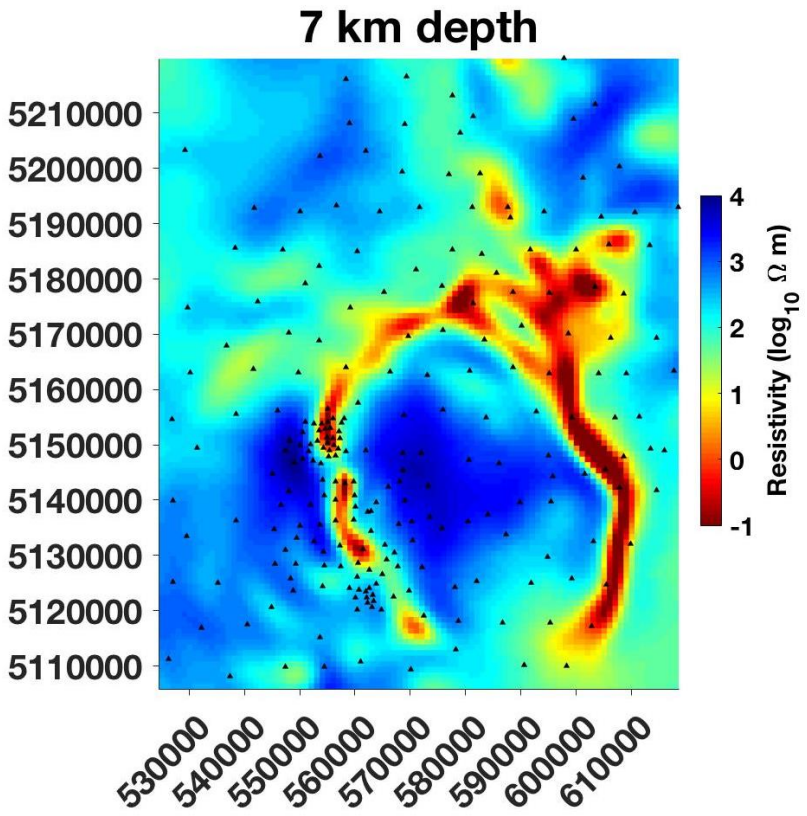

Figure 5. Example of a 3D resistivity model created from MT inversion with ModEM. The arcuate and irregularly-shaped features make it impossible to determine a single regional geoelectric strike direction, making this a good example of a region where 3D MT is highly advantageous. Conductive features are plotted in warm colors and resistive features are plotted in cool colors. Conductors in this model (model used by Bedrosian et al., 2018; see also IRIS DMC, 2018) are interpreted as metasediments in a volcanic region of the Washington Cascades (northwestern USA), while resistive features are plutonic rocks. Black dots represent station locations. A logarithmic color scale is used. Axes in this case are UTM distances, but it is also common to use latitude and longitude or distance from a certain location.

3D models are usually plotted either as cross sections, horizontal slices, isosurfaces, or a combination of these. Most academic researchers studying solid Earth problems use a convention of using warm colors to plot conductive features and cool colors for

resistive features. However, in industry and hydrology it is often the opposite. Therefore, it is important to verify the convention used by looking at the plot's color scale. Color scales typically are logarithmic and usually range within -1 and 4, corresponding to resistivities of .1 Ω m to 10000 Ω m. It is also helpful to adjust color scales to highlight certain features. An example of a resistivity model created by 3D inversion with ModEM is shown in Figure 5 (Bedrosian et al., 2018).

2.7 Resistivity model interpretation

MT inversion results in a resistivity model that represents the properties of subsurface materials, including rock, melt, and pore fluids (aqueous solutions or melt), but determining what exactly each model feature represents requires geologic interpretation. Many things affect material resistivity and this section will provide only a brief introduction to the topic. A comprehensive discussion is provided by Evans (2012). The resistivity of any single common material within the Earth's crust can be as low as 10^{-5} for metallic sulfide minerals (Pridmore & Shuey, 1976) to 10^{12} for a dry basalt (Evans, 2012). Earth materials that MT is sensitive to are never perfectly uniform and should be treated as multiphase materials where the bulk resistivity of most rocks ranges on the order of 10^{-1} Ωm to 10^{4} Ωm. Rocks are made up of crystals and interstitial fluid with varying levels of pore interconnectivity. Within rocks of the upper crust, the fluid component is generally far more conductive than the surrounding mineral grains, and the bulk resistivity depends primarily on the presence of fluids and how thoroughly they are interconnected to enable current flow. The relationship between resistivity of the two phases and their interconnectedness, or "cementation factor," was determined empirically by Archie (1942), in what is known as Archie's Law, given in Equation 22 (with complete fluid saturation assumed):

$$\sigma_{\text{bulk}} = \sigma_{\text{fluid}} \Phi^{\text{m}},$$

Equation 22

where σ_{bulk} is the conductivity of the whole rock, σ_{fluid} is the conductivity of the pore fluid, Φ is the fluid fraction or porosity, and m is the cementation factor, which describes

the tortuousity of fluid pathways. Archie's law requires the assumption that mineral grain conductivity is negligible compared to that of pore fluids. The value of m depends on the rock, and usually a value must be assumed. When m = 1, pore fluid interconnections are uninterrupted and current can flow unimpeded between pores. This is only achieved when crystals are suspended in fluid, such as a high degree fraction partial melt. Common values of m range from 1.5-1.8 in marine sands (Jackson et al., 1978) to 2.5-3 in igneous rocks (Evans, 1994). Unless geologic structures and tectonics suggest otherwise, it is common to interpret areas of low resistivity in the upper crust as highly permeable or having a high fracture density, but there is little that can be said about the rock type. Overall, crystalline rocks have very little pore space and low permeability and thus are highly resistive. Sedimentary rocks can be highly porous and thus have lower resistivities. Shales are also very conductive because of the extremely high surface areas of clay minerals. Charge can flow relatively easily along mineral surfaces, where crystal lattice defects create charge imbalances that are filled by cations that allow for the movement of charge (Evans, 2012). At mantle depths, conductivity can be high despite low fluid content because olivine behaves as a semiconductor, where high temperatures provide activation energy for solid state conduction to occur in olivine (Schock et al., 1989; Constable et al., 1992; Fullea et al., 2011)

Over the large distances that are of most interest in GICs, conductive regions tend to be in tectonically active areas where faulting and volcanism allow for increased fracture density, fluid transport, and clay alteration, in sedimentary basins where clays and water-saturated sediments accumulate, or in areas containing coal or shale beds, or certain ore formations such as banded irons. Resistive regions are tectonically stable parts of continents such as cratons, or areas where bedrock is exposed rather than buried beneath deep sediment. A further complication to interpreting MT data is that geologic materials (e.g. shales) can have anisotropic conduction properties, which can make it difficult within the resolving power limitations of MT surveys to distinguish between the true dimensionality of the resistivity structure and its possible anisotropy. This could have some consequence for applying MT data to the problem of estimating

GICs from geomagnetic disturbances. The impedance tensor contains all measured information on both the dimensionality and the possible anisotropy of the true Earth resistivity structure, so algorithms that project the ground magnetic fields directly through the impedance tensor to predict the ground electric fields used for GIC calculations intrinsically allow for anisotropic effects. Alternatively if anisotropic conditions exist, and ground resistivity models resulting from inversion of MT data that do not account for such anisotropy are used to calculate ground electric fields, it possible that bias might be introduced into the predicted ground electric fields.

2.8 Conclusions

Earth's time-varying magnetic field induces electric fields within the Earth through Faraday's Law and Ampere's Law. Magnetotelluric data is primarily used as a way to determine the electrical resistivity structure of the subsurface, and then making geologic interpretations from the resistivity model. MT uses the ratio of electric and magnetic fields to determine the impedance tensor, which is a transfer function through which the magnetic fields are projected to predict electric fields. Impedance tensors are inverted to produce resistivity models of the Earth. Of interest in GIC studies, the impedance and/or the resulting crust and upper mantle resistivity model is useful for predicting electric fields produced by GMDs that can damage power transmission and distribution networks. Accurate modeling of electric fields requires that 3D effects are taken into account, including distortion. Data acquisition instruments and survey design must be appropriate for the desired spatial and frequency coverage.

Chapter 3: Imaging the internal structure of Newberry Volcano with 3D magnetotellurics

3.1 Abstract

We use 3D magnetotellurics to improve our understanding of the structure and magma composition of Newberry Volcano in Oregon, USA. Newberry is a broad shield volcano with a summit caldera exhibiting strongly bimodal magmatism throughout the Holocene. For forty years, Newberry has been the subject of research for geothermal exploration, but that work has focused on the volcano's west flank, leaving the caldera largely unstudied with geophysical methods until recently. Our modeling shows a relatively resistive magma reservoir with a resistivity of approximately 50 Ωm. Our work builds upon recent seismic models and petrological analysis to interpret Newberry's magma reservoir as a dry rhyolite with no more than 8.7% partial melt. We also image a prominent vertical conductive anomaly along the south rim below the vent that produced the most recent eruption. The anomaly extends from magma reservoir depths of 3 km to 1 km below the surface where it fades into the dispersed conductivity of the caldera fill. We interpret this as the main conduit for magmatic fluids to reach Newberry's hydrothermal system. Other features that our model show include higher conductivity along the caldera rim and a resistive pluton on the west flank.

3.2 Introduction

3.2.1 Geologic setting

Newberry Volcano in central Oregon is located in the Cascade back-arc at the intersection of three major tectonic systems: the northeast-trending Walker Rim fault system of the westernmost Basin and Range province, the northwest-trending Sisters fault zone, and the Cascade magmatic arc, and is close to the Brothers Fault Zone that marks the northern boundary of Basin and Range extension (Higgins, 1973; Hildreth, 2007), as shown in Figure 6. The Newberry volcanic system is a broad shield volcano that features a 5.5 km x 7.5 km rhyolitic caldera elongated east-west at its summit and a northwest-trending rift zone (NWRZ) hosting numerous cinder cones and fissure vents

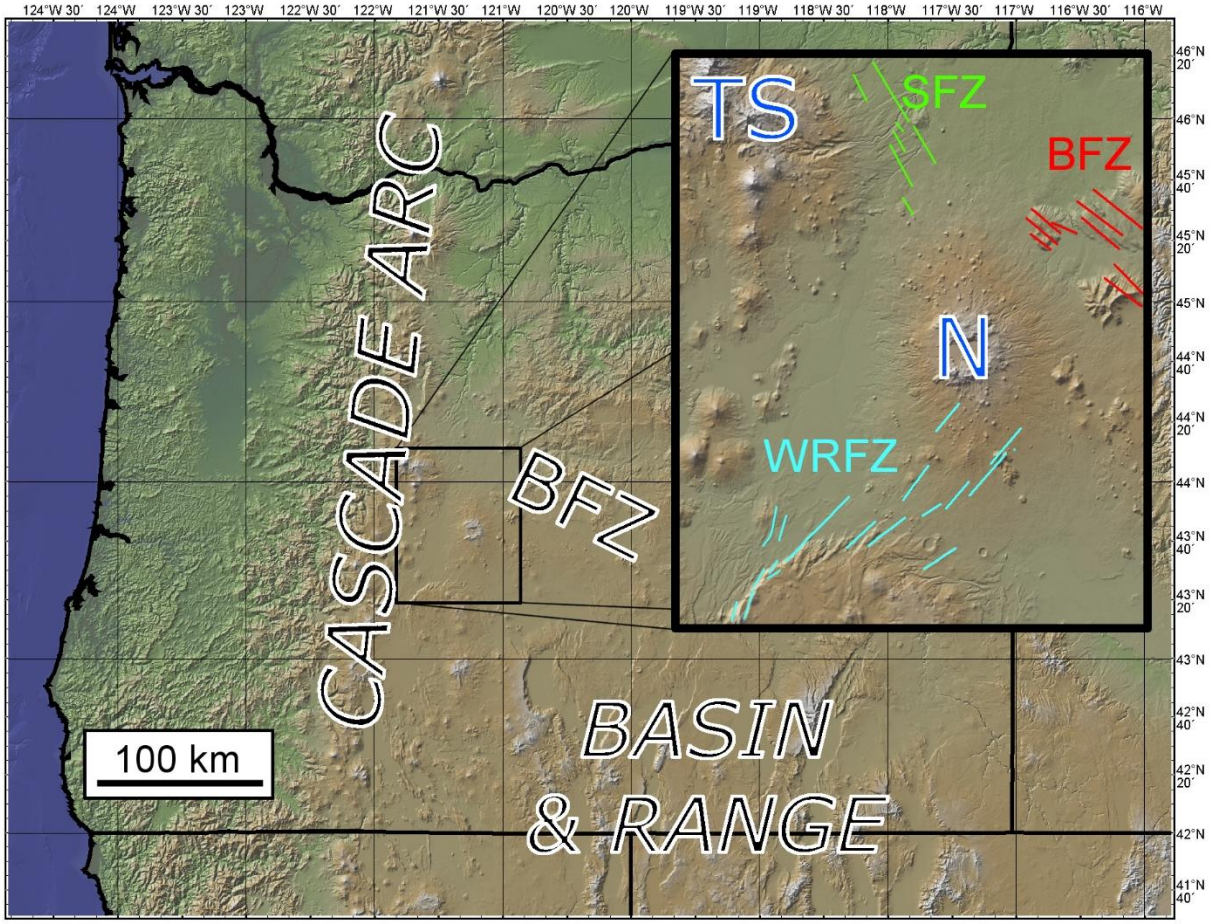

Figure 6. Map of Newberry's location at the intersection of major tectonic systems of the western United States. The inset shows Newberry's geographic relationship with fault nearby fault systems and the Three Sisters cluster of volcanoes in the high Cascades. Faults inferred from topography and mapping (MacLeod et al., 1995). BFZ – Brothers Fault Zone; TS – Three Sisters; SFZ – Sisters Fault Zone; WRFZ – Walker Rim Fault Zone; N – Newberry. Topographic base map generated with GeoMapApp using data from Ryan et al. (2009).

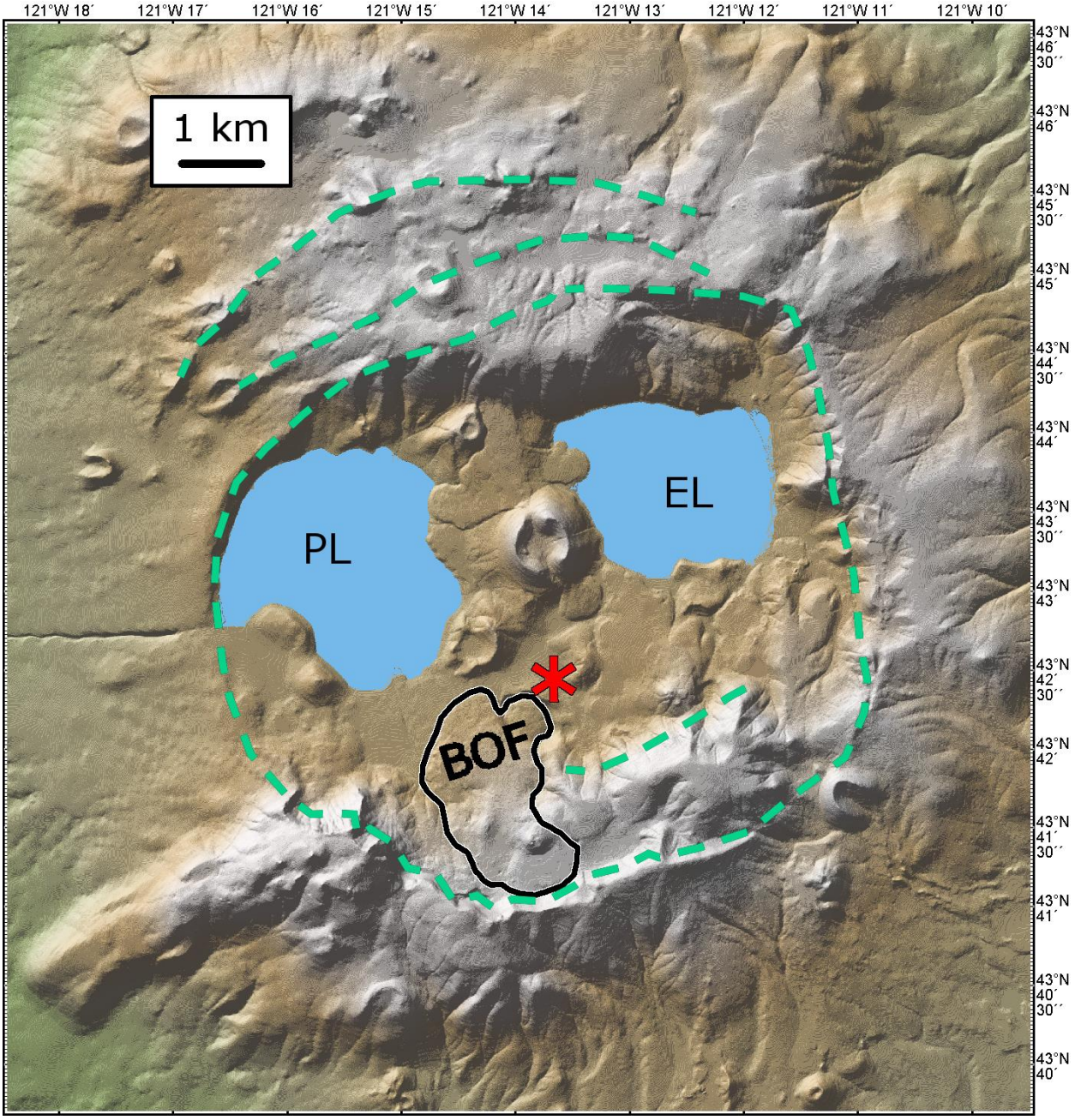

Figure 7. Close-up map of Newberry caldera with major features labeled. Asterisk denotes location of the 932-meter-deep USGS Newberry-2 well. Dashed green line marks caldera rim and fractures from nested collapse structures, inferred from LiDAR topography. PL – Paulina Lake; EL – East Lake; BOF – Big Obsidian Flow. Topographic base map data from Ryan et al. (2009).

of basaltic andesite. The caldera is 50 km east of the linear chain of stratovolcanoes that comprise the main Cascade arc in Oregon and has erupted only rhyolitic lavas during the Holocene, mainly in the form of obsidian flows (MacLeod & Sherrod, 1988) that were preceded by Plinian eruptive phases. The outermost major vent of the NWRZ, Lava Butte (McKay et al., 2009), is 21 km from the caldera rim and 30 km east of the main Cascade arc. The goal of our study is to improve our understanding of the volcano's magmatic, fluid, and structural characteristics using magnetotellurics (MT), a geophysical method for determining subsurface electrical properties by analyzing the Earth's electromagnetic response to changes in the geomagnetic field.

3.2.2 Geothermal exploration

Newberry has been studied extensively as a prospective source of geothermal energy (e.g. Fitterman, 1988; Sammel, 1981; Sammel & Craig, 1983; Swanberg et al., 1988; Swanberg & Combs, 1986; Waibel et al., 2014). The establishment of Newberry National Volcanic Monument in 1990 barred access to the caldera and NWRZ for geothermal exploration and energy production. Thus, research thereafter has focused on the western flank of the volcano, outside of the protected area, where high temperatures and enhanced hydrothermal alteration are observed in boreholes. The source of this alteration is inferred from resistivity modeling using one-dimensional MT and other electromagnetic methods (Fitterman et al., 1988) to be heat from intrusive rock. Later work on the west flank focused on temperature modeling, gravity, and a return to MT with modern methods of analysis. Because these studies emphasized the volcano's west flank, that is the area covered in greatest detail by these geothermal exploration datasets. The models produced by these data were used to help with locating two deep wells on the west and northwest flanks of the volcano, with the west flank well being used for an enhanced geothermal system (EGS) injection study in 2014. With geothermal exploration focusing on the western flank for the previous three decades, only a small amount of recent work has been done toward understanding volcanic processes within the caldera.

Newberry is the largest volcano in the Cascades, with a volume of at least 500 km^3 (Hildreth, 2007), requiring an extraordinary amount of heat to produce such a great melt volume. It is therefore unsurprising that Newberry has been an attractive target for geothermal exploration. Because Newberry is strongly affected by the “rain curtain” effect (Swanberg et al., 1988), where circulation of abundant meteoric water through permeable shallow rock conceals and dilutes shallow thermal features, there are only two mildly hot springs in the caldera (MacLeod et al., 1995) and the hydrothermal system’s properties remain unclear. Downhole temperature measurements have been made at several wells, and only very deep wells have reached conductive geothermal gradients. USGS test well NB-2 was drilled to 932 meters near the caldera center to measure temperatures and sample rock properties below the toe of Big Obsidian Flow (BOF). This hole reached a conductive thermal gradient at 700 m where a temperature gradient of over 600 °C/km was found (Keith & Bargar, 1988; Sammel, 1981). Projecting this gradient deeper into the caldera and considering the abundance of CO_2 and H_2S in well bottom fluids that suggests a magmatic source. Keith and Bargar (1988) determined that a small magma body at 2 km depth is a possible heat source. Another possibility preferred by Sammel et al. (1988) is that this conductive zone is actually a thick cap on a deeper convective zone and that such a high gradient does not continue to great depth. Nonetheless, this well log demonstrates that extremely high temperatures are reached at modest depths at Newberry. Outside of the caldera, deep (> 2 km) geothermal exploration wells drilled 1.5 km from the caldera rim reached conductive thermal gradients of around 124 °C/km and 141 °C/km, while gradients of 98 °C/km and 109 °C/km were observed in wells 3 km from the rim (Bargar & Keith, 1999; D. D. Blackwell, 1994; Bonneville et al., 2016; Frone, 2015; Spielman & Finger, 1998; Waibel et al., 2014). These conductive gradients were reached beneath an upper 200-300 m of isothermal or convective gradients.

3.2.3 Eruptive history

Analysis of tephra deposits, canyon exposures of Pleistocene lacustrine sediment, and sediment cores in lakes in the northwestern United States (Kuehn and Foit, 2006)

reveal 50 distinct tephra units that can be traced back to Newberry during the volcano's approximately 500 ka history. Most of these are from relatively minor eruptions or may represent different lobes of a single large eruption of zoned magma (Donnelly-Nolan et al., 2004). Of these tephras, 13 are deposited distally across five U.S. states (Kuehn & Foit, 2006), including tephras associated with Newberry's most recent eruption, which produced the 1.35 ka BOF. The most recent caldera-forming eruption occurred ~75 ka, with a possible earlier caldera formed at 300 ka (Donnelly-Nolan et al., 2004).

Newberry's Holocene eruptive activity within the caldera is summarized by MacLeod and Sherrod (1988), who report that all eruptions within the caldera were rhyolitic, with both explosive and effusive eruptions. Eruptions had steady recurrence intervals of 2000-3000 years and show similar compositions (Laidley & McKay, 1971), suggesting a common source in a persistent magma chamber that regularly recharges. Outside of the caldera the composition is mafic, with basaltic andesite flows making up the majority of flank material. Geochemical analysis by Carlson et al. (2018) reveals two distinct sources for flank lavas, one tholeiitic and one calc-alkaline. The tholeiitic lavas are dry and underwent anhydrous adiabatic decompression melting at depths less than 70 km. These lavas are interpreted as having a source in the mantle wedge without input from the subducting slab (Carlson et al., 2018). Chemistry of the calc-alkaline lavas is more typical of arc lavas, showing a slab-derived source with input from the mantle wedge during ascent, with chemical signals of input from sediment and mid-ocean ridge basalt. The calc-alkaline lavas contain 2-4 wt % H_2O, and include a component melted within the garnet stability field, at least 70 km deep (Carlson et al., 2018).

3.3 Previous geophysical studies

Geophysical studies of Newberry have taken place since the 1980s using magnetotellurics, gravity, and various seismic methods. Advances in instrumentation and processing methods have produced improved models of the volcano over time. Newberry has also benefited from the variety of different geophysical data types that, along with geologic information, have been jointly interpreted to reveal properties of the

volcano that could not be ascertained by one geophysical method alone. Our study adds modern three-dimensional (3D) MT methods to the interpretation. Previous geophysical modeling efforts have been summarized in a U.S. Department of Energy report (NEWGEN Consortium, 2016).

3.3.1 Gravity modeling

Gravity data acquired on a dense array covering Newberry in 2006 to 2010 (Waibel et al., 2014) combined with regional gravity data (Roberts et al., 2008) were used initially to make inferences of subsurface density from Bouguer anomaly mapping (Waibel et al., 2014). This was followed by additional data collection in 2012 by Zonge International Inc. With the full dataset of 1418 stations, 3D forward and inverse modeling were done to create a density model of the volcano (NEWGEN Consortium, 2016). Station density was greatest around the west flank geothermal area. To better constrain the non-uniqueness inherent to gravity modeling, solutions were sought that matched well log density profiles, core samples, and well cuttings from two deep wells approximately 3 km west of the caldera rim, as well as structures found in seismic tomographic models of Beachly et al. (2012). The final density model has the following features: 1) a low-density caldera-fill zone; 2) a ring of high-density material surrounding the caldera; and 3) a high-density body on the west flank interpreted as a large intrusion. A cross-section through this model is given in Figure 8. The gravity model provides an overview of the volcano's structure that is useful in guiding the interpretation of our resistivity model for the west flank.

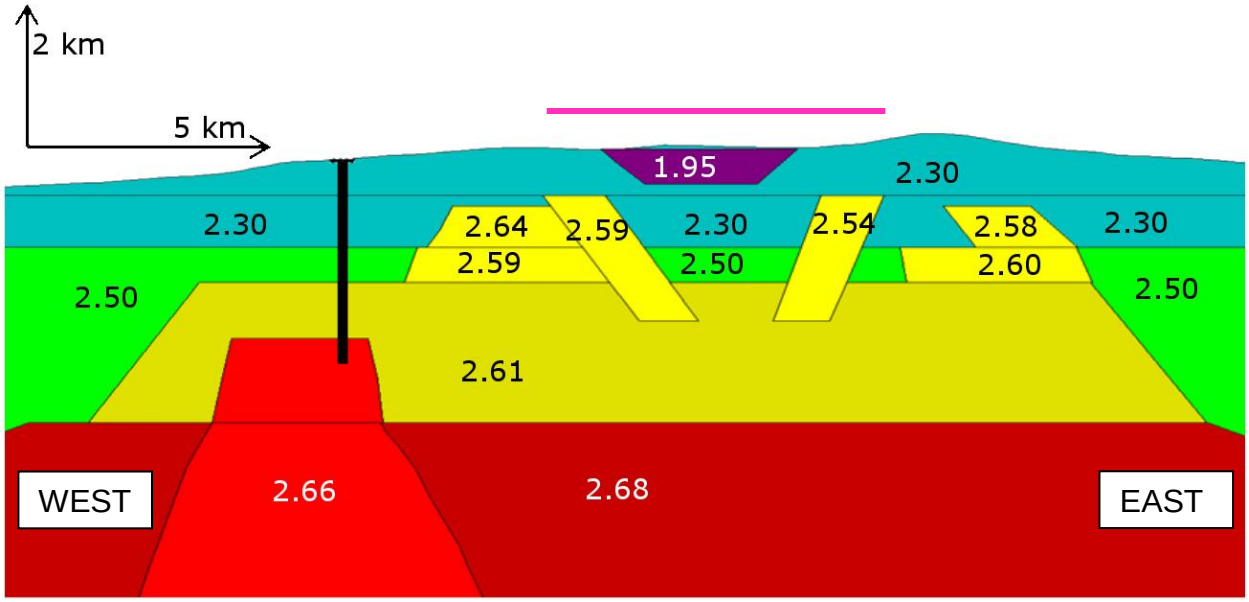

Figure 8. West-East cross-section of density model derived from gravity data (modified from NEWGEN Consortium (2016)). Profile covers the same area as the resistivity profile shown in Figure 11. Numbers give density in g/cm^3. Vertical black line marks location of a geothermal injection well for an enhanced geothermal system project on Newberry's west flank. Magenta line covers caldera .The high density anomaly on the west flank shown here is equivalent to the high resistivity anomaly shown in Figure 10g and Figure 12.

3.3.2 Seismic modeling

Several seismic studies have been conducted at Newberry to image the volcano's structure and the properties of its magma chamber. A 1988 study targeting the magma chamber (Achauer et al., 1988) created a 3D model of P-wave velocity using 120 receivers on a footprint 13 km in diameter centered over the caldera, with an average receiver spacing of 1.07 km. Six explosive sources located 39 km away and three more 89 km away were used as seismic sources in this experiment. Their study revealed low velocity (-8% velocity perturbation) within the caldera that is consistent with a magma chamber and the authors interpret it as such, but the amplitude of the anomaly is not sufficiently large that a magma chamber is required. A hot, fractured pluton could also produce such an anomaly. This study also revealed a ring of high-velocity material along the caldera rim, interpreted as dikes emplaced along fractures. The volcano's

western flank has high-velocities at shallower depths than the eastern flank, showing the influence of the prevailing wind direction on tephra deposition. Higher velocities at shallower depths on the western flank also suggest more intrusions on the west side. However, a P-wave attenuation study by Zucca & Evans (1992) found insufficient attenuation for the presence of a magma body and considered a hot, fractured pluton as an explanation for an anomaly with low velocity but little attenuation.

Building on these studies' results, Beachly et al. (2012) used the previous data and a newly-acquired seismic line to create a new, finely-parameterized, tomographic model to use as a starting model in a waveform modeling experiment. Through their modeling of numerous low-velocity bodies within the caldera, they found a small range of magma chamber geometries that reproduced a prominent secondary phase in the waveforms. This provided constraints on the geometry and melt fraction of Newberry's magma chamber as well as improved imaging of the high-velocity rock surrounding the magma chamber. Further constraints on the magma chamber's properties were provided by Heath et al. (2015), who used a dense array of teleseismic data jointly inverted with the active-source seismic data of earlier experiments to a produce 3D Vp model with a reduction in velocity sufficiently low to require the presence of melt.

3.3.3 Magnetotellurics

Newberry has seen two previous rounds of MT modeling. The first round was done by Fitterman et al. (1988), who also used Schlumberger direct current resistivity soundings and transient electromagnetics to create an array of 1D models interpreted into a model of the volcano's overall resistivity structure by defining depths to layers of contrasting resistivity at different locations. Inside the caldera, a conductive zone was found at depths corresponding to high-temperature hydrothermal alteration. This study found low resistivity in the upper 2 km in the caldera attributed to hydrothermal alteration minerals, with resistive material below this attributed to intrusive rocks, but no conductive material among the intrusive rocks that could be attributed to magma was found.

More recently, an MT study focusing on the geothermal targets of the west flank was done by Waibel et al. (2014). This study used a subset of the data used in our study, including most, but not all of our stations. They used 3D inversion of about half of the stations, focusing on the western flank, with only a few stations in the caldera. Additional two-dimensional (2D) inversions were done along lines that included more stations, which were also on the western flank. They found clear evidence of intrusive rocks on the west flank. Slightly elevated conductivity was found along the caldera rim. Due to sparse station coverage beyond the area of geothermal exploration interest, volcanic features were not well-expressed and received little attention in the model's interpretation.

Our study builds upon the MT work of Waibel et al. (2014) by including more stations and using a finer model parameterization over a wider area to give a detailed image of not only the western flank, but also the caldera and the north and south sides of the edifice. The east side remains too sparsely covered to make meaningful interpretations.

3.4 3D magnetotelluric modeling

3.4.1 Data

Most of our stations come from datasets acquired by Geosystems in 2006 and Zonge International in 2011 for geothermal exploration by Davenport Newberry. The 2006 dataset is the same as that used in the 3D inversions of Waibel et al. (2014). A subset of the 2011 dataset was used in that study's 2D inversions. We used the full 2006 and 2011 dataset as well as data from an array of MT instruments installed by OSU and by Zonge for a continuous MT monitoring study during an enhanced geothermal stimulation experiment in 2014. The 2014 data were processed using the robust remote reference MT transfer function estimation method of Egbert (1997). Neither the original time-series data nor information on processing methods for the 2006 and 2011 data was available. These datasets were interpolated onto a common set of frequencies in a band ranging from 128 Hz to 683 seconds period, for a total of 39 frequencies with eight evenly-spaced frequencies per decade. To cover more of the volcano, we also acquired

five additional stations in the caldera and eastern flank, though these are limited to frequencies higher than 10 Hz. A total of 195 stations were used in the inversion. The full impedance tensor was used with an error floor of 5% on all four components, defined as $.05 * \sqrt{|Z_{xy}| * |Z_{yx}|}$. Vertical magnetic transfer function data were not available for most stations, so they were not used in the inversions.

3.4.2 Inversion

We created our model using the 3D inversion program ModEM (Egbert & Kelbert, 2012; Kelbert et al., 2014). This program uses a non-linear conjugate gradient algorithm to find a resistivity model that minimizes the misfit between the observed data and synthetic data calculated from the model. To avoid isolated model cells with unrealistically extreme resistivity contrast, the optimization penalizes models that deviate from a smooth initial model, which in this case is a uniform half-space with topography.

Topography was modeled as 42 layers with a uniform thickness of 20 meters built upon a half-space foundation made up of 47 layers increasing with depth, where each layer is 11% thicker than the one above. Topographic data came from the global dataset of Ryan et al. (2009).The model uses a horizontal cell size of 250-meter squares over an area 22 km north-south by 24 km east-west in the region where data exist, with cell size increasing exponentially beyond this region. The model has a total of 1.4 million cells, including the air cells used in building the topography. The model is centered over the west flank, where station density is greatest, 3 km west of the caldera's northwest rim. Initial model resistivities of 100 Ωm and 30 Ωm were tested, and we found that the 30 Ωm initial model resulted in a better-fitting final model. This is our preferred model, which we will use in our interpretation. The model's global root mean squared (RMS) misfit is 1.37.

The misfits of individual stations are shown in Figure 9. This figure has each station represented by a circle whose radius is equal to the RMS misfit for each component of the impedance tensor, taking the mean RMS of all frequencies. For reference, the

radius of a circle with RMS misfit of 1 is given in the filled green circle in the upper left, and the radius of an RMS misfit of 10 is given by the larger open circle surrounding the filled circle.

Each circle is colored according to Spearman's rank correlation to analyze whether misfit increases monotonically with period. From this we can determine if the model overfits or underfits the low frequencies or the high frequencies. This technique ranks the data points at each station according to their misfits to create a Spearman correlation. A large value of the Spearman correlation means that the data have misfits that increase monotonically with period, which will occur if the greatest misfits are in the low frequencies. If the data follow an opposite trend and misfit tends decrease with period, the Spearman correlation will be large and the high frequencies have more misfit. We calculate a 95% confidence interval that we expect to include most of the data, and those data are colored white in Figure 9. Data outside of that interval are colored either blue, for larger misfits in the long periods, or red, for larger misfits in the high frequencies. The benefit to using the Spearman's rank correlation is that the influence of very poorly-fitting outliers is minimized, for only their rank is considered and not the size of the misfit.

From our misfit map we see that most dots are white or blue, indicating that misfit is generally greater at longer periods. There are no exceptionally poorly-fitting regions in the model, but the largest misfits tend to be in areas with the highest station density. This high misfit could be due to the station spacing being only slightly greater than the cell size, preventing the model from changing freely to fit every station's data.

3.4.3 Final model

Outside of the caldera, our model's electrical resistivity structure is similar on a general level to that observed by Fitterman et al. (1988) using 1D electrical methods and MT and the 2D and 3D MT models of (Waibel et al., 2014). There is an upper resistive layer a few hundred meters thick, a conductive layer about 1-2 km thick, and a moderately

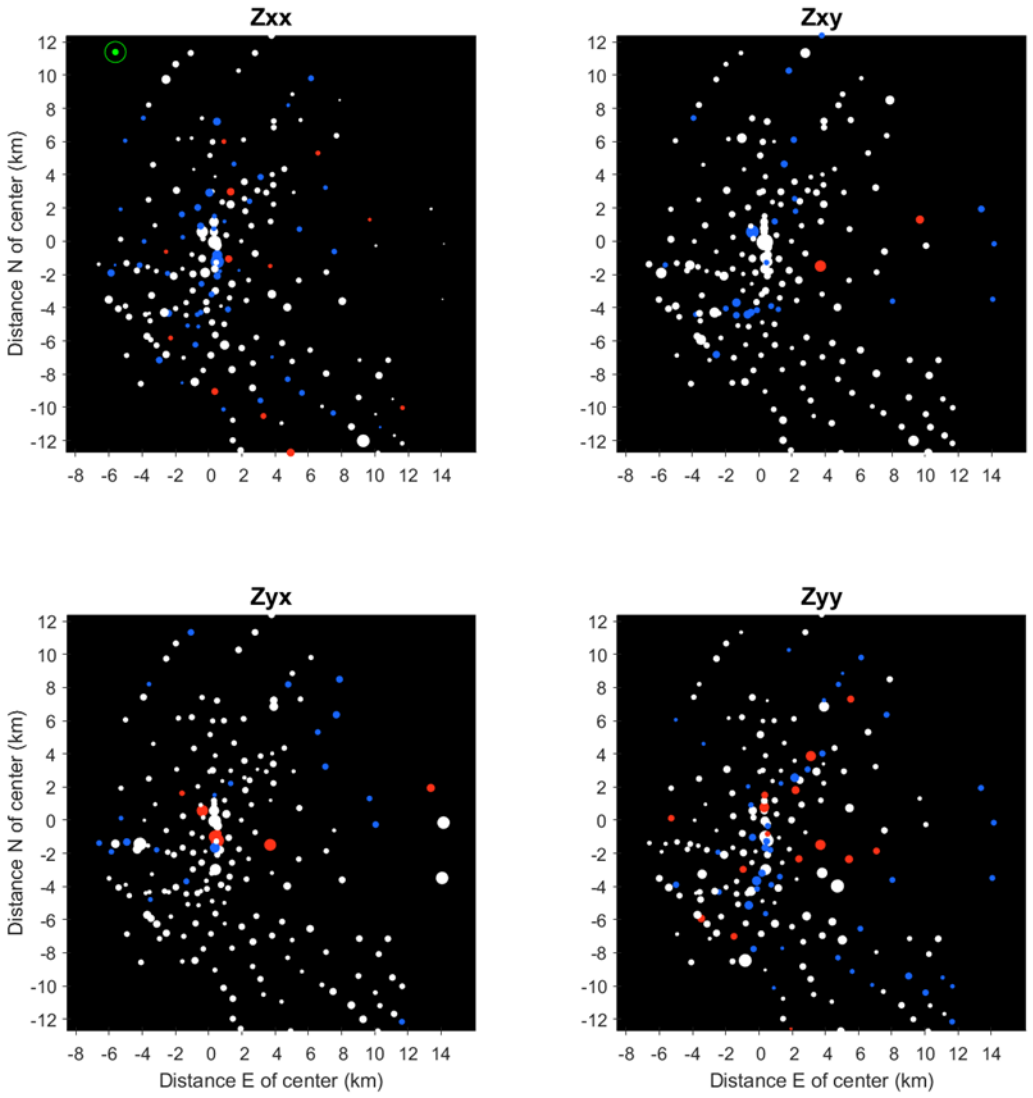

Figure 9. Map of stations and their misfits for each component of the impedance tensor. Circle radius gives the RMS misfit, where the radius of a misfit of 1 is given by the filled green circle in the upper left, which is surrounded by a circle whose radius represents a misfit of 10. The color comes from the Spearman's rank correlation to determine if the misfit increases with period. Blue circles have a very strong correlation and their misfit is in the long periods. Red circles have their greatest misfits in the short periods. White circles do not show a strong correlation.

resistive basement. As in the earlier models, the resistive basement shallows on the west flank at the geothermal interest area.

Our model shows four interesting features in and near the caldera that our discussion will focus on: 1. A resistive body below the west flank. 2. High conductivity along the caldera's west rim; 3. Moderately resistive (50 Ωm) material 3-4 km below the caldera floor; 4. A strong vertical conductor at the south rim. Data coverage on the east side of the volcano remains too sparse to conclusively resolve any structure. Horizontal slices of through our model are shown in Figure 10. A north-south cross-section through the caldera is shown in Figure 11 and a west-east cross section is in Figure 12. Three-dimensional oblique views of the model are shown in Figure 13. These features will be described in more detail in Section 3.5.

3.5 Interpretation and discussion

The layers of contrasting resistivity identified in previous 1D MT work were interpreted as an upper layer of unaltered ash and lava flows, which overlies a conductive middle layer of hydrothermally altered rock, which overlies intrusive rocks (Fitterman et al., 1988). This interpretation of the upper two layers is supported by well logs on the volcano's flanks (Swanberg et al., 1988) and the intrusive lower layer is supported by the geophysical data described previously. The 2D and 3D MT modeling of Waibel et al., (2014) agrees with this, and also shows slightly elevated conductivity below the western caldera rim to depths of 4 km, as well as several lenses of highly conductive material. Their study focused on the volcano's western flank, making no attempt at interpreting the caldera interior. Our model and interpretation are also in agreement with the earlier MT work, but with new detail within the caldera to illuminate properties of the volcano.

Figure 10. Horizontal slices through the model at depths below caldera floor of (a) 0.2 km, (b) 0.5 km, (c) 0.9 km, (d) 1.4 km. Because these slices are at a constant elevation rather than following topography, the west side is at a shallower depth than areas in the caldera and the white area in (a) and (b) is above ground level. The caldera rim is denoted with a dashed line. Black circles denote station locations. Circle size is proportional to station's mean RMS misfit. The star symbol gives the location of the EGS injection well on the west flank near model center. Axis labels give distances in km from model center on west flank. The slice at 0.2 km (a) cuts through the upper resistive layer of unaltered flows and tephra around the west side and in a few areas on the east side where data exist. We expect that this layer encircles the volcano and its lack of continuity reflects data sparseness on the east side. The slice at 0.5 km (b) shows high conductivity along the caldera rim and varying conductivity within the caldera fill. The slice at 0.9 km (c) shows the transition from resistive unaltered rock on the flanks at shallow depths to conductive hydrothermally altered rock farther down. At 1.4 km (d), conductivity dissipates in the caldera and a prominent conductor appears on the south rim. At 1.8 km (e), the only significant conductor near the caldera is on the south rim. At 2.7 km (f), the south rim conductor persists, while outside the caldera, the top of the resistive pluton begins to appear on the west flank below the region of densest station spacing. The locations of the cross sections in Figure 11 and Figure 12 are marked with vertical and horizontal lines. At 3.5 km (g), the south rim conductor fades away and there is no conductivity associated with a magma chamber. The resistive pluton begins to fill much of the west flank. At 5 km (h), there is still no magma conductivity and the west flank pluton is the most significant feature.

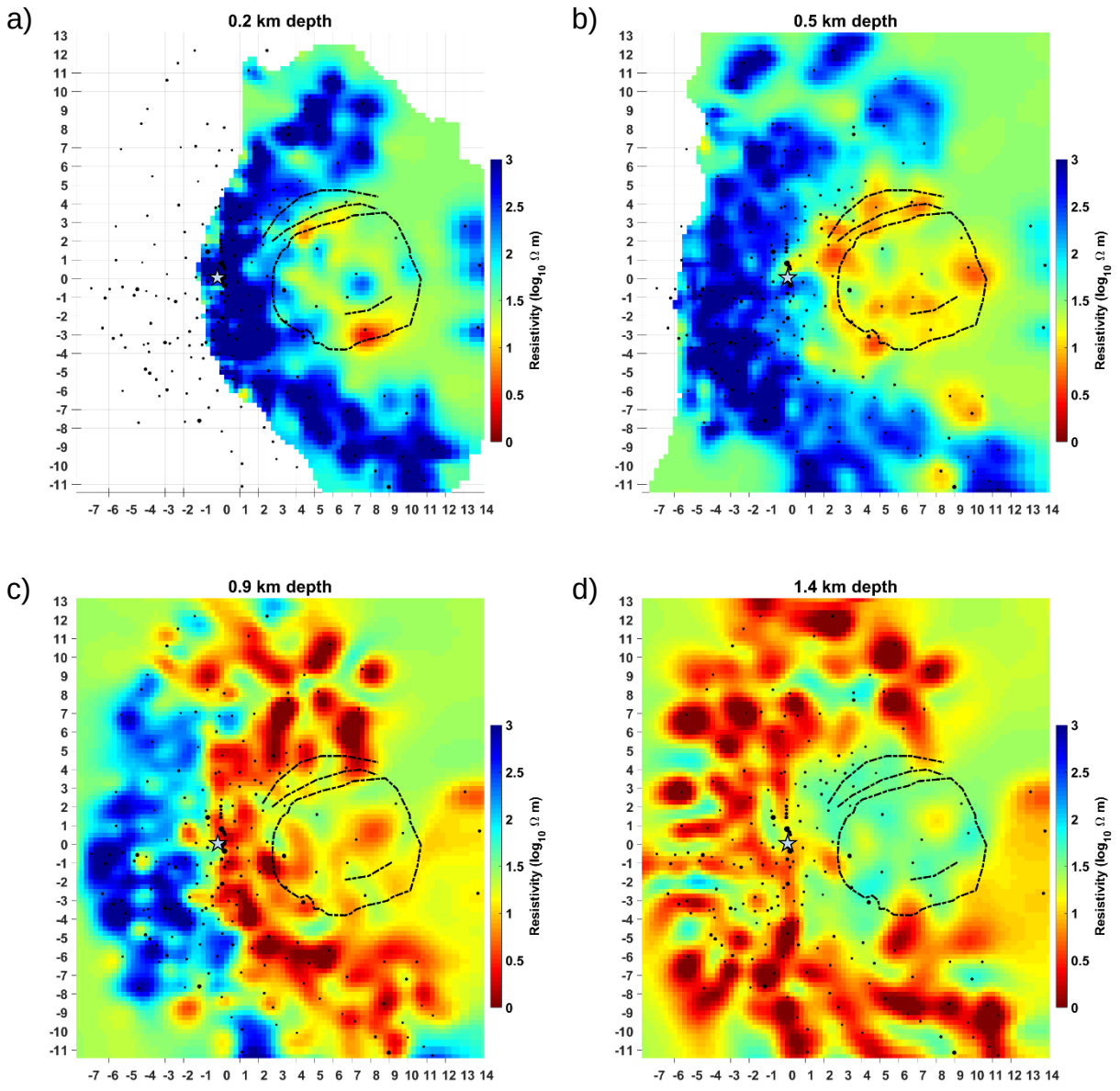

Figure 10 (continued).

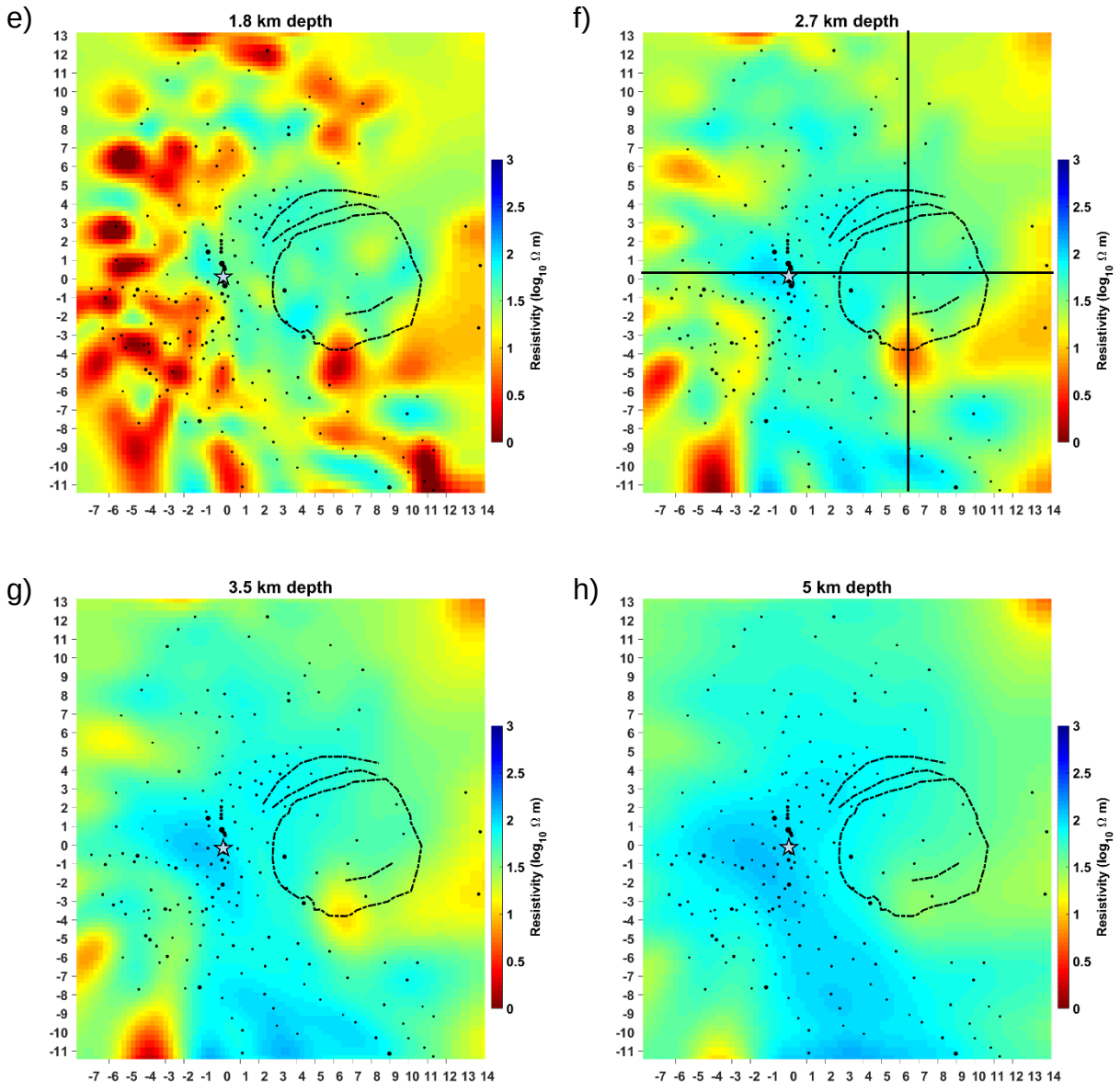

Figure 10 (continued).

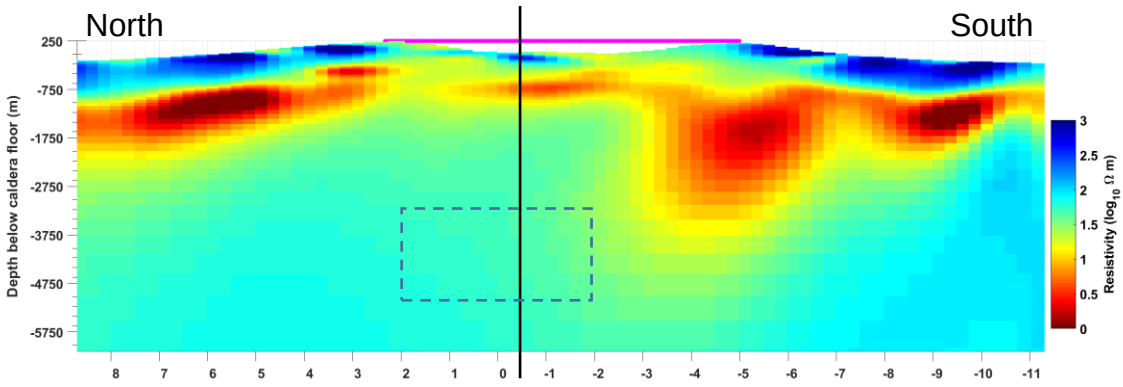

Figure 11. North-south cross-section through center of caldera. Vertical line marks location of west-east cross-section in Figure 6. Caldera rim (magenta) is projected onto plane of cross-section. Dashed line gives location of low-velocity zone interpreted as magma reservoir by Heath (2015). Depths are relative to the caldera floor. The shallowest conductive lens below the north rim represents increased permeability along caldera collapse faults. On the volcano's flanks, the shallow resistive layer of unaltered tephra and flows can be seen overlying the conductive zone of altered rocks. The south rim conductor is clearly visible to approximately 3.5 km depth, but no other structures are present deeper than approximately 1.5 km. This conductor merges with the conductive caldera fill that hosts the volcano's hydrothermal system.

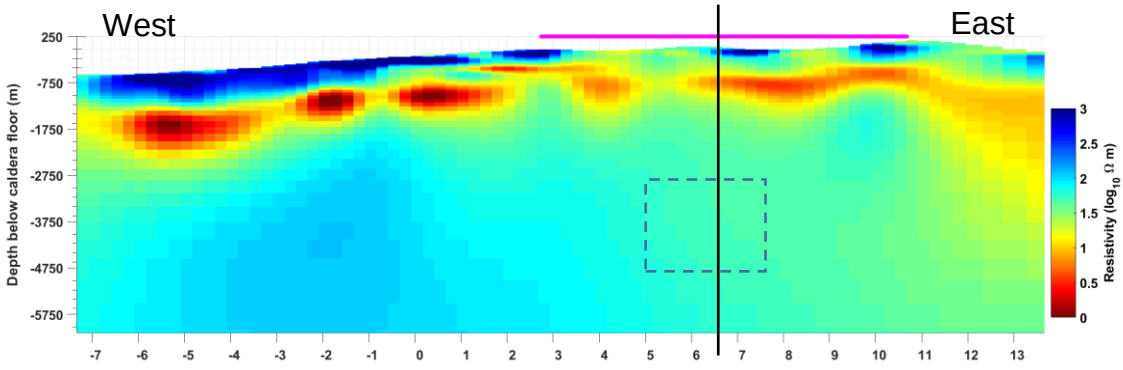

Figure 12. West-east cross-section through caldera, through Central Pumice Cone slightly north of caldera center. Magenta line covers area within caldera. Vertical line marks location of north-south cross-section in Figure 5. Dashed line gives location of low-velocity zone interpreted as magma reservoir by Heath (2015). Shallow structures on flank are likely alteration-related, as in Figure 5. Deep resistive anomaly below western flank is an older pluton that may be responsible for high temperatures in geothermal target area. Within the caldera, no structures are visible below 1.5 km.

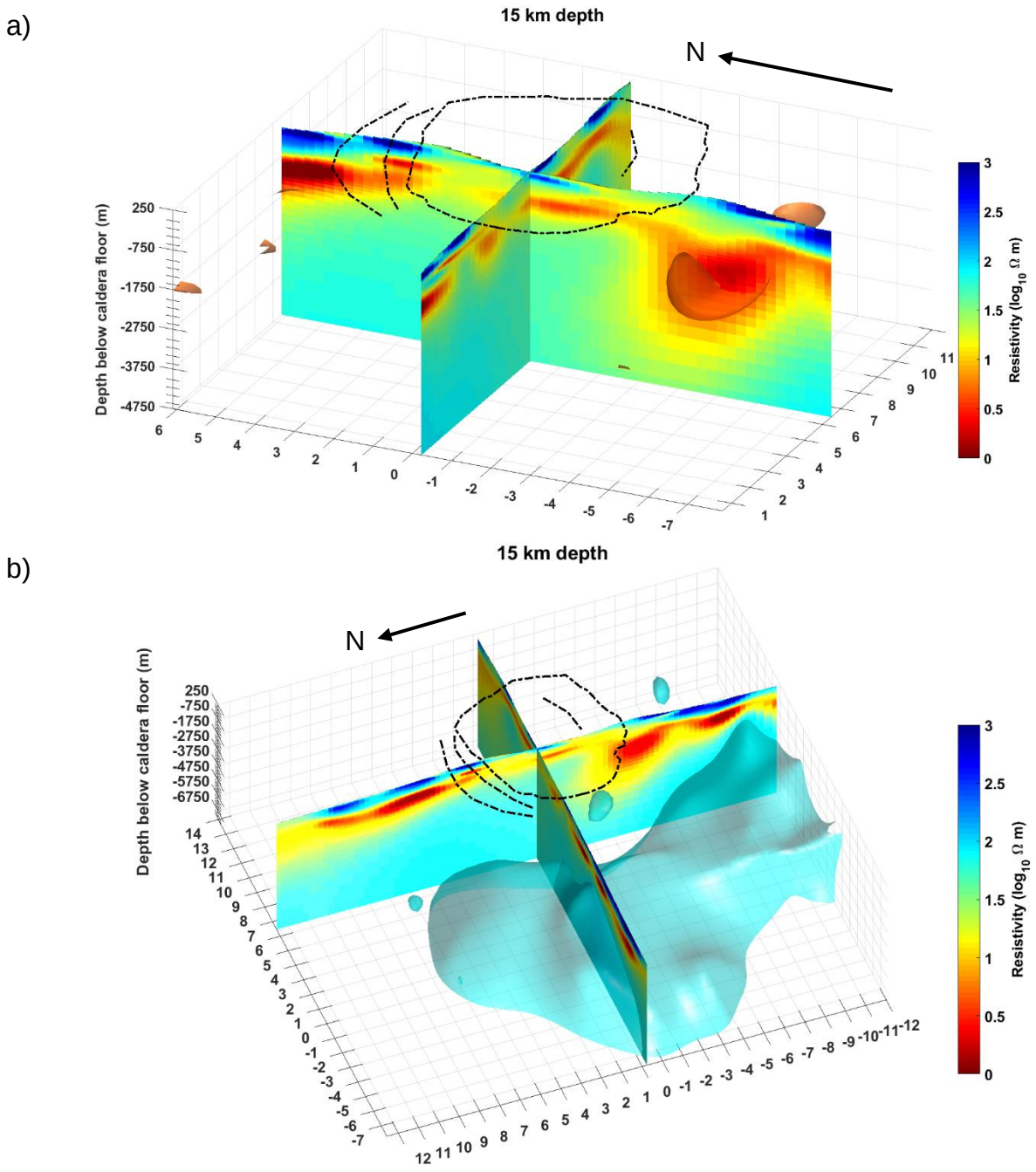

Figure 13. Oblique views of resistivity anomalies. Arrows indicate north direction. The upper 1.5 km was stripped from isosurfaces to prevent shallow features from obscuring deeper ones. The view in (a) shows the south rim conductor highlighted with a 5 Ωm isosurface. The west flank pluton is highlighted in (b) with a 75 Ωm isosurface.

3.5.1 West flank pluton

To the west of the caldera is a resistive zone in an area that overlaps the high-density region inferred from gravity data. Our model shows that this resistive zone wraps around the volcano through the northwest to the west and south (Figure 10f-g, Figure 12, Figure 13). This feature is interpreted as a pluton that is the heat source for geothermal targets on the west flank. It may be from a much earlier stage of Newberry magmatism.

3.5.2 Caldera rim

From the southwest rim near Paulina Peak to the northern areas of the caldera rim near the NWRZ, our model shows a clearly defined arcuate zone of 1-5 Ωm at depths of 400 m to 900 m that overlaps fractures shown in high-resolution LiDAR topography. Along the north rim, LiDAR data show concentric fractures in a zone 4 km wide (Grasso et al., 2012). In agreement, our model shows this area as the widest zone of high conductivity along the rim (Figure 10b). This suggests that high fracture density has allowed for more hydrothermal fluid flow in this region, and thus more alteration. There are no hot springs in this area, so this area is either no longer an active hydrothermal system or the hydrothermal fluids are diluted by meteoric water before reaching the surface.

3.5.3 Caldera fill

Our interpretation of the model within the caldera is informed by the active-source seismic models. At shallow depths within the caldera, our model shows a complex patchwork of conductive and somewhat resistive bodies of 5-50 Ωm in the upper 1.5 km. We interpret this in two ways: first, as a reflection of the sparse data coverage's difficulty in resolving shallow features in an area where station spacing is approximately 2 km; second, as an indication of complex fluid pathways and history of hydrothermal alteration within the caldera fill. The velocity models (Beachly et al., 2012; Heath et al., 2015) also show strong heterogeneity at these depths, though individual velocity and resistivity anomalies show little correlation.

3.5.4 Magma chamber

Deeper within the caldera we examine resistivity of the low velocity region interpreted as a partial melt (Figure 10f-h; Heath et al., 2015).That study used joint inversion of teleseismic and active source data to determine that an elliptical 5 km by 3 km north-south elongated low-velocity anomaly lies in the northern part of the caldera at depths of 3-5 km. The magnitude of the velocity reduction is ~10%, a strong enough anomaly to require partial melt. An explanation for low velocities caused by highly fractured hot rock was proposed by earlier researchers (Zucca & Evans, 1992) based on smaller-magnitude velocity anomalies from earlier modeling (Achauer et al., 1988), but the high porosity required to support the lower velocities found in the newer studies is not realistic at the anomaly's depth, hence the requirement for partial melt. Much of our interpretation of melt properties inferred from resistivity is dependent upon the seismic model's inferred melt, demonstrating the value of complementary geophysical experiments.

Because magma is usually found as a conductive target and the melt zone is somewhat resistive (50 Ωm from a 30 Ωm initial model), the resistivity model alone is not sufficient to require the presence of melt. A fractured pluton is a plausible explanation for our model's resistivity, assuming the temperature is sufficiently high that fractures are filled with vapor rather than brine. A vapor-dominated geothermal system sealed by impermeable clays was suggested as an explanation for high resistivity within the caldera by Fitterman et al. (1988). Fractures filled with aqueous fluids would exhibit low resistivity because of highly mobile ions in the solution, but at high temperatures, electrically-isolating steam makes rocks far more resistive. Laboratory experiments with Icelandic geothermal reservoir rocks (Milsch et al., 2010) demonstrated an increase in rock resistivity by a factor of 20 upon pore fluids transitioning from liquid to vapor. A similar resistivity increase has been shown in sedimentary rocks (Roberts et al., 2001). Such rocks would no longer appear as a conductive target, making a vapor-dominated hydrothermal zone within a hot, fractured pluton a plausible interpretation of our model's resistivity, had the seismic model not been available.

The resistivity of most rocks depends upon the resistivity of the interstitial fluids and how well the fluid-filled porosity is interconnected, not upon the minerals that make up the rock (Archie, 1942). Resistivity of rock saturated with hydrothermal fluid has been inferred from MT models as 1 Ωm below the crater of Unzen, Japan (Kagiyama et al., 1999), 5 Ωm at Tatun, Taiwan (Komori et al., 2014), 0.1 Ωm at the Kirishima volcano group, Japan (Aizawa et al., 2014), and 0.1 Ωm at Long Valley Caldera, California (Peacock et al., 2016). These fluids are significantly more conductive than felsic melt conductivity determined experimentally by Laumonier et al. (2014). They found the resistivity of dacite melt at 900 °C for 0 to 3.3 wt% H_2O and 0.15 to 2.78 GPa to be between 3 Ωm 20 Ωm, with conductivity increasing with increasing water content and decreasing as pressure increases. Experiments with rhyolite melt in the same temperature and wt% H_2O range, but at higher pressures of .5-1.0 GPa found a resistivity range of 0.8 to 4.7 Ωm (Guo et al., 2016) for pure melt. Partial melt would be far more resistive.

The ranges of pressures and composition used in these experiments do not completely cover the conditions within Newberry, so some properties must be extrapolated and assumptions must be made. First we will assume that the melt composition is rhyolitic rather than dacitic. Considering that all Holocene eruptions within the caldera have been obsidian with 73-74% SiO_2 (MacLeod & Sherrod, 1988) and very similar to each other in major element composition despite 2000-3000 years between eruptions, MacLeod & Sherrod (1988) proposed that a persistent rhyolitic magma chamber is present within Newberry, with intermittent heating by mafic underplating. This leads to a preference for the rhyolite melt resistivity model of Guo et al. (2016). While their experiments' pressure range was higher than Newberry's approximately 100 MPa magma chamber, they suggest that their results can safely be extrapolated to lower pressures based on similar pressure-resistivity relationships for lower-pressure melts of other compositions in earlier studies. Using a rhyolitic melt instead of a dacitic melt makes pure melt more conductive by nearly an order of magnitude for dry melts and makes little difference for wet melts (Laumonier et al., 2014; Guo et al., 2016).

Using a minimum solidus temperature of 725 °C at a pressure of 100 MPa (Tuttle & Bowen, 1958), and a rhyolitic composition, resistivity of pure melt ranges from 4.2 Ωm to 0.8 Ωm as wt% H_2O is varied from 0.1% to 4.3%, the water saturation point for granitic magma at this temperature and pressure (Holtz et al., 2001). To accurately determine the melt fraction we must further constrain the water content of Newberry's magma, so we look to the composition of the volcano's deep magma source inferred from geochemical analysis of basaltic andesite flank flows. Recent work has identified two discrete source magmas of different composition: a dry tholeiitic lava sourced from the mantle wedge and an arc-like calc-alkaline lava with 2-4 wt% H_2O (Carlson et al., 2018). Additionally, petrologic analysis of Newberry pumices shows evidence of mixing of dry tholeiitic and wet calk-alkaline sources to form a "damp" magma with 1.5 wt% H_2O evolving to a wetter (2.8 wt% H2O) dacitic magma at 50% crystallization preceding explosive eruptions, and suggesting that further crystallization would produce an even wetter rhyolitic magma (Mandler et al., 2014). We will use our resistivity model and inferences from seismic tomography to further explain the source of Newberry's current magma chamber and to determine the melt fraction.

Water content has a strong effect on melt resistivity, where a dry melt is significantly more resistive than a wet melt (Gaillard, 2004; Guo et al., 2016; Laumonier et al., 2014). However there is a tradeoff between water content and temperature for a given melt resistivity. For example, the solidus temperature of granitic melt at 100 MPa is around 725 °C (Tuttle & Bowen, 1958) . At its water saturation of 4.3 wt% H_2O, its resistivity is 0.8 Ωm. For a hotter and drier rhyolite with 1 wt% H_2O at 900 °C, the melt has a resistivity of 0.9 Ωm. Both melts have very different temperatures and water contents, yet their resistivities are almost the same. Therefore, it is critical that at least one of these parameters is estimated accurately. We will use these petrological considerations in our analysis of the magma chamber's resistivity by finding what H_2O concentrations produce a melt resistivity that allows for a given melt fraction.

Thermal modeling (Frone, 2015) helps to answer the temperature question. Temperature logs in geothermal exploration wells were used to determine the thermal

properties of the volcano. The best-fitting models used a magma temperature of 850 °C at a depth of about 4 km with magma recharge every 200k years, inferred to be the time between the largest eruptions. These models fit the well temperature data within ±5 °C. However, several other models were also found to fit the data nearly as well.

Temperature and water content were estimated from petrologic analysis of obsidian and pumice erupted in Newberry's most recent eruption ca. 1.35 ka (Rust & Cashman, 2007). They estimated a temperature range of 700 to 900 °C with a preference for 850 °C based on coarseness of mafic crystals and the agreement of this temperature with rhyolites studied elsewhere. This temperature also agreed with magma viscosity estimated from bubble geometry and water content. They measured water content in the matrix glass between 0.3 and 1.5 wt% H_2O. Because water solubility decreases greatly with pressure, these magmas almost certainly lost water during ascent from storage conditions. Therefore we will consider the highest measured values to be the minimum water content of the magma reservoir.

A melt fraction of 8-12% was inferred from a 10% reduction in P-wave velocities (Heath et al., 2015). A larger melt fraction was found to be allowable in the waveform modeling of Beachly et al. (2012). Of their preferred models, the one whose geometry most closely matches that of the low-velocity zone of Heath et al. (2015) is the graded mush model. This is a cylindrical body of partial melt 3 km wide by 3 km thick whose top is at a depth of 2.8 km. It ranges from 26% partial melt at the top of the cylinder to 11% at the bottom, for an average melt fraction of 18.4%. Analysis of resistivity gives a smaller melt fraction than either of these seismic studies inferred.

We use Archie's law (Archie, 1942) to estimate bulk resistivity of fluid-filled rock using some assumptions. The formulation of Archie's law used here is $\rho_{bulk} = \rho_{fluid}\Phi^{-m}$, where ρ_{bulk} is the bulk resistivity of the rock in our model, ρ_{fluid} is the resistivity of the melt, Φ is the fluid fraction of the rock, and m is the cementation factor. Cementation factors close to 1 represent rocks whose pore fluids are so well interconnected that electric charge can flow freely with no obstruction by crystals. Higher values represent rocks with more

tortuosity to their porosity. It is unlikely for a solid rock to have a cementation factor less than 1.5, as it was shown analytically (Sen et al., 1981) that 1.5 is the cementation factor of a rock whose grains are perfect spheres. Modeling ellipsoidal grains can give smaller cementation factors in some specific configurations, but generally the cementation factor increases as grain eccentricity increases and moves farther away from the sphere model and toward more realistic models (Mendelson & Cohen, 1982), with values around 2 common for sandstones (Glover, 2009). However, it has been demonstrated that in a partially-molten olivine, melt along grain boundaries forms tubes and sheets of conductive melt in between crystals, providing a relatively open connection more favorable to current flow than the spheres model (ten Grotenhuis et al., 2005). The cementation factor that best represented the olivine partial melt was found to be 1.3. Assuming that crystals in Newberry's partial melt behave similarly, we will also use 1.3 for the cementation factor in our calculations.

Using these values and our model resistivity of 50 Ωm and a temperature of 850 °C, and solving Archie's law for fluid fraction Φ, we obtain a melt fraction of 2.8% for a melt with 4 wt% H_2O, a melt fraction of 4.5% for a melt with 2 wt% H_2O, and a melt fraction of 5.8% using a melt with 1 wt% H_2O. Because these are all below the melt fractions inferred from seismic modeling, there is either a smaller melt fraction, the melt is cooler, the magma chamber resistivity is lower than our inversion predicted, or melt is concentrated in a sill too thin for our MT array to resolve.

Lowering the temperature to 760 °C allows for a melt fraction of 8.0% with 1.5 wt% H_2O, but this is a large deviation from the temperature determined by other methods. A somewhat more conductive magma reservoir would also allow for the desired partial melt. We find that if the resistivity of the magma reservoir was 28 Ωm instead of 50 Ωm, 8.0% partial melt is achieved at a temperature of 850 °C and 1.5 wt% H_2O. 28 Ωm is the most resistive value that allows for all of the parameters to be within the desired range. Lowering it further, say to 20 Ωm, allows for much more flexibility in these parameters, but that is a significant deviation from our model. It takes a much larger deviation of resistivity and/or temperature to reach a melt with high enough water content to have

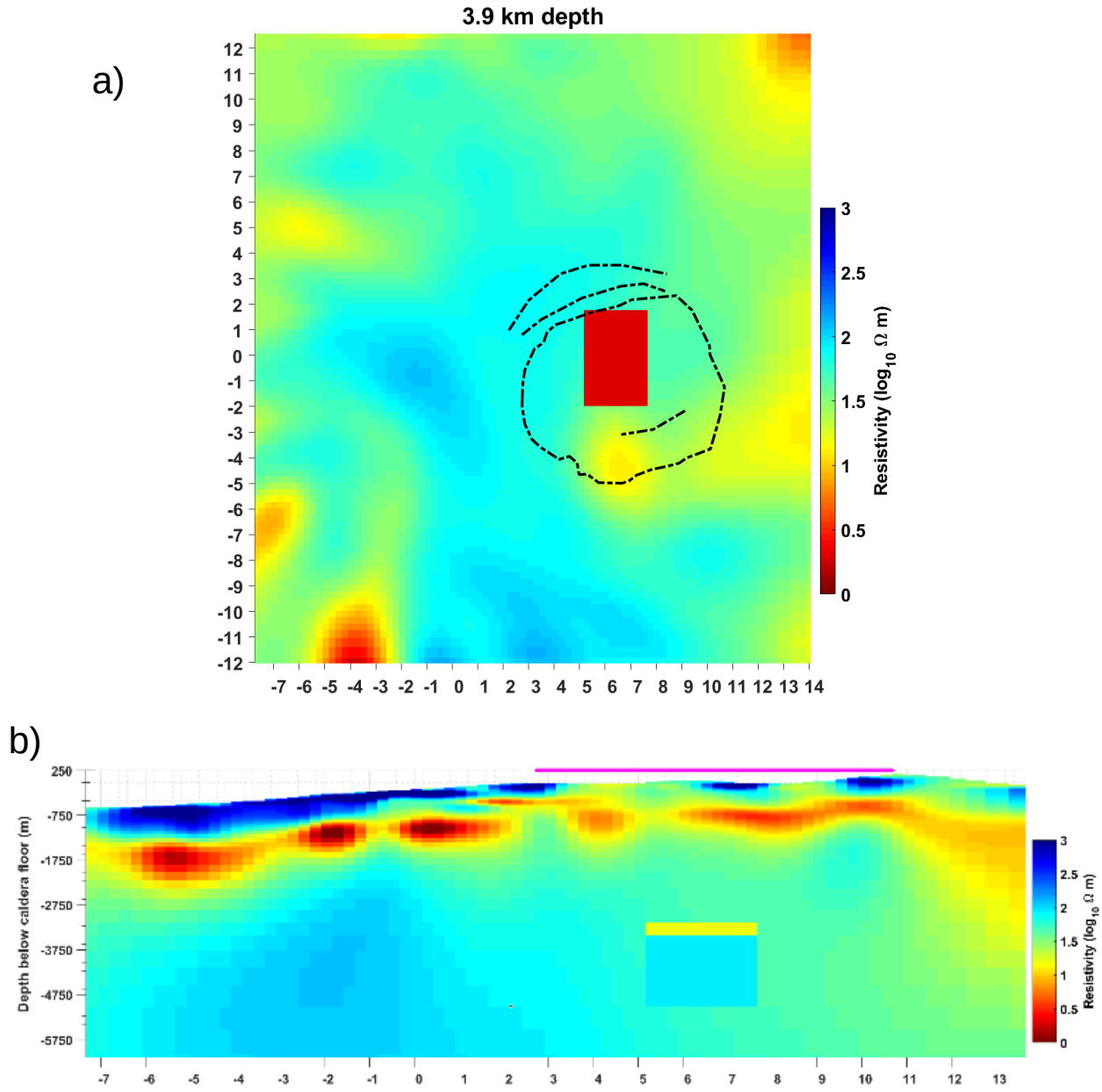

Figure 14. For sensitivity testing, the model was modified to replace the seismically-defined magma chamber with values of different resistivity. The 2 Ωm version used in our testing is shown in (a), with the other augmented models looking similar. An example of the mush sill model is given in (b), which has the same conductance as our inverse model but separated into two bodies of different conductivity and thickness. In this example, the upper layer is 10 Ωm above a 90 Ωm body to represent a higher melt fraction body over a lower melt fraction body.

come from the calc-alkaline source, so it is much more likely that Newberry's current magma chamber evolved from the dry tholeiitic source. We will discuss how sensitive our model is to changes in the magma reservoir resistivity in the next section.

3.5.5 Magma chamber sensitivity

To determine if our data require the magma chamber to have its unusually high resistivity, we ran five tests to see how much the RMS misfit changes as the resistivity of the magma chamber changes. A rectangular body of the same volume as the low Vp body of Heath et al. (2015) was inserted into the model with resistivity of 25 Ωm, 10 Ωm, 2 Ωm, 0.5 Ωm, 150 Ωm, and 1000 Ωm to represent a wide range of melt fractions and fluid conductivities (Figure 14). The magnetotelluric response was calculated from each

of the augmented models and their misfits were compared to the original model, whose global RMS misfit is 1.368. There was no significant difference in global misfit for any of the model augmentations, with RMS = 1.368 for the 10 Ωm and 25 Ωm models, RMS = 1.370 for the 2 Ωm model, and RMS = 1.371 for the 0.5 Ωm model. The 150 ΩM and 1000 Ωm models both produced RMS = 1.365. This shows that even though the data prefer a model with a 50 Ωm magma chamber resistivity, this is no strong requirement as far as the global misfit is concerned. However, most of the stations are on the west flank to cover a geothermal target, and therefore have minimal sensitivity to features within the caldera. Meaningful sensitivity analysis for this dataset requires that a station's distance from the caldera is considered.

Individual station responses show that stations in the immediate vicinity of the magma have a worse misfit with the conductive magma chamber models. Changes in RMS misfit begin to appear at periods longer than 2 s at the stations closest to the anomaly (Figure 15). An MT skin depth calculation for a 2 s period for this anomaly's depth gives an average resistivity of 20 Ωm for the material above the magma chamber, which agrees with the 5-30 Ωm range our model shows in the upper 3 km below this station. Taking the mean RMS error for all frequencies and all four impedance components gives a local misfit of 1.096 for this station. Misfit worsens with the conductive models,

with the 0.5 Ωm, 2 Ωm, and 10 Ωm models giving RMS misfits of 1.164, 1.144, and 1.114, respectively (Figure 15a-c). However, the resistive models show a slightly better local misfit of 1.086 and 1.083 for the 150 Ωm and 1000 Ωm models, respectively. A similar pattern is seen at other stations within the caldera. To determine how meaningful these small differences are, we compare with stations outside of the caldera where sensitivity to magma should be minimal. This is shown in Figure 17, which compares misfit with distance to show if stations closer to the anomaly have a larger misfit than those that are farther away. There is a very clear correlation between misfit and proximity for the conductive models (Figure 17a-c), where stations in the caldera have misfits well above the scatter of the distal stations. Meanwhile, the resistive models (Figure 17e-f) show that misfits for stations close to the anomaly are within the range of scatter for stations farther away, suggesting that the small reductions in misfit for the resistive models are not meaningful and that this dataset is not capable of resolving a resistive target in this area. This low sensitivity is probably caused by a combination of MT source signal attenuation from the conductive caldera fill material and the physical limitation that MT is more sensitive to targets that can produce an inductive response. Sensitivity to the magma chamber is also hampered by sparse data coverage within the caldera.

Another possibility is that the structure of the melt zone is more complex than the MT can resolve, with some parts more resistive and some parts more conductive, but with heterogeneities on an unresolvably small scale. MT is sensitive to conductance, the product of conductivity and layer thickness, which allows a wide range of models to fit the data equally well (e.g. Weidelt, 1985). This was a major challenge in the era of one-dimensional MT where models were necessarily layered, but it can still be a problem in 3D MT in areas where station coverage is sparse, as is the case within the caldera of Newberry. We are assuming a melt zone 2.09 km thick (2.09 km is the closest that our model cell discretization can be to 2 km) with a resistivity of 50 Ωm, giving it a conductance of 41.8 S. The same conductance can be achieved with a melt zone composed of a 334 m mush sill with resistivity 20 Ωm overlying a 76 Ωm partial melt

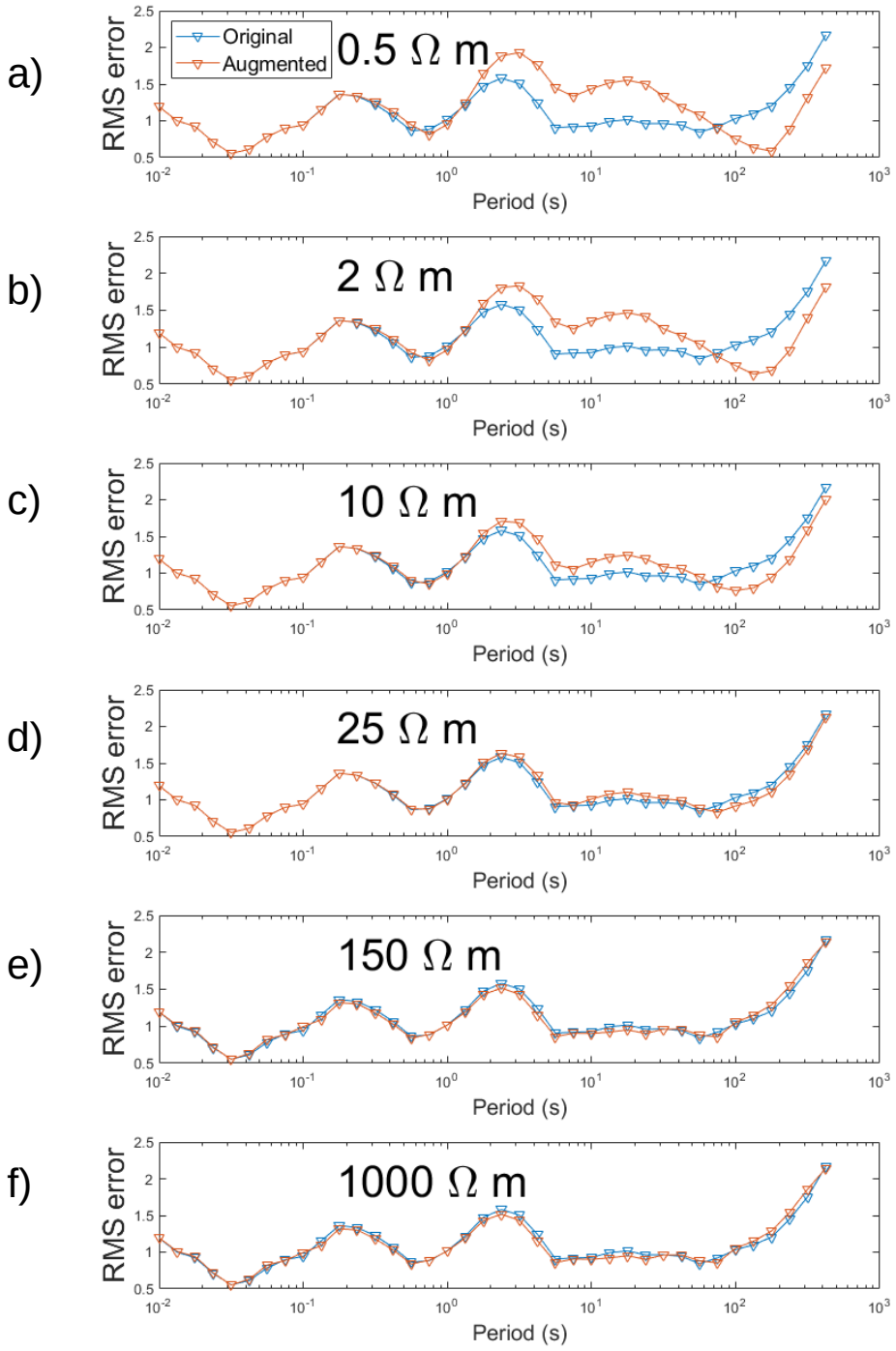

Figure 15. For sensitivity testing, this is a comparison of misfit at a station in the northern part of the caldera, with five different models altered to make the seismically-defined magma body have different resistivities. There is a larger misfit when the model is made more conductive (a, b, c) compared to the original model. The slightly more conductive 25 Ωm model (d) has only a negligible difference in misfit while the more resistive models (e, f) are essentially indistinguishable from the original.

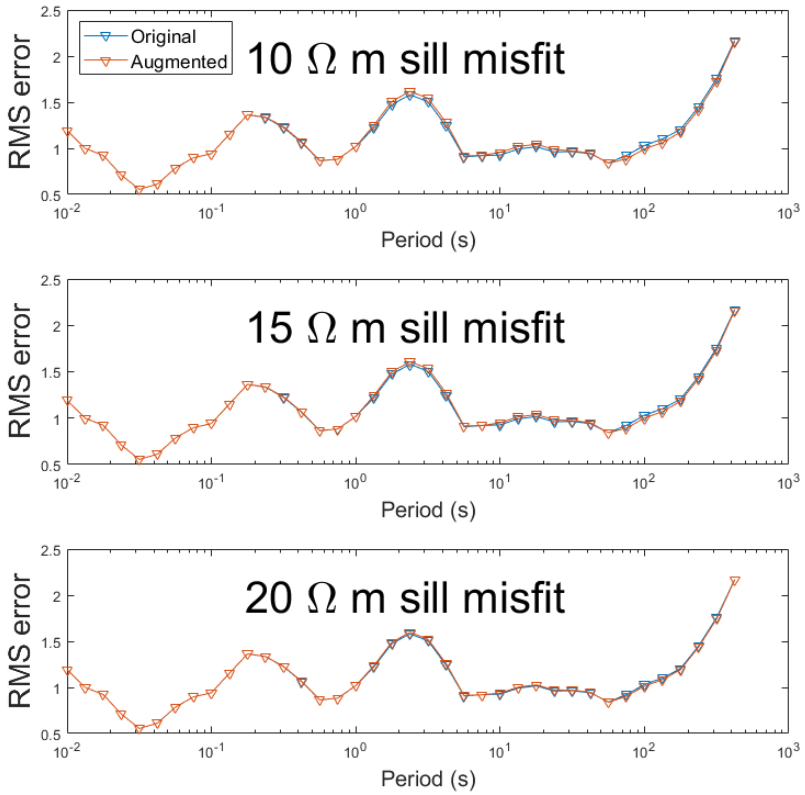

Figure 16. Sensitivity test for heterogeneous melt zone. Similar to Figure 15, but instead of a melt zone of homogeneous resistivity, we substituted a more conductive sill overlying a more resistive zone, that together have the same conductance as the melt zone found in our model.

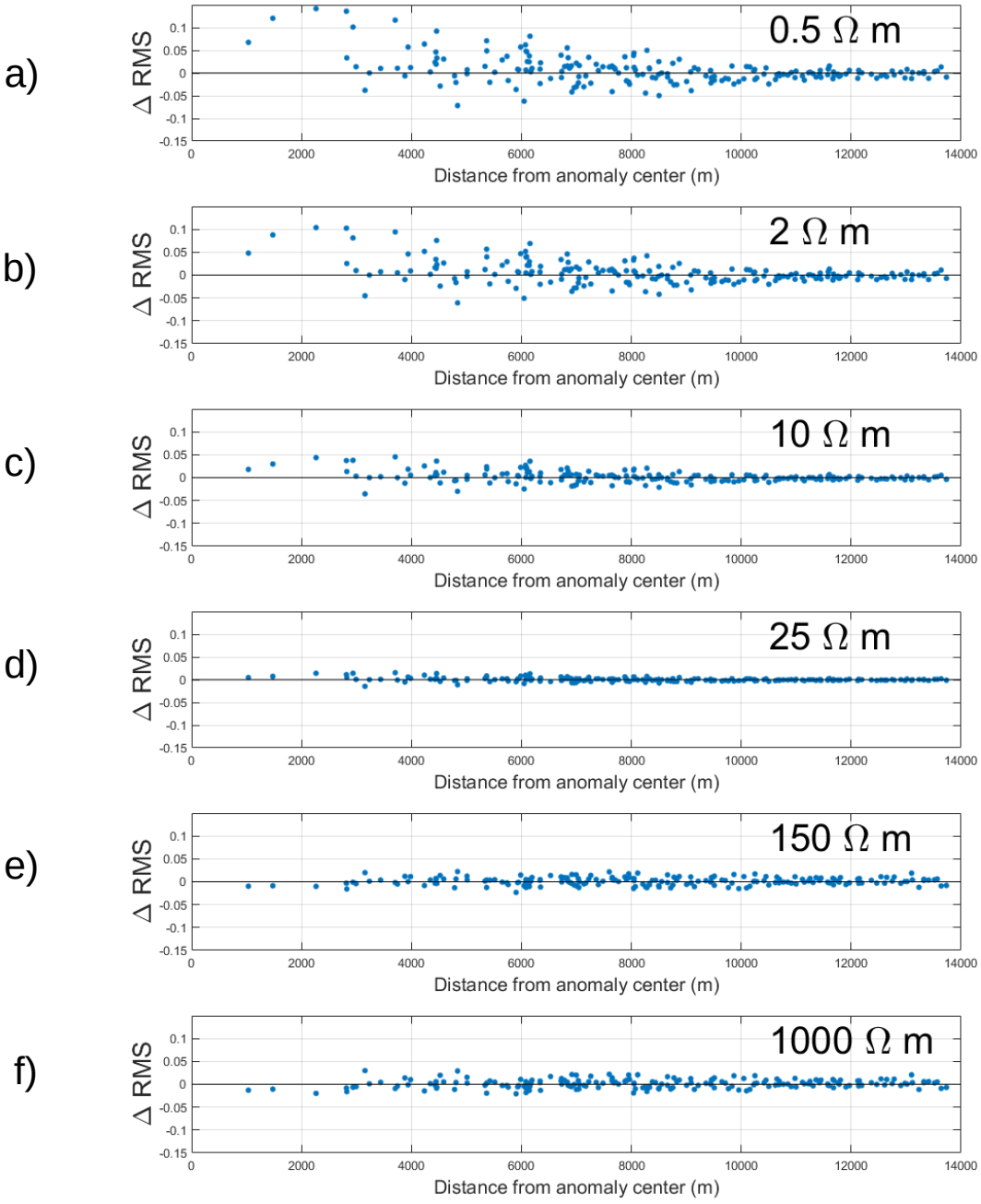

Figure 17. For sensitivity testing, we analyzed how station misfit changes with distance from the magma chamber for the five different test models we used. The conductive melt zone models create greater misfits than the original model (horizontal line at 0), but for the more resistive models, all misfits are within the same range regardless of distance. The most visible difference is the wider variability of misfits at all distances in the more resistive models, with a slight overall increase in misfit at distances greater than 3000 m.

zone 1756 m thick. Changing the resistivities of the sill to 15 Ωm and the partial melt zone to 90 Ωm also achieves 41.8 S conductance, as does a 10 Ωm zone over a 225 Ωm zone. Here we test the sensitivity of our data to these alternative models, with an example shown in Figure 14. For a rhyolitic magma at a temperature of 800 °C and 2 wt% H_2O, the melt fractions for 10 Ωm, 15 Ωm, 20 Ωm, 100 Ωm, and 225 Ωm are 19.7%, 14.4%, 11.5%, 3.4%, and 1.4%, respectively. As shown in Figure 16 for the same in-caldera station analyzed in Figure 15, the difference in misfit is negligible when a homogeneous melt zone is replaced with a heterogeneous one with the same conductance. This raises the possibility that there are pockets of magma with a higher melt fraction, but the heterogeneities are on such a small scale that the MT array is unable to detect them.

It is still interesting that our preferred model used a starting model with a uniform 30 Ωm resistivity and settled on a more resistive melt zone, while inversions that used a 100 Ωm starting model lowered the resistivity to settle at the same value. If the few stations within the caldera lack sensitivity to the melt zone, then the melt zone resistivity must be determined by the ensemble effect of all stations in lowering the global misfit by making the melt zone resistive. Through this analysis, we find that data at stations outside of the caldera are able to influence the model resistivity within the caldera. To examine this effect, we can look at the melt zone resistivity that the inversion arrived at from our two different starting models. From these tests, it is clear that the inversion favors a melt zone resistivity greater than 30 Ωm but less than 100 Ωm, with a preference for 50 Ωm, and not a more resistive anomaly that the single-station sensitivity analysis would suggest. The reason for this can be seen in Figure 17d-f. For the resistive models, although no individual station has a misfit that is noticeably large, there is an overall increase in misfit at all distances from the anomaly. This demonstrates that the resistive magma chamber produces a very small increase in misfit for many stations over a wide area. When the ensemble of stations is inverted, they each provide a small influence toward determining the magma chamber resistivity. This wide-area effect suggests that

it is essential to do MT in three dimensions when attempting to image a resistive body beneath a conductive overburden.

The result of this sensitivity testing is that a conductive melt zone does not fit the data as well as the 50 Ωm melt zone found in our model. However, once the melt zone resistivity is above about 25 Ωm, the differences in misfit become so small as to be negligible. There is also no difference between homogeneous and heterogeneous melt zones of equal conductance. The inversion's preference for a 50 Ωm melt zone is weakly constrained, but it is probably not less resistive than 25 Ωm. Using this resistivity as a minimum, a temperature of 850 °C determined from thermal modeling and petrology, and 1.5 wt% H_2O determined from geochemistry, we can say that the average melt fraction is no greater than 8.7%.

3.5.6 South rim conduit

A prominent feature in our model is a vertical conductive zone of high permeability running along the south rim directly below BOF at a depth of 1 to 3 km with a resistivity of 2 to 6 Ωm (Figure 10e-f, Figure 13a). Its proximity to the BOF vent and the depth of its bottom at magma chamber depths strongly suggest a correlation. Subvertical conductors below eruption sites at Ruapehu in New Zealand (Ingham et al., 2009) and the Kirishima volcanic group in Japan (Aizawa et al., 2014) were suggested to be conduits for magmatic fluids and potentially for magma. The location of our conductive anomaly below BOF and the extremely high temperature gradient of the nearby 932-meter-deep USGS NB-2 well located at the toe of BOF (Sammel, 1981; Sammel & Craig, 1983) suggest that this anomaly also represents a conduit for both magmatic fluids and magma, and plays a key role in Newberry's hydrothermal system and in explaining the extraordinary 600 °C/km thermal gradient measured in well NB-2.

The deepest part of this conductor appears around 4 km depth, but it is possible that the lowermost portion is an artifact of MT's low sensitivity to the base of conductive features. At 3 km depth it is a clear and prominent feature. It continues upward until a depth of 1 km, where it fades and disperses into the shallow conductivity structure of the

caldera. We propose a model in which this is a path for hot magma-derived fluid to rise from the magma chamber until it reaches a depth of 1 km and mixes with meteoric water in the caldera fill rock. It then flows laterally within the formation reached at the lowermost two meters of well NB-2 (930 to 932 m), where high levels of CO_2 and H_2S were measured and alteration was more extensive than at any shallower depths (Keith & Bargar, 1988). This model is similar to the hydrogeologic model proposed by Sammel et al. (1988), whose model relied upon a pipe-like vertically permeable conduit to transport fluids up from magma storage depths into caldera fill deposits. The location of this feature in their model is below the central pumice cone near the middle of the caldera, but they suggest that relocating the permeable structure to below BOF would satisfy their hydrogeologic model's requirements equally well. Our resistivity model confirms that the BOF vent is the source of these fluids and the high conductivity results from a combination of magmatic fluids and high-temperature hydrothermal alteration.

The physical mechanism to allow for a vertical structure with sufficient permeability for pipe-like behavior is the formation of a highly porous rhyolitic foam during magma ascent before eruption. This texture was found from drilling into a feeder vent below an obsidian flow along the Inyo Domes chain on the northwest edge of Long Valley Caldera in eastern California (Eichelberger et al., 1986). Cores through the feeder showed that as a water-saturated magma ascends, lowering pressure causes oversaturation of H_2O resulting in its exsolution into bubbles. Interconnecting bubbles form permeable pathways for vapor to escape from the viscous magma, thereby allowing an effusive eruption rather than an explosive one. A similar foam-like texture at Newberry beneath BOF, even if the foam has collapsed to a breccia, would provide the vertical fluid conduit that is responsible for the conductive anomaly in our model.

3.5.7 Vertical conduit sensitivity

To test whether the data require a vertical column of conductivity at this location, we ran a sensitivity test to determine the misfit with the feature removed. The section of the model with this anomaly was isolated and any model cells whose resistivity was below a

threshold and replaced it with a value typical of the background resistivity in that part of the model, effectively erasing the anomaly. This changed the global RMS misfit from 1.37 with the anomaly to 1.46 without it. Station misfits adjacent to the anomaly significantly worsened. This suggests that the conductive feature is required.

3.6 Conclusions

We use 3D magnetotellurics to explore the characteristics of Newberry Volcano in central Oregon, USA. Our model shows high conductivity along the fracture zone of the upper 500 m of the caldera rim, showing that it has been a pathway for groundwater and probably has undergone hydrothermal alteration. The rim conductive zone is widest in the north, where multiple concentric collapse structures are visible. We also see an unexpectedly high resistivity where seismic modeling has inferred a magma reservoir at depths of 3-5 km, and use seismic and geologic information to infer that the melt is rhyolitic, comes from a dry tholeiitic source, and has a melt fraction of no more than 8.7%. We also image a vertical conductive feature beneath BOF interpreted as a fluid conduit of high vertical permeability along the former route of ascending BOF magma that now feeds hot magmatic fluid to the caldera fill material at a depth of 1 km where it disperses into the volcano’s hydrothermal system. These observations help to further our understanding of this large and complex volcano and demonstrate the value of using complementary geophysical methods and petrologic analysis.

Chapter 4: Conductive trace of the Keweenawan mantle plume imaged with magnetotellurics

4.1 Abstract

North America's 1.1 Ga Midcontinent Rift was initiated by a mantle plume. Upon arrival at the surface, the plume unleashed a flood basalt and caused initial stages of continental rifting. The hot spot track left by the mantle plume is shown through 3D magnetotelluric imaging as an elongated conductive feature at the base of the lithosphere near western Lake Superior at depths of 150-200 km. We present a tectonic model that allows for this feature's continued presence after one billion years as a zone of pyrite-rich sediment subducted during the 1.8 Ga Yavapai orogeny. This sediment was deposited shortly after the Paleoproterozoic Great Oxygenation Event, when the ocean's chemistry transitioned from ferruginous to sulfidic. This would have allowed large amounts of pyrite to be deposited on the seafloor. Low-angle subduction conveyed the sediment far inland beneath Laurentia to underplate the lithosphere. With the mantle plume's arrival, disseminated iron sulfide grains were able to become interconnected by melting, tracing a path of conductivity in the base of the lithosphere. This path abruptly ends at the Yavapai-Mazatzal suture zone that runs east-west across central Wisconsin, where a different tectonic regime no longer allowed for pyrite-rich sediment to underplate.

4.2 Introduction

4.2.1 Mantle plumes

A mantle plume breaching the surface has powerful and lasting effects on the surrounding plate. Perhaps the most visible long-lasting effect is an outpouring of enormous volumes of lava produced when anomalously hot, buoyant, low-viscosity primitive mantle material nears the surface. Plume material and heated lithospheric rock melts to form a large igneous province (LIP) with volumes of 10^5 to 10^6 km^3 during a period of a few million years (e.g. Campbell & Griffiths, 1990; Morgan, 1971; Richards et al., 1989; R. White & McKenzie, 1989; White et al., 1987). Furthermore, dynamic uplift

from a plume impinging on the lithosphere creates horizontal strain that can result in extension and rifting of stable continental crust (e.g. Hooper, 1990; Houseman & England, 1986; Mareschal, 1983; Turcotte & Emerman, 1983; R. S. White et al., 1987). These effects have been observed in several recognized mantle plume locations worldwide (Storey, 1995), including the following: the Iceland plume's effect on Pangea to form the North Atlantic (White, 1992); the influence of the Tristan da Cunha and Saint Helena plume on Gondwana's breakup to form the South Atlantic (Storey & Kyle, 1997); the Réunion plume's rifting of the Seychelles from India (Duncan, 1990; Hooper, 1990); the Yellowstone plume's relation to rifting within western North America's Basin and Range province (Camp & Ross, 2004; Hooper, 1990); and the Keweenawan mantle plume initiating North America's 1.1 Ga Midcontinent Rift System (Hutchinson et al., 1990). Following LIP production, the plume head traces a hot spot track of age-progressing magmatism in the lithosphere parallel to the direction of plate motion, such as the Hawaiian-Emperor seamount chain, the Yellowstone-Snake River Plain system, and many others throughout the world (e.g. Morgan, 1971). The geophysical expression of the Keweenawan mantle plume's hot spot track at the base of the lithosphere beneath North America is the focus of this paper. We present an electrical resistivity model from magnetotelluric data and use its properties to make inferences about Proterozoic tectonics, changes in ocean chemistry, and mantle conductivity mechanisms.

4.2.2 MRS rifting

A major effect of the Keweenawan mantle plume is the formation of the Midcontinent Rift System (MRS). MRS rifting took place during a lull in contraction during the 1.3 to 1.0 Ga Grenville collision during the formation of the supercontinent Rodinia. This lull is a hiatus of at least 80 Ma when no orogenic activity occurred (Cannon, 1994). The MRS began with one of the largest flood basalt eruptions in Earth's history, producing an eruptive volume of at least 1.3×10^6 km^3 and most likely about 2.0×10^6 km^3 (Cannon, 1992; Hutchinson et al., 1990). This LIP volume is comparable to the Deccan Traps (Jay & Widdowson, 2008; Richards et al., 1989) at the end of the Cretaceous. The total

duration of rift-related volcanism was from ca. 1110 Ma to 1087 Ma (Paces & Miller, 1993; Swanson-Hysell et al., 2014; Vervoort et al., 2007), with the bulk of magmatic productivity taking place between 1099 Ma and 1095 Ma (Davis & Green, 1997; Vervoort et al., 2007).

The main rift arm reaches from Lake Superior (LS) southwest to eastern Kansas. It cuts through the southern margin of the Archean Superior Craton and Paleoproterozoic accreted terranes that lie to its south (Whitmeyer & Karlstrom, 2007), rifting this part of the continent in a manner consistent with a short-lived mid-ocean spreading center (Merino et al., 2013). Matching magnetic anomalies on both sides of the rift indicate at least 60 km of spreading in the northern part of the rift in Minnesota, near where spreading was greatest (Chandler, 1983). A second rift arm extends southeast from LS across Michigan and Ohio, though it is not expressed as clearly as the main arm due to strong deformation during the Grenville orogeny (Dickas, 1986; Van Schmus & Hinze, 1985) and smaller magma volumes than the main arm. The second arm has been proposed to be either a second branch of rifting or the result of magmatism from a leaky transform coming off of the main rift (Merino et al., 2013). A third branch of the rift is weakly expressed to the north of LS as a region of north-south-oriented dikes and sills of Keweenawan age (Franklin et al., 1980; Perry, 2004). The main rift region has remained stable since 1060 ± 20 Ma, when Grenville compression reactivated the rift-bounding normal faults as thrusts, uplifting the rift axis basins as horsts, resulting in up to 30 km of crustal shortening (Cannon, 1992, 1994). No post-Grenville deformation events have affected the rift.

4.2.3 Geophysical studies

Phanerozoic sediment conceals most of the rift, with the exposures only along Lake Superior. With limited means to study geology directly, the MRS is an attractive target for geophysical study. Its associated anomalies are clearly visible in gravity and aeromagnetic data (Chandler, 1990; King & Zietz, 1971; E. Thiel, 1956) as one of the most prominent features in North America. Several seismic profiles have traversed the

rift, showing a total crustal thickness of 55 to 60 km, with 20 to 30 km thickness of basalt and sedimentary rift infill overlying syn-rift intrusives (Behrendt et al., 1990; Cannon et al., 1989; Tréhu et al., 1991). Recent MT investigations have examined details of the rift and conductive sutures adjoining Proterozoic accreted terranes cut by the rift (Bedrosian, 2016; Schultz et al., 2014; Wunderman et al., 2018; Yang et al., 2015). Our study uses MT to examine the mantle plume that initiated the rift and presents the first images of its hot spot track along the base of the lithosphere, and we propose a tectonic model to explain the anomaly's persistence after more than one billion years of plate motion.

4.3 Keweenawan mantle plume

Various models of mantle plume morphology have been summarized (e.g. Griffiths & Campbell, 1990; Pirajno, 2007; R. S. White & McKenzie, 1995), describing a focused column of high-temperature, low-viscosity material traveling to the surface from the lower mantle or core-mantle boundary, with a leading mushroom-shaped head of intermediate-temperature material that broadens to approximately 1500 km in diameter as it meets the lithosphere-asthenosphere boundary. A plume brings an immense volume of hot material toward the surface, which melts by decompression and produces additional melt by heating of rock. Voluminous melt from the plume head is responsible for the rapid production of LIP volcanism at the onset of plume emergence, while the more focused post-LIP magmatism of a hotspot track is caused by the movement of the plate over the plume's tail (Camp & Ross, 2004; Richards et al., 1989). The MRS flood basalts are consistent with this model, however, there is no surface expression of a hot spot track associated with it. Because of its great age, it is possible that the track has been either masked by overprinting, that exhumation and erosion have obscured it, or that it is buried under Phanerozoic sediment. In such conditions, geophysical methods must be used to detect whatever traces of a hotspot track may exist.

An abundance of petrological and geochemical evidence points to a mantle plume origin of the MRS flood basalts (Hutchinson et al., 1990; Nicholson & Shirey, 1990). It has

been shown that major and trace element compositions of Keweenawan flood basalts and intrusives at Lake Superior are consistent with a primitive mantle source (Keays & Lightfoot, 2015; Nicholson & Shirey, 1990). The magma source is complex, with multiple possible sources that suggest plume magmas have mixed with older crustal material or by a deep subcratonic lithospheric mantle source (Hollings et al., 2007, 2012), perhaps signifying plume deflection by the thick lithosphere of the Superior Craton (Shirey, 1997). The great volume of basaltic lava that erupted also suggests a plume source, as it is unlikely that another mechanism could provide sufficient heat to produce such voluminous magmatism during such a short time (Cannon, 1992; Richards et al., 1989). Mantle temperatures in a plume are elevated 100 to 200 °C above surrounding mantle temperatures (R. S. White & McKenzie, 1995). With secular cooling making 1.1 Ga mantle temperatures 50 to 100 °C hotter than present-day mantle temperatures (depending on assumptions for long-term mantle mixing; Labrosse & Jaupart, 2007; Richter, 1984), temperature estimates of Keweenawan basalts is to be 1500 to 1560 °C with melting depths exceeding 150 km for basalts erupted at the onset of volcanism (Robert S. White, 1997; see also: McKenzie & Bickle, 1988). Late-erupting lavas exposed at LS show a transition to mid-ocean ridge basalt as rifting developed into a spreading center (Shirey et al., 1994).

4.4 Resistivity model

4.4.1 Inversion and results

We used 241 stations from the EarthScope USArray Magnetotelluric Transportable Array dataset (Schultz et al., 2006-2018), acquired by Oregon State University and its contractors. We directly oversaw the acquisition of this publically-available dataset. We also conducted the field work for approximately half of the stations used in our inversions. This direct involvement with all stages of the data collection and management process allowed us to infer reasons for unexpected data quality issues that required many stations to be reoccupied or relocated. We determined that in many cases, data that continues to have low quality or unusual appearance even after relocating is not caused by noise or local effects, but is instead an effect of unusual

characteristics of the subsurface across a large region. Many stations exhibited strong static shifts as well as error bars that rapidly increase with period. This was especially noticeable at stations in the northern part of our array near LS, where there is an abundance of metallic rocks deposited in iron- and sulfur-rich conditions of the Proterozoic ocean. Because of the likelihood that data that could be considered to be poor quality is actually reflective of anomalous subsurface conditions, we chose not to discard data unless serious problems were obvious. We found that the inversion was almost always able to accommodate the strong static shifts and fit unusual-looking data (see Appendix B for model responses).

Data were downloaded from the IRIS Data Management Center's electromagnetic transfer function database (Kelbert et al., 2011). These stations have a nominal 70 km spacing across the regions of the United States that have been covered so far. Our stations cover an approximately square footprint 1300 km wide covering the northern Midwestern United States, from the Canadian border in the north to approximately southern Missouri in the south, and from eastern Nebraska in the west to Ohio in the east. Data were collected in 2011 to 2014. We inverted data on 30 periods ranging from 7 s to 19k s using the program ModEM (Egbert & Kelbert, 2012; Kelbert et al., 2014) to produce a resistivity model. Our inversion uses a grid of cells 15 km square and with varying thickness that increases exponentially with depth. For cells outside of the data coverage region, horizontal cell width also increases exponentially to avoid edge effects. In the x, y, and z, directions, the model has 120, 120, and 77 cells, respectively, with x north, y east, and z down. The model was designed to be sufficiently wide and deep that the data will not sense the model edges. The model is centered on the city of Rockville, Illinois.

We experimented with a wide variety of inversion parameters in over 100 tests that varied smoothing, model grid resolution, data error floors, frequencies used, and starting models. Most successful inversions converged to global normalized root mean squared (RMS) misfits of 3 to 4, typically after O(100) iterations. To produce our preferred model, inversion was done in two stages. The first stage had a relatively high

smoothing factor of 0.5 and ran until an overall RMS misfit of 3.47. The resulting model was used as both the starting model and the reference model in the second stage, and smoothing was reduced to 0.2. This inversion converged to a global RMS misfit of 2.84. Both stages used a 5% error floor, defined as $.05 * \sqrt{|Z_{xy}| * |Z_{yx}|}$ applied to all four impedance components. We note that all major model features are present even when inverting in a single stage. The two-stage approach allows for a smaller RMS misfit to be reached while having an overall smoother final model.

Our final inversions do not include vertical transfer function (VTF), i.e. “tipper” data. We found that inverting VTF data helps significantly with resolving shallow features, and is especially useful for showing that small, isolated features with a width much smaller than one station spacing are actually connected to form continuous, narrow features that span the gap between stations. However, inversions that included VTF data tended to inhibit the expression of deeper features. To determine the sensitivity of VTF data to features at different depths, we plotted the VTF data as induction arrows using the convention of Parkinson (1962), where arrows point toward conductive features. The induction arrows have no coherent pattern at periods longer than 4700 seconds, and were discarded. For the longest useable periods, induction arrows pointed toward conductive crustal features (Bedrosian, 2016) only, with no influence from mantle features (Figure 18). This suggests that there is a depth limit to what our VTF data can sense that is much shallower than what can be sensed by MT impedance data, and that the VTF data have no ability to resolve features in the mantle. We confirmed this by inverting VTF data alone, which recovered structure only within the upper 60 km. Our mantle target is almost directly beneath strong crustal conductors, so it is also possible that the high conductivity of these crustal structures dominates the VTF data at all frequencies, obstructing the view of the mantle features that we are interested in. Because VTF data appears to not be sensitive to features at the depths we are interested in, it was not included in the inverse modeling presented here.

Crustal features of our model agree with those described in previous MT publications

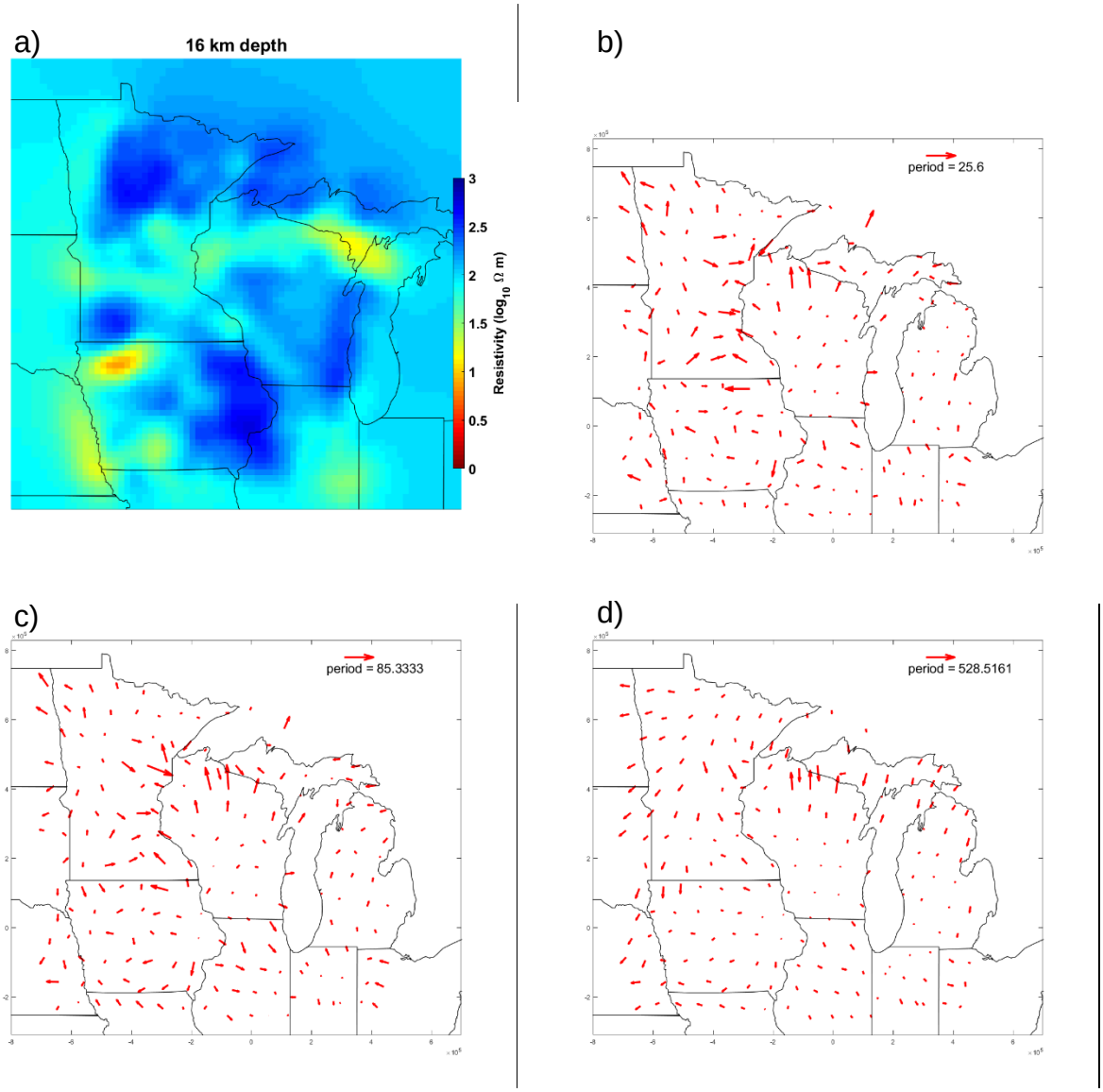

Figure 18. Vertical transfer function (VTF) data are used to produce a resistivity model (a) that shows crustal structures similar to our resistivity model. VTF data are presented as induction arrows in (b) at 25.6 s period, (c) at 85.3 s period, and (d) 529 s period. The arrows become less coherent at longer periods while showing features similar to (d). The arrows appear to be sensitive only to crustal features, with no influence from the mantle.

(Bedrosian, 2016; Yang et al., 2015), and these features will not be described here. Below 80 km, the deepest crustal features have faded away, and at 150 km, a new anomaly begins to appear (Figure 19). It is a linear trail of extremely low resistivity that trends southeast from western LS across northern Wisconsin. Its trend is approximately

parallel to the direction of compression during the Grenville collision (Cannon, 1994). It is approximately 40 km thick, though the depth to the bottom of any conductive anomaly is poorly resolved by MT. Its location intersects the Keweenaw flood basalts and runs close to the deepest basalt accumulation in LS imaged by seismic reflection (Cannon et al., 1989), near where the MRS gravity high broadens significantly as it enters Lake Superior (Thiel, 1956). The coincidence of anomalies in MT, gravity, seismic reflection, and the agreement between the depth of the conductive trend and the calculated depth of melting of the Keweenaw basalt's source rock (White & McKenzie, 1995), as well as the resistivity anomaly's elongation in a direction consistent with plate motion roughly orthogonal to Grenville convergence leads to the conclusion that this anomaly is the fossil trace of the hotspot track left by the 1.1 Ga Keweenaw mangle plume.

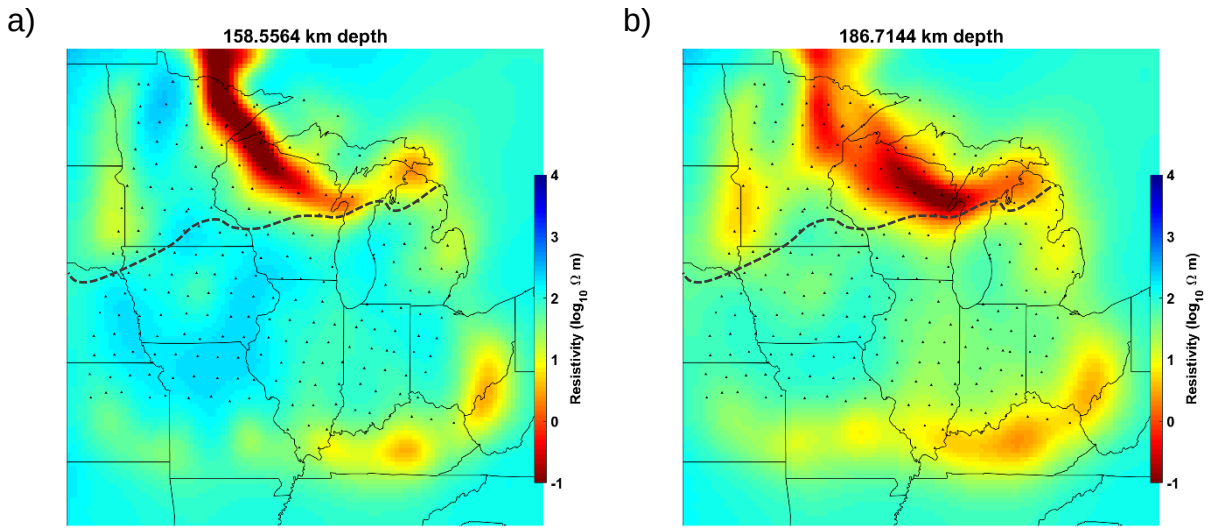

Figure 19. A strong conductive anomaly appears at the base of the lithosphere, shown at two depths, (a) 159 km and (b) 187 km. The dashed line marks the Yavapai suture given by Whitmeyer and Karlstrom (2007).

4.4.2 Anomaly sensitivity

To determine whether the anomaly is required to satisfy the misfit, we calculate the model response with the anomaly removed. If the anomaly is required, the misfit will

worsen. We removed the plume from the model by going through each layer in the depth range of 130-250 km and changing the cells that are more conductive than the layer's average resistivity to a value that slightly more resistive than average, effectively erasing the anomaly. This changed the global RMS misfit from 2.84 with the anomaly to 3.00 without it, suggesting that it is a required feature.

To go beyond this global misfit comparison, we analyze the overall change in misfit at each station. To do this, we first calculate the misfits for both the original and augmented models. We then subtract the augmented misfits from the original misfits to see how big the difference in misfit is and to see whether the original model or the augmented model fits better. The station misfits of the original model are shown in Figure 20, where each station's circle radius is proportional to the difference in RMS misfit and the color indicates whether the misfit is greater in the shorter or longer periods (see caption text). The difference in misfits between the original and augmented models is mapped in Figure 21. A comparison of the models with and without the anomaly is given in Figure 22. The circles are colored so that stations that fit better with the original model are blue and those that fit better without the plume are red. As expected, the largest differences in misfit are in the northern half of the array, where the anomaly is. We also see that most of the stations whose misfit improves by removing the anomaly (red, smaller circles overall) have their misfit changed by a smaller amount than those that prefer to have the anomaly (blue, bigger circles overall). It is interesting that so many stations prefer a model without the anomaly, but they are overwhelmed by the number of stations that prefer the anomaly and by the larger amplitude of the difference in misfit for those stations. We conclude from the increases in misfit both globally and at individual stations that the anomaly is a necessary feature of the model.

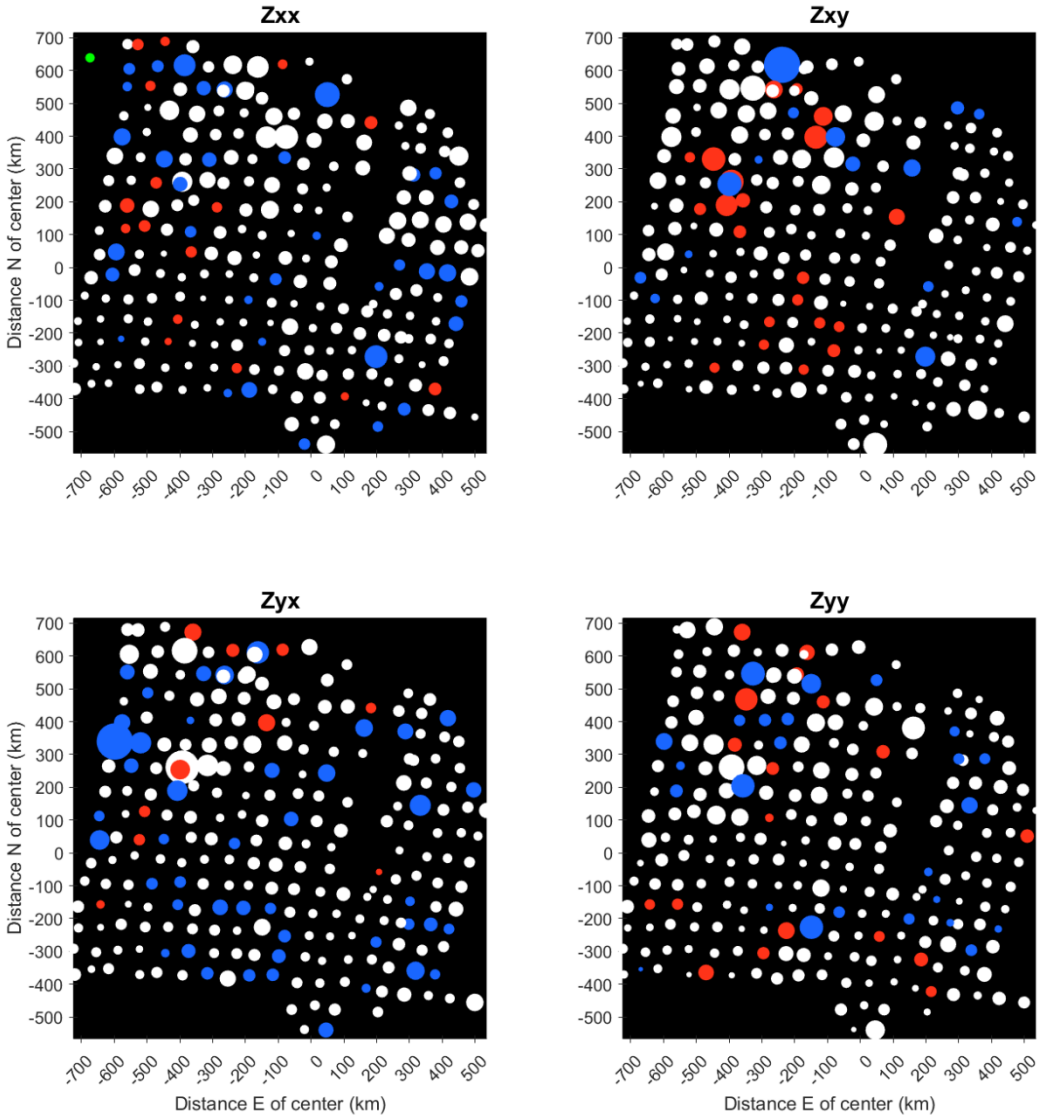

Figure 20. Map of RMS misfits for each impedance component at each station, with the circle radius proportional to the RMS misfit. The green dot in the upper left of the Zxx plot gives the radius for an RMS misfit of 1. The station color indicates whether the misfits tend to be bigger at longer periods (blue), bigger at shorter periods (red), or if there is no trend (white).

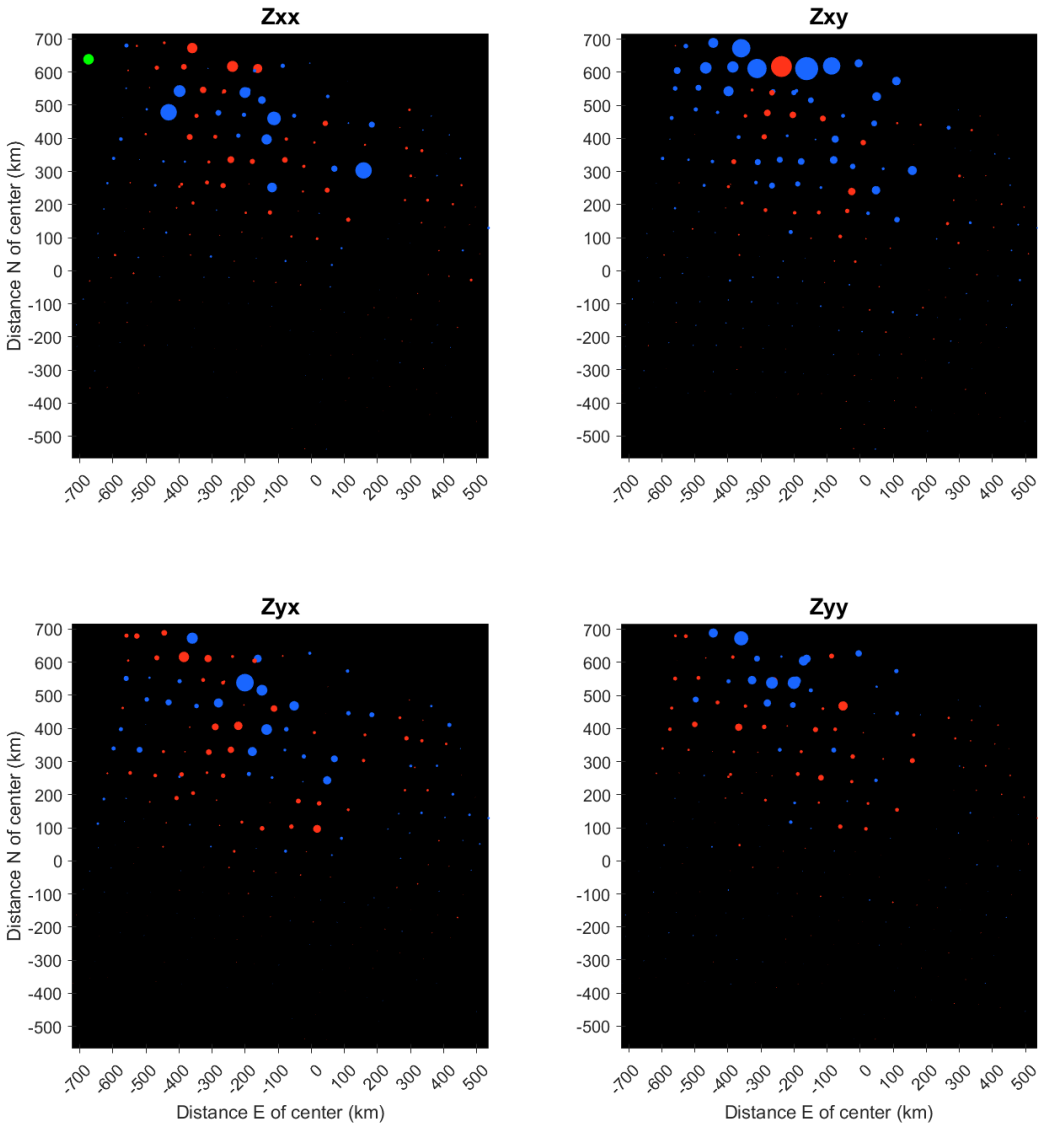

Figure 21. Map of the difference in RMS misfits for each station when comparing the original model and the model with the anomaly removed. The color indicates whether the original model fits better at that station (blue) or if the augmented model fits better (red). The green circle in the upper left gives the radius of an RMS difference of 1.

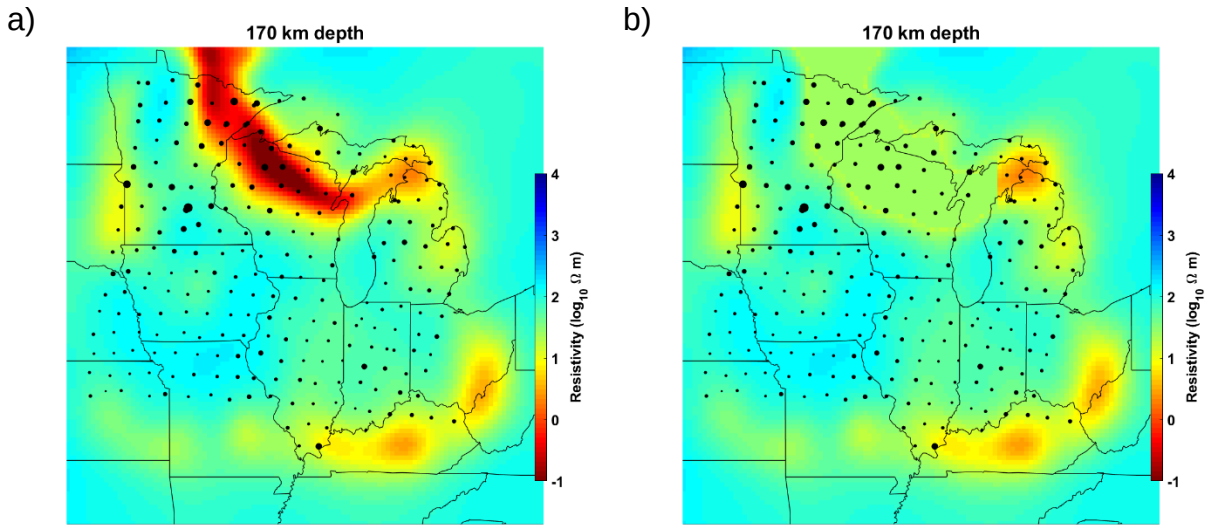

Figure 22. Comparison showing the model with the anomaly (a) and without it (b). Station locations are plotted as black circles whose radius is proportional to that stations RMS misfit.

4.4.3 Model interpretation

Accounting for such low resistivity within the mantle is a demanding task. This anomaly is distinct from the highly conductive Flambeau and related anomalies in the crust near the Michigan-Wisconsin border (Bedrosian, 2016) that were attributed to graphite created from metamorphism of carbonaceous sediment undergoing the high pressure of accretion. It is also distinct from the anomalies associated with conductive suture zones (Yang et al., 2015), which were attributed to graphite and metallic sulfide minerals in the middle and lower crust. Those anomalies are much shallower than what we image and fade out before our anomaly appears. The plume anomaly is too deep to be within the temperature and pressure range of graphite stability, with the graphite-diamond transition at depths of approximately 130-150 km beneath old, cool lithosphere (Stachel & Harris, 2008). This region has very low heat flow of 45-50 mW/m^2 (D. Blackwell et al., 2011). Regions with active tectonics that lead to high conductivity, such as the western United States where heat flow is typically 70-95 mW/m^2 (D. Blackwell et al., 2011), have their high conductivity confined to the upper 60-70 km (e.g. Meqbel et al., 2014), with

exceptions only where major active disturbances are present, such as subduction or hot spot volcanism. No such events have occurred in this region during the previous one billion years, making a heat source from present-day tectonics or magmatism an unrealistic source of conductivity.

Anomalously conductive zones where resistivity is reduced to 10s of Ωm in otherwise resistive upper mantle are often attributed to hydration or refertilization from a tectonic event, such as a mantle plume (Selway, 2014). The anomaly we image is 1-2 orders of magnitude more conductive than this, encouraging us to seek another explanation. A final possibility is deep metallic sulfide minerals, such as pyrite and pyrrhotite, which are present in small amounts in many settings at different depths, but rarely in high enough concentrations to produce significant low resistivity anomalies. With typical resistivity values ranging from 10^{-5} Ωm to 1 Ωm, metallic sulfides are exceptionally conductive minerals (Pridmore & Shuey, 1976). We present a tectonic model where the resistivity anomaly is a body of interconnected sulfide minerals deposited at the base of the lithosphere from mantle plume interaction with ancient subducted sediments.

4.5 Discussion

Interpretation of the deep conductive anomaly requires an understanding of the tectonic history of this region and changes in the fundamental chemistry of the ocean that occurred in the Proterozoic. Our tectonic model requires large amounts of metallic sulfide minerals to be available at 160 km depth, which requires mechanisms for the genesis of sulfides and for their final emplacement in a location accessible to the mantle plume. Our model also requires a mechanism for enhancing sulfide interconnectivity in only the narrowly restricted band that passed over the plume. In this section we will show that conditions were ideal for production of plentiful sulfide minerals in Proterozoic marine sediment, that low-angle subduction occurred in the ideal location to place this sulfide-rich sediment in only the area where the anomaly appears, and that plume temperatures were suitable to melt and interconnect the conductive sulfide minerals to create the anomaly.

4.5.1 Keweenawan sulfide deposits

Magmas associated with metallic sulfide deposits in early stages of Keweenaw magmatism are very high in MgO, suggesting a primitive mantle source with sulfides carried upward from depth as well as sulfides incorporated shallow in the crust (Ding et al., 2010, 2012). These magmas underwent a prolonged period of crystal fractionation and show signs of extremely high pressures from a source within the garnet stability field, at least 70 km deep (Keays & Lightfoot, 2015). We propose that subducted crust that preceded the 1.7 Ga Yavapai-Mazatzal accretion is the source of the deep sulfur that produced these deposits. Furthermore, we propose that deep metallic sulfide minerals remain at depth and are the source of the high conductivity in our model.

4.5.2 Proterozoic biogeochemistry

The occurrence of large quantities of metallic sulfide minerals in subducting sediment requires an ocean whose chemistry is vastly different from the oxygen-saturated ocean of today. Large amounts of iron sulfide would be expected in sediment that recorded the ca. 1.9-1.8 Ga transition from a ferrous ocean to a sulfidic ocean. The arrival of atmospheric oxygen in the Paleoproterozoic Great Oxygenation Event brought increased weathering rates to continental rocks, resulting in a large influx of sulfate to the oceans where it was a nutrient for sulfate-reducing bacteria (Canfield, 1998). When the rate of sulfate reduction exceeded the rate of iron delivery to the oceans, production of the banded-iron formations (BIF)—which developed in shallow ocean settings worldwide during the Archean and Paleoproterozoic—ceased (Canfield & Raiswell, 1999). With the end of BIFs, the iron-saturated ocean gave way to sulfur-saturated conditions, while oxygen levels remained low enough that only the surface ocean was oxic, leaving the deep ocean euxinic (Canfield, 1998; Farquhar et al., 2010; Logan et al., 1995). In large portions of the ocean, virtually all of the iron that would have formed BIFs, as well as most of the ocean's sulfur input from continental weathering, was buried in the seafloor as pyrite (Canfield & Farquhar, 2009). Most of this would have formed in the water column as grains smaller than 10 μm, though diagenetic pyrite formation would also have been possible (Logan et al., 1995). Such conditions no

longer existed following the Neoproterozoic rise in oxygen levels to eliminate euxinic bottom waters in the newly oxic ocean that would support the Cambrian explosion (Canfield et al., 2007) and would be sufficient to oxidize all of the sulfur and iron, eliminating pyrite from younger sediment. A timeline of the chemical changes in the atmosphere, shallow ocean, and deep ocean is given in Figure 23.

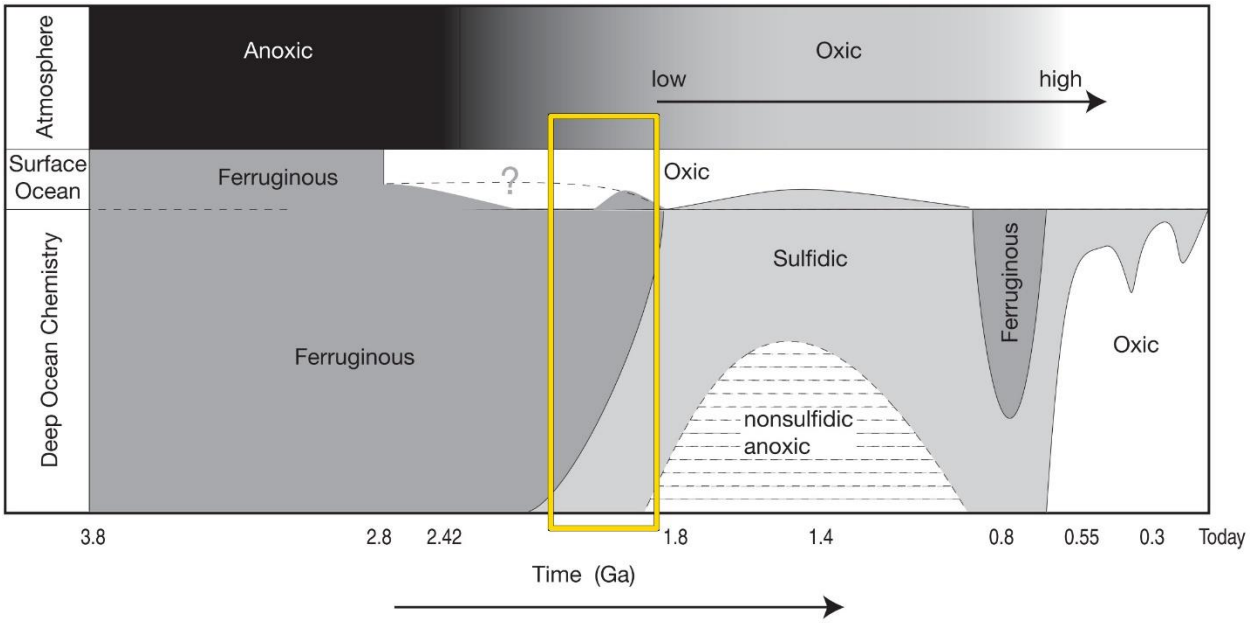

Figure 23. Timeline of significant changes in the chemistry of the ocean and atmosphere from the Archean to the present, modified from Farquhar et al. (2010). The time when the pyrite-rich sediment would have been deposited preceding Yavapai subduction is highlighted in yellow. During this time, ocean bottom waters had become sulfidic.

4.5.3 Proterozoic Laurentian accretion

The formation of the proto-North American continent Laurentia during the Proterozoic occurred as a series of accretions against the Archean Superior Craton, building up the continent from the LS region outward to the southeast. A thorough review of the accretionary and tectonic history of Laurentia is given by Whitmeyer & Karlstrom (2007). The earliest accreted terranes along the southern margin of the Superior Craton made up the ca. 1880-1835 Ma Penokean province that now underlies northern Wisconsin, the upper peninsula of Michigan, and eastern Minnesota (Schulz & Cannon, 2007). The Penokean province resulted from south-dipping subduction south of a shallow sea

between it and the Superior Craton, producing arc magmatism in the Penokean province until it accreted, closing the sea along the Niagara Fault Zone (Holm et al., 2005; Schneider et al., 2002). Following final convergence was a southward jump of the subduction zone (Schulz & Cannon, 2007) and a reversal in subduction direction to north-dipping (Holm et al., 2005). This new subduction zone created a series of intrusions within the Penokean province to produce the ca. 1800-1700 Yavapai orogeny (Holm et al., 2005). Age-progression of ca. 1800-1750 Yavapai intrusions and metamorphic cooling ages shows that arc magmatism from early Yavapai plutonism was much farther inland, close to Lake Superior, and migrated southeast to its final location in central Wisconsin. This age progression suggests slab rollback (Holm et al., 2007; Holm et al., 2005) following low-angle north-dipping subduction as the ca. 1700-1600 Mazatzal terrane approached. The anomaly we image disappears as it crosses the Yavapai-Mazatzal suture and enters a younger terrane with a different tectonic history. A map of tectonic provinces is shown in Figure 24.

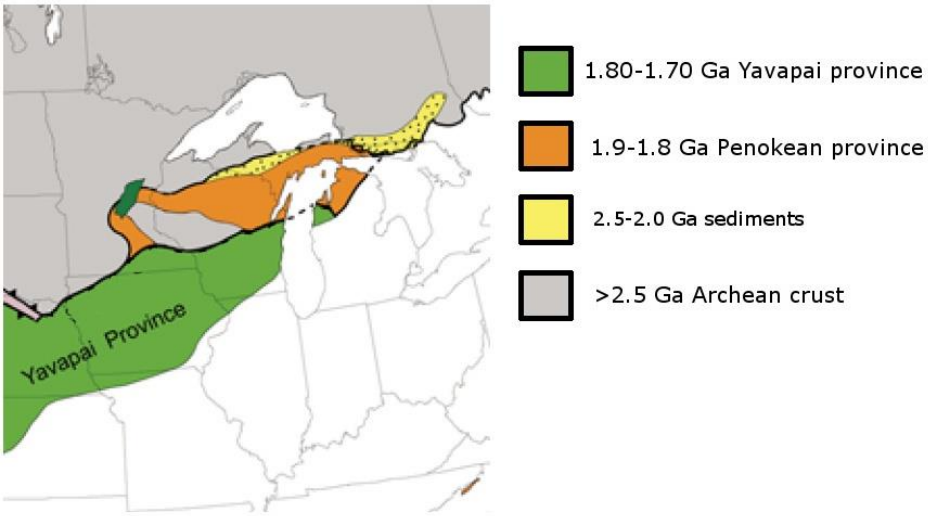

Figure 24. Map of tectonic provinces in the region of interest, with the boundary between Yavapai crust and older rock shown going across central Wisconsin, near the edge of our anomaly. Modified from Whitmeyer and Karlstrom, (2007).

Many authors have invoked low-angle subduction with slab rollback to explain deformation and magmatism migrating trenchward from far inland of the subduction

trench, including in the Trans-Mexican Volcanic Belt (Ferrari et al., 2012; Gérault et al., 2015), the western Mediterranean (Bezada et al., 2013; Malinverno & Ryan, 1986), the Laramide orogeny in western North America (Coney & Reynolds, 1977; Humphreys, 1995), the Acadian orogeny in northeastern North America (Murphy et al., 1999), and the South China fold belt (Li & Li, 2007). Similarly in the Yavapai orogeny, subduction-related deformation, heating, and magmatism occurred several hundred kilometers inland before migrating toward the trench, suggesting low-angle subduction (Holm et al., 2005), and crucially, with a timing that followed the ocean's transition to sulfur saturation. This allowed pyrite-rich subduction channel sediment to be conveyed inland below the Penokean province. The thermomechanical properties of subduction channel sediment were modeled analytically (Shreve & Cloos, 1986) and through finite element modeling (Ellis et al., 1999). Their models show that it is common for subducting sediment to undergo basal detachment from the downgoing slab, and to then underplate and become mechanically coupled to the overriding plate due to shearing and the contrast in density between sediment and slab. This would allow the sediment to remain at the base of Laurentian lithosphere after the slab falls away, where the pyrite-rich sediment awaited the Keweenawan mantle plume. A summary of our tectonic model is given in Figure 25.

4.5.4 Role of mantle plume

Dispersed pyrite grains, while abundant, are unlikely to produce a significant conductivity anomaly without a mechanism to enhance pyrite grain interconnectivity. Pyrite at this depth would begin to transition to pyrrhotite at 1250 °C and melt at 1550 °C (Bataleva et al., 2016; Sharp, 1969). At this temperature and at depths greater than 80 km, sulfide melting occurs before mafic silicic minerals begin to melt (Sharp, 1969), which would allow the sulfide liquid to interconnect around silicate mineral grains or recrystallize in feather-like dendritic structures that can traverse relatively large distances that reach across crystals of refractory minerals (Bataleva et al., 2016).

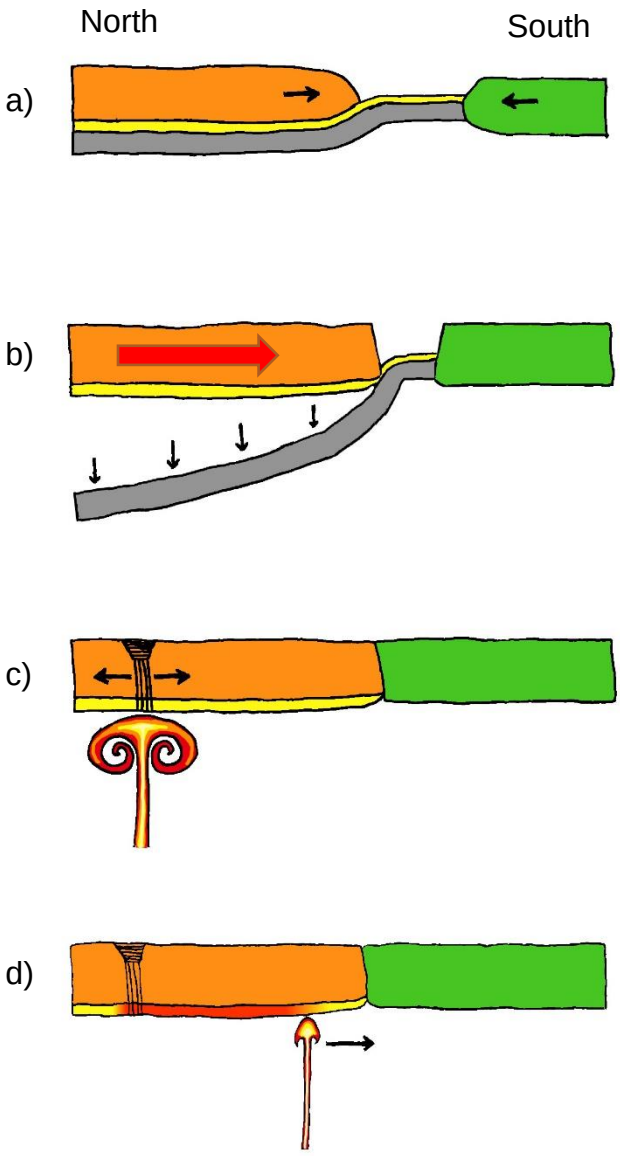

Figure 25. Our tectonic model is summarized in four stages: (a) Low-angle subduction of slab containing pyrite-rich sediment (yellow) emplaces the sediment at the base of the Laurentian lithosphere (orange). (b) Subduction angle steepens and the slab falls away, leaving underplated sediments behind as arc magmatism migrates south (red arrow). (c) The Keweenawan mantle plume head arrives, causing rifting and melting at the lithosphere-asthenosphere boundary. (d) The plume tail traverses the underside of the plate, melting the subducted sediment in its path to increase the interconnectivity of pyrite grains while leaving mafic minerals intact.

Furthermore, pure sulfur is released during the transition from pyrite to pyrrhotite around 1250 °C—which does not require mantle plume temperatures—creating small amounts of pure sulfur (Bataleva et al., 2016), which would be available for plume metals to react with and form a trail of metallic sulfides along the plume's path.

4.5.5 Broader implications: Olympic Dam

There is one other example of a linear conductive anomaly in the mantle beneath a Proterozoic continental back-arc setting that has been attributed to plume interaction. This has been observed in South Australia below the Gawler Craton in the Olympic Dam region (Thiel & Heinson, 2013), an area with many large massive sulfide deposits. Melting at Olympic Dam to produce a LIP has been inferred at the base of the lithosphere in a setting very similar to our region of interest (Swain et al., 2008). Previous researchers considered that the high conductivity is caused by veining of metallic sulfides upon interaction with the plume's high temperatures and iron enrichment. It is possible that the oceanographic and tectonic processes that produced the anomaly we observe in Laurentia are similar to those that occurred in Proterozoic Australia.

4.6 Conclusions

We used long-period magnetotellurics to create a resistivity model of the Great Lakes region of the United States that shows an elongated zone of anomalously high conductivity at a depth of 150 km south of Lake Superior. We interpret this anomaly track the track of the mantle plume that created the Keweenaw flood basalt province and initiated the 1.1 Ga Midcontinent Rift. After ruling out other sources of high conductivity, we determine that this anomaly is due to large amounts of metallic sulfide minerals in sediment that underwent low-angle north-dipping subduction during the ca. 1.8-1.7 Yavapai orogeny. Pyrite is an extremely conductive mineral that was abundant in the oceans following the ca 1.9-1.8 Ga transition from ferrous to sulfidic ocean chemistry, and marine sediment from shortly after this time would have been rich in pyrite. The region's tectonic history allows for this sediment to be transported to the

location and depth of the anomaly by low-angle subduction. When the mantle plume arrived, it melted the disseminated sulfides to increase their interconnectivity, greatly increasing the conductivity of the subducted sediment in the mantle plume's path. The anomaly's depth is consistent with geochemically-inferred flood basalt melting depths, its spatial extent is consistent with major geologic boundaries, its conductivity is consistent with metallic sulfides, and the region's pre- and syn-plume tectonics provided the ideal conditions to produce such an anomaly.

This study highlights the importance of considering the changes in fundamental Earth processes over a 2 billion year period since the earliest Laurentian accretions occurred. This period saw the arrival of oxygen in the atmosphere, which strongly changed the weathering of rocks, leading to sulfidic oceans. Banded-iron formations that previously were deposited as marine sediment in an iron-rich ocean gave way to pyrite-rich sediment. During Keweenawan volcanism, a hotter Proterozoic mantle allowed for much deeper melting than in any Phanerozoic LIP eruption. These events would not occur in modern conditions, leaving no trace of the Keweenawan hot spot track if it had interacted only with rocks produced in the present-day. Looking at the long-term changes in these major processes allows us to deconvolve all of the steps that produced an ancient conductivity anomaly.

Chapter 5: General conclusions

These three manuscripts show the effectiveness of the magnetotelluric method in determining the properties and internal structure of the Earth. These results show more than just the features in the models and their geologic interpretations, but also the importance of using MT in three-dimensions. The two modeling studies demonstrate how effective 3D MT is at resolving targets of arbitrary shape with no dimensionality assumptions to limit the geometry of the anomalies. Neither the Newberry study nor the midcontinent study shows features that are appropriate for 2D analysis, except on a very local scale. Using 2D MT, one is confined to small targets that are already assumed to be present, while unexpected targets will be overlooked or misinterpreted. 3D MT removes this limitation. Without 3D, one can miss the big picture and never realize it.

These studies also show models that require unconventional interpretations. Newberry Volcano, with its magma chamber shown clearly in seismic models, defies the conventional wisdom that magma is a conductive target. With seismic, petrological, and thermal constraints, we are able to use this apparent paradox to our advantage and use MT to narrow down the magma's chemical composition. In the Keweenaw mantle plume study, we analyze billion-year changes in global processes to find an interpretation that would not make sense in today's world, but fits the world of the past when the anomaly was created.

Bibliography

Achauer, U., Evans, J. R., & Stauber, D. A. (1988). High-resolution seismic tomography of compressional wave velocity structure at Newberry Volcano, Oregon Cascade Range. *Journal of Geophysical Research: Solid Earth*, *93*(B9), 10135–10147. https://doi.org/10.1029/JB093iB09p10135

Aizawa, K., Koyama, T., Hase, H., Uyeshima, M., Kanda, W., Utsugi, M., et al. (2014). Three-dimensional resistivity structure and magma plumbing system of the Kirishima Volcanoes as inferred from broadband magnetotelluric data. *Journal of Geophysical Research: Solid Earth*, *119*(1), 2013JB010682. https://doi.org/10.1002/2013JB010682

Archie, G. E. (1942). The electrical resistivity log as an aid in determining some reservoir characteristics: *Transactions of the American Institute of Mining, Metallurgical, and Petroleum Engineers*, *146*, 54–62.

Aster, R. C., Borchers, B., & Thurber, C. H. (2013). Chapter Six - Iterative Methods. In *Parameter Estimation and Inverse Problems* (2nd ed., pp. 141–168). Boston: Academic Press. https://doi.org/10.1016/B978-0-12-385048-5.00006-9

Avdeev, D. B. (2005). Three-Dimensional Electromagnetic Modelling and Inversion from Theory to Application. *Surveys in Geophysics*, *26*(6), 767–799. https://doi.org/10.1007/s10712-005-1836-x

Bahr, K. (1988). Interpretation of the magnetotelluric impedance tensor: regional induction and local telluric distortion. *J. Geophys*, *62*(2), 119–127.

Bargar, K. E., & Keith, T. E. C. (1999). *Hydrothermal Mineralogy of Core from Geothermal Drill Holes at Newberry Volcano, Oregon* (U.S. Geological Survey Professional Paper No. 1578). Washington, D. C.: U.S. Geological Survey. Retrieved from https://pubs.usgs.gov/pp/pp1578/

Bataleva, Y. V., Palyanov, Y. N., Borzdov, Y. M., & Sobolev, N. V. (2016). Sulfidation of silicate mantle by reduced S-bearing metasomatic fluids and melts. *Geology*, *44*(4), 271–274. https://doi.org/10.1130/G37477.1

Beachly, M. W., Hooft, E. E., Toomey, D. R., & Waite, G. P. (2012). Upper crustal structure of Newberry Volcano from P-wave tomography and finite difference waveform modeling. *Journal of Geophysical Research: Solid Earth*, *117*(B10). https://doi.org/10.1029/2012JB009458

Beblo, M., & Liebig, V. (1990). Magnetotelluric measurements in Antarctica. *Physics of the Earth and Planetary Interiors*, *60*(1), 89–99. https://doi.org/10.1016/0031-9201(90)90251-R

Bedrosian, P. A. (2016). Making it and breaking it in the Midwest: Continental assembly and rifting from modeling of EarthScope magnetotelluric data. *Precambrian Research*, *278*, 337–361. https://doi.org/10.1016/j.precamres.2016.03.009

Bedrosian, P. A., Peacock, J. R., Bowles-Martinez, E., Schultz, A., & Hill, G. J. (2018). Crustal inheritance and a top-down control on arc magmatism at Mount St Helens. *Nature Geoscience*. https://doi.org/10.1038/s41561-018-0217-2

Behrendt, J. C., Hutchinson, D. R., Lee, M., Thornber, C. R., Trehu, A., Cannon, W., & Green, A. (1990). GLIMPCE seismic reflection evidence of deep-crustal and upper-mantle intrusions and magmatic underplating associated with the Midcontinent Rift system of North America. *Tectonophysics*, *173*(1–4), 595–615.

Berdichevsky, M. N., Dmitriev, V. I., & Pozdnjakova, E. E. (1998). On two-dimensional interpretation of magnetotelluric soundings. *Geophysical Journal International*, *133*(3), 585–606. https://doi.org/10.1046/j.1365-246X.1998.01333.x

Bernard, J., Vachette, C., & Valla, P. (1990). Deep groundwater survey with audio?magnetotelluric soundings. In *SEG Technical Program Expanded Abstracts 1990* (Vols. 1–0, pp. 528–531). Society of Exploration Geophysicists. https://doi.org/10.1190/1.1890253

Bezada, M. J., Humphreys, E. D., Toomey, D. R., Harnafi, M., Dávila, J. M., & Gallart, J. (2013). Evidence for slab rollback in westernmost Mediterranean from improved upper mantle imaging. *Earth and Planetary Science Letters*, *368*, 51–60. https://doi.org/10.1016/j.epsl.2013.02.024

Blackwell, D., Richards, M., Frone, Z., Batir, J., Ruzo, A., Dingwall, R., & Williams, M. (2011). Temperature at depth maps for the conterminous US and geothermal resource estimates. *Geothermal Resources Council Transactions*, *35*.

Blackwell, D. D. (1994). *A summary of deep thermal data from the Cascade range and analysis of the "rain curtain" effect* (Open File Report No. O-94-07) (p. 131). Portland: State of Oregon Department of Geology and Mineral Industries.

Bonner, L. R., & Schultz, A. (2017). Rapid prediction of electric fields associated with geomagnetically induced currents in the presence of three-dimensional ground structure: Projection of remote magnetic observatory data through magnetotelluric impedance tensors. *Space Weather*, *15*(1), 204–227. https://doi.org/10.1002/2016SW001535

Bonneville, A., Cladouhos, T. T., & Schultz, A. (2016). Establishing the Frontier Observatory for Research in Geothermal Energy (FORGE) on the Newberry Volcano, Oregon. In *Proceedings* (Vol. 41, p. 9). Palo Alto.

Booker, J. R. (2014). The Magnetotelluric Phase Tensor: A Critical Review. *Surveys in Geophysics*, *35*(1), 7–40. https://doi.org/10.1007/s10712-013-9234-2

Boteler, D. H. (2001). Space Weather Effects on Power Systems. In P. Song, H. J. Singer, & G. L. Siscoe (Eds.), *Space Weather* (pp. 347–352). Washington, D. C.: American Geophysical Union. https://doi.org/10.1029/GM125p0347

Boteler, D. H. (2006). The super storms of August/September 1859 and their effects on the telegraph system. *Advances in Space Research*, *38*(2), 159–172. https://doi.org/10.1016/j.asr.2006.01.013

Cagniard, L. (1953). Basic theory of the magneto-telluric method of geophysical prospecting. *GEOPHYSICS*, *18*(3), 605–635. https://doi.org/10.1190/1.1437915

Caldwell, T. G., Bibby, H. M., & Brown, C. (2004). The magnetotelluric phase tensor. *Geophysical Journal International*, *158*(2), 457–469. https://doi.org/10.1111/j.1365-246X.2004.02281.x

Camp, V. E., & Ross, M. E. (2004). Mantle dynamics and genesis of mafic magmatism in the intermontane Pacific Northwest. *Journal of Geophysical Research: Solid Earth*, *109*(B8), B08204. https://doi.org/10.1029/2003JB002838

Campbell, I. H., & Griffiths, R. W. (1990). Implications of mantle plume structure for the evolution of flood basalts. *Earth and Planetary Science Letters*, *99*(1), 79–93. https://doi.org/10.1016/0012-821X(90)90072-6

Canfield, D. E. (1998). A new model for Proterozoic ocean chemistry. *Nature*, *396*(6710), 450–453.

Canfield, Donald E., & Farquhar, J. (2009). Animal evolution, bioturbation, and the sulfate concentration of the oceans. *Proceedings of the National Academy of Sciences*, *106*(20), 8123–8127. https://doi.org/10.1073/pnas.0902037106

Canfield, Donald E., & Raiswell, R. (1999). The evolution of the sulfur cycle. *American Journal of Science*, *299*(7–9), 697–723.

Canfield, Donald E., Poulton, S. W., & Narbonne, G. M. (2007). Late-Neoproterozoic Deep-Ocean Oxygenation and the Rise of Animal Life. *Science*, *315*(5808), 92–95. https://doi.org/10.1126/science.1135013

Cannon, W. F. (1992). The Midcontinent rift in the Lake Superior region with emphasis on its geodynamic evolution. *Tectonophysics*, *213*(1–2), 41–48.

Cannon, W. F. (1994). Closing of the Midcontinent rift-A far—field effect of Grenvillian compression. *Geology*, *22*(2), 155–158.

Cannon, W. F., Green, A. G., Hutchinson, D. R., Lee, M., Milkereit, B., Behrendt, J. C., et al. (1989). The North American Midcontinent rift beneath Lake Superior from GLIMPCE seismic reflection profiling. *Tectonics*, *8*(2), 305–332.

Carlson, R. W., L., G. T., & Julie M., D. (2018). Origin of Primitive Tholeiitic and Calc-Alkaline Basalts at Newberry Volcano, Oregon. *Geochemistry, Geophysics, Geosystems*, *0*(0). https://doi.org/10.1029/2018GC007454

Carrington, R. C. (1859). Description of a Singular Appearance seen in the Sun on September 1, 1859. *Monthly Notices of the Royal Astronomical Society*, *20*(1), 13–15. https://doi.org/10.1093/mnras/20.1.13

Chandler, V. W. (1983). Correlation of magnetic anomalies in east-central Minnesota and northwestern Wisconsin: Constraints on magnitude and direction of Keweenawan rifting. *Geology*, *11*(3), 174–176. https://doi.org/10.1130/0091-7613(1983)11<174:COMAIE>2.0.CO;2

Chandler, V. W. (1990). Geologic interpretation of gravity and magnetic data over the central part of the Duluth Complex, northeastern Minnesota. *Economic Geology*, *85*(4), 816–829.

Chant, I. J., & Hastie, L. M. (1992). Time-frequency analysis of magnetotelluric data. *Geophysical Journal International*, *111*(2), 399–413. https://doi.org/10.1111/j.1365-246X.1992.tb00586.x

Chave, A., & Jones, A. (2012). *The Magnetotelluric Method, Theory and Practice* (1st ed.). New York: Cambridge University Press. https://doi.org/10.1017/CBO9781139020138

Chave, A. D., & Thomson, D. J. (1989). Some comments on magnetotelluric response function estimation. *Journal of Geophysical Research: Solid Earth*, *94*(B10), 14215–14225. https://doi.org/10.1029/JB094iB10p14215

Coney, P. J., & Reynolds, S. J. (1977). Cordilleran Benioff zones. *Nature*, *270*(5636), 403–406. https://doi.org/10.1038/270403a0

Constable, S., Shankland, T. J., & Duba, A. (1992). The electrical conductivity of an isotropic olivine mantle. *Journal of Geophysical Research: Solid Earth*, *97*(B3), 3397–3404. https://doi.org/10.1029/91JB02453

Davis, D. W., & Green, J. C. (1997). Geochronology of the North American Midcontinent rift in western Lake Superior and implications for its geodynamic evolution. *Canadian Journal of Earth Sciences*, *34*(4), 476–488. https://doi.org/10.1139/e17-039

Dickas, A. B. (1986). Comparative Precambrian Stratigraphy and Structure Along the Mid-Continent Rift. *AAPG Bulletin*, *70*(3), 225–238.

Ding, X., Li, C., Ripley, E. M., Rossell, D., & Kamo, S. (2010). The Eagle and East Eagle sulfide ore-bearing mafic-ultramafic intrusions in the Midcontinent Rift System, upper Michigan: Geochronology and petrologic evolution. *Geochemistry, Geophysics, Geosystems*, *11*(3). https://doi.org/10.1029/2009GC002546

Ding, X., Ripley, E. M., & Li, C. (2012). PGE geochemistry of the Eagle Ni–Cu–(PGE) deposit, Upper Michigan: constraints on ore genesis in a dynamic magma conduit. *Mineralium Deposita*, *47*(1–2), 89–104. https://doi.org/10.1007/s00126-011-0350-y

Dong, S.-W., Li, T.-D., Lü, Q.-T., Gao, R., Yang, J.-S., Chen, X.-H., et al. (2013). Progress in deep lithospheric exploration of the continental China: A review of the SinoProbe. *Tectonophysics*, *606*, 1–13. https://doi.org/10.1016/j.tecto.2013.05.038

Donnelly-Nolan, J. M., Champion, D. E., Lanphere, M. A., & Ramsey, D. W. (2004). New Thoughts About Newberry Volcano, Central Oregon USA. *AGU Fall Meeting Abstracts*, *43*, V43E-1452.

Duncan, R. A. (1990). The volcanic record of the Reunion hotspot. *Proceedings of the Ocean Drilling Program, Scientific Results*, *115*, 10.

Egbert, G. D. (1997). Robust multiple-station magnetotelluric data processing. *Geophysical Journal International*, *130*(2), 475–496. https://doi.org/10.1111/j.1365-246X.1997.tb05663.x

Egbert, G. D., & Booker, J. R. (1986). Robust estimation of geomagnetic transfer functions. *Geophysical Journal of the Royal Astronomical Society*, *87*(1), 173–194. https://doi.org/10.1111/j.1365-246X.1986.tb04552.x

Egbert, G. D., & Kelbert, A. (2012). Computational recipes for electromagnetic inverse problems. *Geophysical Journal International*, *189*(1), 251–267. https://doi.org/10.1111/j.1365-246X.2011.05347.x

Egbert, G. D., & Livelybrooks, D. (1996). Single station magnetotelluric impedance estimation: Coherence weighting and the regression M-estimate. *GEOPHYSICS*, *61*(4), 964–970. https://doi.org/10.1190/1.1444045

Egbert, G. D., Eisel, M., Boyd, O. S., & Morrison, H. F. (2000). DC trains and Pc3s: Source effects in mid-latitude geomagnetic transfer functions. *Geophysical Research Letters*, *27*(1), 25–28. https://doi.org/10.1029/1999GL008369

Eichelberger, J. C., Carrigan, C. R., Westrich, H. R., & Price, R. H. (1986). Non-explosive silicic volcanism. *Nature*, *323*(6089), 598. https://doi.org/10.1038/323598a0

Ellis, S., Beaumont, C., & Pfiffner, O. A. (1999). Geodynamic models of crustal-scale episodic tectonic accretion and underplating in subduction zones. *Journal of Geophysical Research: Solid Earth*, *104*(B7), 15169–15190. https://doi.org/10.1029/1999JB900071

Evans, R. L. (1994). Constraints On the Large-Scale Porosity and Permeability Structure of Young Oceanic Crust From Velocity and Resistivity Data. *Geophysical Journal International*, *119*(3), 869–879. https://doi.org/10.1111/j.1365-246X.1994.tb04023.x

Evans, R. L. (2012). Earth's Electromagnetic Environment: 3A. Conductivity of Earth Materials. In *The Magnetotelluric Method: Theory and Practice* (p. 552). New York: Cambridge University Press.

Farquhar, J., Wu, N., Canfield, D. E., & Oduro, H. (2010). Connections between sulfur cycle evolution, sulfur isotopes, sediments, and base metal sulfide deposits. *Economic Geology*, *105*(3), 509–533.

Ferrari, L., Orozco-Esquivel, T., Manea, V., & Manea, M. (2012). The dynamic history of the Trans-Mexican Volcanic Belt and the Mexico subduction zone. *Tectonophysics*, *522–523*, 122–149. https://doi.org/10.1016/j.tecto.2011.09.018

Fitterman, D. V. (1988a). Overview of the structure and geothermal potential of Newberry Volcano, Oregon. *Journal of Geophysical Research: Solid Earth*, *93*(B9), 10059–10066. https://doi.org/10.1029/JB093iB09p10059

Fitterman, D. V. (1988b). Overview of the structure and geothermal potential of Newberry Volcano, Oregon. *Journal of Geophysical Research: Solid Earth*, *93*(B9), 10059–10066. https://doi.org/10.1029/JB093iB09p10059

Fitterman, D. V., Stanley, W. D., & Bisdorf, R. J. (1988). Electrical structure of Newberry volcano, Oregon. *Journal of Geophysical Research: Solid Earth*, *93*(B9), 10119–10134.

Foster, J., Gjelde, E., Graham, W. R., Hermann, R. J., Kluepfel, H. M., Lawson, R. L., et al. (2004). *Report of the Commission to Assess the Threat to the United States from Electromagnetic Pulse (EMP) Attack. Volume 1: Executive Report*. National Research Council Washington DC, Committee on Electromagnetic Pulse Environment. Retrieved from http://www.dtic.mil/docs/citations/ADA484497

Foster, J., Gjelde, E., Graham, W. R., Hermann, R. J., Kluepfel, H. M., Lawson, R. L., et al. (2008). *Report of the Commission to Assess the Threat to the United States from Electromagnetic Pulse (EMP) Attack: Critical National Infrastructures*. Electromagnetic Pulse Commission, McLean, Virginia. Retrieved from http://www.dtic.mil/docs/citations/ADA484672

Franklin, J. M., McIlwaine, W. H., Poulsen, K. H., & Wanless, R. K. (1980). Stratigraphy and depositional setting of the Sibley Group, Thunder Bay district, Ontario, Canada. *Canadian Journal of Earth Sciences*, *17*(5), 633–651. https://doi.org/10.1139/e80-060

Frone, Z. S. (2015). *Heat flow, thermal modeling and whole rock geochemistry of Newberry Volcano, Oregon and heat flow modeling of the Appalachian Basin, West Virginia* (Dissertation). Southern Methodist University, Dallas. Retrieved from https://search.proquest.com/openview/4c7c19f03878c6c54c33f32aefc909d1

Fullea, J., Muller, M. R., & Jones, A. G. (2011). Electrical conductivity of continental lithospheric mantle from integrated geophysical and petrological modeling: Application to the Kaapvaal Craton and Rehoboth Terrane, southern Africa. *Journal of Geophysical Research*, *116*(B10). https://doi.org/10.1029/2011JB008544

Gaillard, F. (2004). Laboratory measurements of electrical conductivity of hydrous and dry silicic melts under pressure. *Earth and Planetary Science Letters*, *218*(1), 215–228. https://doi.org/10.1016/S0012-821X(03)00639-3

Gamble, T., Goubau, W., & Clarke, J. (1979). Magnetotellurics with a remote magnetic reference. *GEOPHYSICS*, *44*(1), 53–68. https://doi.org/10.1190/1.1440923

Gérault, M., Husson, L., Miller, M. S., & Humphreys, E. D. (2015). Flat-slab subduction, topography, and mantle dynamics in southwestern Mexico. *Tectonics*, *34*(9), 1892–1909. https://doi.org/10.1002/2015TC003908

Glover, P. (2009). What is the cementation exponent? A new interpretation. *The Leading Edge*, *28*(1), 82–85. https://doi.org/10.1190/1.3064150

Grasso, K. A., Meigs, A., & Cladouhos, T. T. (2012, April 20). *Origin of faults, fissures and volcanic vent alignments at a structural triple junction, Newberry Volcano, central Oregon* (Undergraduate thesis). Oregon State University, Corvallis.

Griffiths, R. W., & Campbell, I. H. (1990). Stirring and structure in mantle starting plumes. *Earth and Planetary Science Letters*, *99*(1–2), 66–78.

Groom, R. W., & Bailey, R. C. (1989). Decomposition of Magnetotelluric Impedance Tensors in the Presence of Local Three-Dimensional Galvanic Distortion. *Journal of Geophysical Research*, *94*(B2), 1913–1925.

ten Grotenhuis, S. M., Drury, M. R., Spiers, C. J., & Peach, C. J. (2005). Melt distribution in olivine rocks based on electrical conductivity measurements. *Journal of Geophysical Research: Solid Earth*, *110*(B12). https://doi.org/10.1029/2004JB003462

Guo, X., Zhang, L., Behrens, H., & Ni, H. (2016). Probing the status of felsic magma reservoirs: Constraints from the P–T–H2O dependences of electrical conductivity of rhyolitic melt. *Earth and Planetary Science Letters*, *433*, 54–62. https://doi.org/10.1016/j.epsl.2015.10.036

Heath, Benjamin A., Hooft, Emilie E. E., Toomey, Douglas R., & Bezada, Maximiliano J. (2015). Imaging the magmatic system of Newberry Volcano using joint active source and teleseismic tomography. *Geochemistry, Geophysics, Geosystems*, *16*(12), 4433–4448. https://doi.org/10.1002/2015GC006129

Hibbs, A., Petrov, T., Pendleton, J., Milberger, S., Eiskamp, G., & Wilson, G. (2012). New electromagnetic sensors for magnetotelluric and induced polarization geophysical surveys. In *SEG Technical Program Expanded Abstracts 2012* (Vols. 1–0, pp. 1–5). Society of Exploration Geophysicists. https://doi.org/10.1190/segam2012-1478.1

Higgins, M. W. (1973). Petrology of Newberry volcano, central Oregon. *Geological Society of America Bulletin*, *84*(2), 455–488.

Hildreth, W. (2007). *Quaternary Magmatism in the Cascades--Geologic Perspectives* (Professional Paper No. 1744) (p. 125). United States Geological Survey. Retrieved from https://pubs.usgs.gov/pp/pp1744/

Hollings, P., Richardson, A., Creaser, R. A., & Franklin, J. M. (2007). Radiogenic isotope characteristics of the Mesoproterozoic intrusive rocks of the Nipigon Embayment, northwestern Ontario. *Canadian Journal of Earth Sciences*, *44*(8), 1111–1129. https://doi.org/10.1139/e06-128

Hollings, P., Smyk, M., & Cousens, B. (2012). The radiogenic isotope characteristics of dikes and sills associated with the Mesoproterozoic Midcontinent Rift near Thunder Bay, Ontario, Canada. *Precambrian Research*, *214–215*, 269–279. https://doi.org/10.1016/j.precamres.2011.11.006

Holm, D. K., Van Schmus, W. R., MacNeill, L. C., Boerboom, T. J., Schweitzer, D., & Schneider, D. (2005). U-Pb zircon geochronology of Paleoproterozoic plutons from the northern midcontinent, USA: Evidence for subduction flip and continued convergence after geon 18 Penokean orogenesis. *Geological Society of America Bulletin*, *117*(3–4), 259–275.

Holm, D. K., Schneider, D. A., Rose, S., Mancuso, C., McKenzie, M., Foland, K. A., & Hodges, K. V. (2007). Proterozoic metamorphism and cooling in the southern Lake Superior region, North America and its bearing on crustal evolution. *Precambrian Research*, *157*(1), 106–126. https://doi.org/10.1016/j.precamres.2007.02.012

Holtz, F., Johannes, W., Tamic, N., & Behrens, H. (2001). Maximum and minimum water contents of granitic melts generated in the crust: a reevaluation and implications. *Lithos*, *56*(1), 1–14. https://doi.org/10.1016/S0024-4937(00)00056-6

Hooper, P. R. (1990). The timing of crustal extension and the eruption of continental flood basalts. *Nature*, *345*(6272), 246. https://doi.org/10.1038/345246a0

Houseman, G., & England, P. (1986). A dynamical model of lithosphere extension and sedimentary basin formation. *Journal of Geophysical Research: Solid Earth*, *91*(B1), 719–729. https://doi.org/10.1029/JB091iB01p00719

Humphreys, E. D. (1995). Post-Laramide removal of the Farallon slab, western United States. *Geology*, *23*(11), 987–990. https://doi.org/10.1130/0091-7613(1995)023<0987:PLROTF>2.3.CO;2

Hutchinson, D. R., White, R. S., Cannon, W. F., & Schulz, K. J. (1990). Keweenaw hot spot: Geophysical evidence for a 1.1 Ga mantle plume beneath the Midcontinent Rift System. *Journal of Geophysical Research: Solid Earth*, *95*(B7), 10869–10884.

Ingham, M. R., Bibby, H. M., Heise, W., Jones, K. A., Cairns, P., Dravitzki, S., et al. (2009). A magnetotelluric study of Mount Ruapehu volcano, New Zealand. *Geophysical Journal International*, *179*(2), 887–904. https://doi.org/10.1111/j.1365-246X.2009.04317.x

IRIS DMC. (2018). Data Services Products: iMUSH.MT.Bedrosian2018.resistivity, three-dimensional electrical resistivity model for southwest Washington. https://doi.org/10.17611/DP/EMCIMUSHMT18

Jackson, P., Smith, D., & Stanford, P. (1978). Resistivity-porosity-particle shape relationships for marine sands. *GEOPHYSICS*, *43*(6), 1250–1268. https://doi.org/10.1190/1.1440891

Jay, A. E., & Widdowson, M. (2008). Stratigraphy, structure and volcanology of the SE Deccan continental flood basalt province: implications for eruptive extent and volumes. *Journal of the Geological Society*, *165*(1), 177–188. https://doi.org/10.1144/0016-76492006-062

Jiracek, G. R. (1990). Near-surface and topographic distortions in electromagnetic induction. *Surveys in Geophysics*, *11*(2–3), 163–203. https://doi.org/10.1007/BF01901659

Jones, A. G., Chave, A. D., Egbert, G. D., Auld, D., & Bahr, K. (1989). A comparison of techniques for magnetotelluric response function estimation. *Journal of Geophysical Research: Solid Earth*, *94*(B10), 14201–14213. https://doi.org/10.1029/JB094iB10p14201

Kagiyama, T., Utada, H., & Yamamoto, T. (1999). Magma ascent beneath Unzen Volcano, SW Japan, deduced from the electrical resistivity structure. *Journal of Volcanology and Geothermal Research*, *89*(1), 35–42. https://doi.org/10.1016/S0377-0273(98)00120-6

Kappler, K. N., Morrison, H. F., & Egbert, G. D. (2010). Long-term monitoring of ULF electromagnetic fields at Parkfield, California. *Journal of Geophysical Research: Solid Earth*, *115*(B4), B04406. https://doi.org/10.1029/2009JB006421

Keays, R. R., & Lightfoot, P. C. (2015). Geochemical stratigraphy of the Keweenawan Midcontinent Rift volcanic rocks with regional implications for the genesis of associated Ni, Cu, Co, and platinum group element sulfide mineralization. *Economic Geology*, *110*(5), 1235–1267.

Keith, T. E. C., & Bargar, K. E. (1988). Petrology and hydrothermal mineralogy of U.S. geological survey Newberry: 2. Drill core from Newberry Caldera, Oregon. *Journal of Geophysical Research: Solid Earth*, *93*(B9), 10174–10190. https://doi.org/10.1029/JB093iB09p10174

Kelbert, A., Egbert, G. D., & Schultz, A. (2011). IRIS DMC Data Services Products: EMTF, The Magnetotelluric Transfer Functions. *Incorporated Research Institutions for Seismology*. https://doi.org/10.17611/DP/EMTF.1

Kelbert, A., Meqbel, N., Egbert, G. D., & Tandon, K. (2014). ModEM: A modular system for inversion of electromagnetic geophysical data. *Computers & Geosciences*, *66*, 40–53. https://doi.org/10.1016/j.cageo.2014.01.010

King, E. R., & Zietz, I. (1971). Aeromagnetic Study of the Midcontinent Gravity High of Central United States. *Geological Society of America Bulletin*, *82*(8), 2187–2208. https://doi.org/10.1130/0016-7606(1971)82[2187:ASOTMG]2.0.CO;2

Komori, S., Utsugi, M., Kagiyama, T., Inoue, H., Chen, C.-H., Chiang, H.-T., et al. (2014). Hydrothermal system in the Tatun Volcano Group, northern Taiwan, inferred from crustal resistivity structure by audio-magnetotellurics. *Progress in Earth and Planetary Science*, *1*(1), 20. https://doi.org/10.1186/s40645-014-0020-7

Kuehn, S. C., & Foit, F. F. (2006). Correlation of widespread Holocene and Pleistocene tephra layers from Newberry Volcano, Oregon, USA, using glass compositions and numerical analysis. *Quaternary International*, *148*(1), 113–137. https://doi.org/10.1016/j.quaint.2005.11.008

Labrosse, S., & Jaupart, C. (2007). Thermal evolution of the Earth: Secular changes and fluctuations of plate characteristics. *Earth and Planetary Science Letters*, *260*(3–4), 465–481. https://doi.org/10.1016/j.epsl.2007.05.046

Laidley, R. A., & McKay, D. S. (1971). Geochemical examination of obsidians from Newberry Caldera, Oregon. *Contributions to Mineralogy and Petrology*, *30*(4), 336–342. https://doi.org/10.1007/BF00404728

Laumonier, M., Gaillard, F., & Sifre, D. (2014). The effect of pressure and water concentration on the electrical conductivity of dacitic melts: Implication for magnetotelluric imaging in subduction areas. *Chemical Geology*, *418*, 66–76. https://doi.org/10.1016/j.chemgeo.2014.09.019

Ledo, J., Queralt, P., & Pous, J. (1998). Effects of galvanic distortion on magnetotelluric data over a three-dimensional regional structure. *Geophysical Journal International*, *132*(2), 295–301. https://doi.org/10.1046/j.1365-246x.1998.00417.x

Li, Z.-X., & Li, X.-H. (2007). Formation of the 1300-km-wide intracontinental orogen and postorogenic magmatic province in Mesozoic South China: A flat-slab subduction model. *Geology*, *35*(2), 179–182. https://doi.org/10.1130/G23193A.1

Logan, G. A., Hayes, J. M., Hieshima, G. B., & Summons, R. E. (1995). Terminal Proterozoic reorganization of biogeochemical cycles. *Nature*, *376*(6535), 53–56.

Love, J. J., Pulkkinen, A., Bedrosian, P. A., Jonas, S., Kelbert, A., Rigler, E. J., et al. (2016). Geoelectric hazard maps for the continental United States. *Geophysical Research Letters*, *43*(18), 9415–9424. https://doi.org/10.1002/2016GL070469

Love, J. J., Lucas, G. M., Kelbert, A., & Bedrosian, P. A. (2018). Geoelectric Hazard Maps for the Mid-Atlantic United States: 100 Year Extreme Values and the 1989 Magnetic Storm. *Geophysical Research Letters*, *45*(1), 5–14. https://doi.org/10.1002/2017GL076042

Lucas, G. M., Love, J. J., & Kelbert, A. (2018). Calculation of Voltages in Electric Power Transmission Lines During Historic Geomagnetic Storms: An Investigation Using Realistic Earth Impedances. *Space Weather*, *16*(2), 185–195. https://doi.org/10.1002/2017SW001779

Mackie, R. L., Smith, J. T., & Madden, T. R. (1994). Three-dimensional electromagnetic modeling using finite difference equations: The magnetotelluric example. *Radio Science*, *29*(4), 923–935. https://doi.org/10.1029/94RS00326

MacLeod, N. S., & Sherrod, D. R. (1988). Geologic evidence for a magma chamber beneath Newberry Volcano, Oregon. *Journal of Geophysical Research: Solid Earth*, *93*(B9), 10067–10079. https://doi.org/10.1029/JB093iB09p10067

MacLeod, N. S., Sherrod, D. R., Chitwood, L. A., & Jensen, R. A. (1995). Geologic map of Newberry Volcano, Deschutes, Klamath, and Lake Counties, Oregon. U.S. Geological Survey.

Malinverno, A., & Ryan, W. B. F. (1986). Extension in the Tyrrhenian Sea and shortening in the Apennines as result of arc migration driven by sinking of the lithosphere. *Tectonics*, *5*(2), 227–245. https://doi.org/10.1029/TC005i002p00227

Mandler, B. E., Donnelly-Nolan, J. M., & Grove, T. L. (2014). Straddling the tholeiitic/calc-alkaline transition: the effects of modest amounts of water on magmatic differentiation at Newberry Volcano, Oregon. *Contributions to Mineralogy and Petrology*, *168*(4), 1066. https://doi.org/10.1007/s00410-014-1066-7

Mareschal, J.-C. (1983). Mechanisms of uplift preceding rifting. *Tectonophysics*, *94*(1), 51–66. https://doi.org/10.1016/0040-1951(83)90009-4

McGary, R. S., Evans, R. L., Wannamaker, P. E., Elsenbeck, J., & Rondenay, S. (2014). Pathway from subducting slab to surface for melt and fluids beneath Mount Rainier. *Nature*, *511*(7509), 338–340. https://doi.org/10.1038/nature13493

McKay, D., Donnelly-Nolan, J. M., Jensen, R. A., & Champion, D. E. (2009). The post-Mazama northwest rift zone eruption at Newberry Volcano, Oregon. Retrieved from https://pubs.er.usgs.gov/publication/70157123

McKenzie, D., & Bickle, M. J. (1988). The volume and composition of melt generated by extension of the lithosphere. *Journal of Petrology*, *29*(3), 625–679.

Mendelson, K., & Cohen, M. (1982). The effect of grain anisotropy on the electrical properties of sedimentary rocks. *GEOPHYSICS*, *47*(2), 257–263. https://doi.org/10.1190/1.1441332

Meqbel, N., Egbert, G. D., Wannamaker, P. E., Kelbert, A., & Schultz, A. (2014). Deep electrical resistivity structure of the northwestern U.S. derived from 3-D inversion of USArray magnetotelluric data. *Earth and Planetary Science Letters*, *402*, 290–304. https://doi.org/10.1016/j.epsl.2013.12.026

Merino, M., Keller, G. R., Stein, S., & Stein, C. (2013). Variations in Mid-Continent Rift magma volumes consistent with microplate evolution. *Geophysical Research Letters*, *40*(8), 1513–1516. https://doi.org/10.1002/grl.50295

Milsch, H., Kristinsdóttir, L. H., Spangenberg, E., Bruhn, D., & Flóvenz, Ó. G. (2010). Effect of the water–steam phase transition on the electrical conductivity of porous rocks. *Geothermics*, *39*(1), 106–114. https://doi.org/10.1016/j.geothermics.2009.09.001

Mittet, R. (2015). Seismic wave propagation concepts applied to the interpretation of marine controlled-source electromagneticsSeismic wave propagation and marine CSEM. *Geophysics*, *80*(2), E63–E81. https://doi.org/10.1190/geo2014-0215.1

Morgan, W. J. (1971). Convection Plumes in the Lower Mantle. *Nature*, *230*(5288), 42. https://doi.org/10.1038/230042a0

Murphy, J. B., Staal, C. R. van, & Keppie, J. D. (1999). Middle to late Paleozoic Acadian orogeny in the northern Appalachians: A Laramide-style plume-modified orogeny? *Geology*, *27*(7), 653–656. https://doi.org/10.1130/0091-7613(1999)027<0653:MTLPAO>2.3.CO;2

NEWGEN Consortium. (2016, May 23). Pacific Northwest National Laboratory Phase 1 Report, a collection of 14 reports submitted for DOE FORGE application. Retrieved January 23, 2019, from https://www.energy.gov/eere/forge/downloads/pacific-northwest-national-laboratory-phase-1-report

Newman, G. A., Gasperikova, E., Hoversten, G. M., & Wannamaker, P. E. (2008). Three-dimensional magnetotelluric characterization of the Coso geothermal field. *Geothermics*, *37*(4), 369–399. https://doi.org/10.1016/j.geothermics.2008.02.006

Nichols, E., Morrison, H., & Lee, S. (1994). Controlled source magnetotellurics for groundwater. In *SEG Technical Program Expanded Abstracts 1994* (pp. 553–554). Society of Exploration Geophysicists. https://doi.org/10.1190/1.1932156

Nicholson, S. W., & Shirey, S. B. (1990). Midcontinent rift volcanism in the Lake Superior region: Sr, Nd, and Pb isotopic evidence for a mantle plume origin. *Journal of Geophysical Research: Solid Earth*, *95*(B7), 10851–10868.

Paces, J. B., & Miller, J. D. (1993). Precise U-Pb ages of Duluth Complex and related mafic intrusions, northeastern Minnesota: Geochronological insights to physical, petrogenetic, paleomagnetic, and tectonomagmatic processes associated with the 1.1 Ga Midcontinent Rift System. *Journal of Geophysical Research: Solid Earth*, *98*(B8), 13997–14013. https://doi.org/10.1029/93JB01159

Parkinson, W. D. (1962). The Influence of Continents and Oceans on Geomagnetic Variations. *Geophysical Journal of the Royal Astronomical Society*, *6*(4), 441–449. https://doi.org/10.1111/j.1365-246X.1962.tb02992.x

Patro, P. K., Uyeshima, M., & Siripunvaraporn, W. (2013). Three-dimensional inversion of magnetotelluric phase tensor data. *Geophysical Journal International*, *192*(1), 58–66. https://doi.org/10.1093/gji/ggs014

Peacock, J. R., & Selway, K. (2016). Magnetotelluric investigation of the Vestfold Hills and Rauer Group, East Antarctica. *Journal of Geophysical Research: Solid Earth*, *121*(4), 2258–2273. https://doi.org/10.1002/2015JB012677

Peacock, J. R., Thiel, S., Reid, P., & Heinson, G. (2012). Magnetotelluric monitoring of a fluid injection: Example from an enhanced geothermal system. *Geophysical Research Letters*, *39*(18), L18403. https://doi.org/10.1029/2012GL053080

Peacock, J. R., Mangan, M. T., McPhee, D., & Wannamaker, P. E. (2016). Three-dimensional electrical resistivity model of the hydrothermal system in Long Valley Caldera, California, from magnetotellurics. *Geophysical Research Letters*, *43*(15), 2016GL069263. https://doi.org/10.1002/2016GL069263

Perry, H. K. C. (2004). Heat flow in the Nipigon arm of the Keweenawan rift, northwestern Ontario, Canada. *Geophysical Research Letters*, *31*(15). https://doi.org/10.1029/2004GL020159

Petiau, G. (2000). Second Generation of Lead-lead Chloride Electrodes for Geophysical Applications. *Pure and Applied Geophysics*, *157*(3), 357–382. https://doi.org/10.1007/s000240050004

Pirajno, F. (2007). Mantle plumes, associated intraplate tectono-magmatic processes and ore systems. *Episodes*, *30*(1), 6.

Pommier, A., & Le-Trong, E. (2011). “SIGMELTS”: A web portal for electrical conductivity calculations in geosciences. *Computers & Geosciences*, *37*(9), 1450–1459. https://doi.org/10.1016/j.cageo.2011.01.002

Pridmore, D. F., & Shuey, R. T. (1976). The electrical resistivity of galena, pyrite, and chalcopyrite. *American Mineralogist*, *61*(3–4), 248–259.

Primdahl, F. (1979). The fluxgate magnetometer. *Journal of Physics E: Scientific Instruments*, *12*(4), 241–253. https://doi.org/10.1088/0022-3735/12/4/001

Pritchard, M. E., Silva, S. L. de, Michelfelder, G., Zandt, G., McNutt, S. R., Gottsmann, J., et al. (2018). Synthesis: PLUTONS: Investigating the relationship between pluton growth and volcanism in the Central Andes. *Geosphere*, *14*(3), 954–982. https://doi.org/10.1130/GES01578.1

Pronenko, V., & Korepanov, V. (2009). Induction coil magnetometers - a review (Vol. 11, p. 1381). Presented at the EGU General Assembly Conference Abstracts, Vienna, Austria. Retrieved from http://adsabs.harvard.edu/abs/2009EGUGA..11.1381P

Richards, M. A., Duncan, R. A., & Courtillot, V. E. (1989). Flood Basalts and Hot-Spot Tracks: Plume Heads and Tails. *Science*, *246*(4926), 103–107. https://doi.org/10.1126/science.246.4926.103

Richter, F. M. (1984). Regionalized models for the thermal evolution of the Earth. *Earth and Planetary Science Letters*, *68*(3), 471–484. https://doi.org/10.1016/0012-821X(84)90131-6

Ripka, P. (1992). Review of fluxgate sensors. *Sensors and Actuators A: Physical*, *33*(3), 129–141. https://doi.org/10.1016/0924-4247(92)80159-Z

Ripka, P. (2003). Advances in fluxgate sensors. *Sensors and Actuators A: Physical*, *106*(1), 8–14. https://doi.org/10.1016/S0924-4247(03)00094-3

Roberts, C. W., Kucks, R. P., & Hill, P. L. (2008). *Oregon magnetic and gravity maps and data–A website for distribution of data* (U.S. Geological Survey Data Series No. Data Series 355). U.S. Geological Survey. Retrieved from https://pubs.usgs.gov/ds/355/

Roberts, J. J., Duba, A. G., Bonner, B. P., & Kasameyer, P. W. (2001). The effects of capillarity on electrical resistivity during boiling in metashale from scientific corehole SB-15-D, The Geysers, California, USA. *Geothermics*, *30*(2), 235–254. https://doi.org/10.1016/S0375-6505(00)00052-3

Robertson, K., Heinson, G., & Thiel, S. (2016). Lithospheric reworking at the Proterozoic–Phanerozoic transition of Australia imaged using AusLAMP Magnetotelluric data. *Earth and Planetary Science Letters*, *452*, 27–35. https://doi.org/10.1016/j.epsl.2016.07.036

Rodi, W., & Mackie, R. L. (2001). Nonlinear conjugate gradients algorithm for 2-D magnetotelluric inversion. *GEOPHYSICS*, *66*(1), 174–187. https://doi.org/10.1190/1.1444893

Rust, A. C., & Cashman, K. V. (2007). Multiple origins of obsidian pyroclasts and implications for changes in the dynamics of the 1300 B.P. eruption of Newberry Volcano, USA. *Bulletin of Volcanology*, *69*(8), 825–845. https://doi.org/10.1007/s00445-006-0111-4

Ryan, W.B.F., Carbotte, S. M., Coplian, J. O., O'Hara, S., Melkonian, A., Arko, R., et al. (2009). Global Multi-Resolution Topography synthesis. *Geochemistry, Geophysics, Geosystems*, *10*(Q03014). https://doi.org/doi:10.1029/2008GC002332.

Ryan, William B. F., Carbotte, S. M., Coplan, J. O., O'Hara, S., Melkonian, A., Arko, R., et al. (2009). Global Multi-Resolution Topography synthesis. *Geochemistry, Geophysics, Geosystems*, *10*(3). https://doi.org/10.1029/2008GC002332

Sammel, E. A. (1981). Results of test drilling at Newberry Volcano, Oregon. *Geothermal Resources Council Bulletin*, 3–8.

Sammel, E. A., & Craig, R. W. (1983). *Hydrology of the Newberry Volcano caldera, Oregon* (USGS Numbered Series No. 83–4091). U.S. Geological Survey,. Retrieved from http://pubs.er.usgs.gov/publication/wri834091

Sammel, E. A., Ingebritsen, S. E., & Mariner, R. H. (1988). The hydrothermal system at Newberry Volcano, Oregon. *Journal of Geophysical Research: Solid Earth*, *93*(B9), 10149–10162. https://doi.org/10.1029/JB093iB09p10149

Sasaki, Y. (2004). Three-dimensional inversion of static-shifted magnetotelluric data. *Earth, Planets and Space*, *56*(2), 239–248. https://doi.org/10.1186/BF03353406

Schneider, D. A., Bickford, M. E., Cannon, W. F., Schulz, K. J., & Hamilton, M. A. (2002). Age of volcanic rocks and syndepositional iron formations, Marquette Range Supergroup: implications for the tectonic setting of Paleoproterozoic iron formations of the Lake Superior region. *Canadian Journal of Earth Sciences*, *39*(6), 999–1012. https://doi.org/10.1139/e02-016

Schock, R. N., Duba, A. G., & Shankland, T. J. (1989). Electrical conduction in olivine. *Journal of Geophysical Research: Solid Earth*, *94*(B5), 5829–5839. https://doi.org/10.1029/JB094iB05p05829

Schultz, A., Booker, J., & Larsen, J. (1987). Lake bottom magnetotellurics. *Journal of Geophysical Research: Solid Earth*, *92*(B10), 10639–10649. https://doi.org/10.1029/JB092iB10p10639

Schultz, A., Kurtz, R. D., Chave, A. D., & Jones, A. G. (1993). Conductivity discontinuities in the upper mantle beneath a stable craton. *Geophysical Research Letters*, *20*(24), 2941–2944. https://doi.org/10.1029/93GL02833

Schultz, A., Egbert, G. D., Kelbert, A., Peery, T., Clote, V., Fry, B., et al. (2006). USArray TA Magnetotelluric Transfer Functions. https://doi.org/10.17611/DP/EMTF/USARRAY/TA

Schultz, A., Bowles-Martinez, E., Key, K., Livelybrooks, D., Bedrosian, P. A., Egbert, G. D., & Wannamaker, P. E. (2014). Magnetotelluric investigations of convergent margins and of incipient rifting: preliminary results from the EarthScope MT Transportable Array and MT FlexArray deployments in Cascadia and in the North American mid-continent region. In *Proceedings*. San Francisco, California, USA: American Geophysical Union.

Schultz, A., Bennington, N., & Bowles-Martinez, E. (2018). Joint MT and seismic imaging of Yellowstone supervolcano - connections between deeper mantle melt sources and shallow hydrothermal expressions from wideband MT array data collected in 2017. Presented at the 24th Electromagnetic Induction Workshop, Helsingør, Denmark.

Schulz, K. J., & Cannon, W. F. (2007). The Penokean orogeny in the Lake Superior region. *Precambrian Research*, *157*(1–4), 4–25. https://doi.org/10.1016/j.precamres.2007.02.022

Selway, K. (2014). On the Causes of Electrical Conductivity Anomalies in Tectonically Stable Lithosphere. *Surveys in Geophysics*, *35*(1), 219–257. https://doi.org/10.1007/s10712-013-9235-1

Sen, P., Scala, C., & Cohen, M. (1981). A self-similar model for sedimentary rocks with application to the dielectric constant of fused glass beads. *GEOPHYSICS*, *46*(5), 781–795. https://doi.org/10.1190/1.1441215

Sharp, W. E. (1969). Melting curves of sphalerite, galena, and pyrrhotite and the decomposition curve of pyrite between 30 and 65 kilobars. *Journal of Geophysical Research*, *74*(6), 1645–1652. https://doi.org/10.1029/JB074i006p01645

Shea, M. A., & Smart, D. F. (2006). Compendium of the eight articles on the “Carrington Event” attributed to or written by Elias Loomis in the American Journal of Science, 1859–1861. *Advances in Space Research*, *38*(2), 313–385. https://doi.org/10.1016/j.asr.2006.07.005

Shirey, S. B. (1997). Re-Os isotopic compositions of Midcontinent rift system picrites: implications for plume-lithosphere interaction and enriched mantle sources. *Canadian Journal of Earth Sciences*, *34*(4), 489–503.

Shirey, S. B., Berg, J. H., Carlson, R. W., & others. (1994). Temporal changes in the sources of flood basalts: isotopic and trace element evidence from the 1100 Ma old Keweenawan Mamainse Point Formation, Ontario, Canada. *Geochimica et Cosmochimica Acta*, *58*(20), 4475–4490.

Shreve, R. L., & Cloos, M. (1986). Dynamics of sediment subduction, melange formation, and prism accretion. *Journal of Geophysical Research: Solid Earth*, *91*(B10), 10229–10245. https://doi.org/10.1029/JB091iB10p10229

Silverman, S. M. (2006). Comparison of the aurora of September 1/2, 1859 with other great auroras. *Advances in Space Research*, *38*(2), 136–144. https://doi.org/10.1016/j.asr.2005.03.157

Simpson, F., & Bahr, K. (2005). *Practical Magnetotellurics*. New York: Cambridge University Press.

Siripunvaraporn, W., Egbert, G. D., Lenbury, Y., & Uyeshima, M. (2005). Three-dimensional magnetotelluric inversion: data-space method. *Physics of the Earth and Planetary Interiors*, *150*(1), 3–14. https://doi.org/10.1016/j.pepi.2004.08.023

Smith, J. (1996). Conservative modeling of 3-D electromagnetic fields, Part I: Properties and error analysis. *GEOPHYSICS*, *61*(5), 1308–1318. https://doi.org/10.1190/1.1444054

Spielman, P. B., & Finger, J. T. (1998). Well test results of exploration drilling at Newberry Crater, Oregon in 1995. In *Proceedings, Twenty-third Workshop on Geothermal Reservoir Engineering* (p. 6). Stanford, California, USA.

Stachel, T., & Harris, J. W. (2008). The origin of cratonic diamonds — Constraints from mineral inclusions. *Ore Geology Reviews*, *34*(1), 5–32. https://doi.org/10.1016/j.oregeorev.2007.05.002

Stevens, K., & McNeice, G. (1998). On the detection of Ni?Cu Ore hosting structures in the Sudbury Igneous Complex using the Magnetotelluric Method. In *SEG Technical Program Expanded Abstracts 1998* (Vols. 1–0, pp. 751–755). Society of Exploration Geophysicists. https://doi.org/10.1190/1.1820581

Storey, B.C., & Kyle, P. R. (1997). An active mantle mechanism for Gondwana breakup. *South African Journal of Geology*, *100*(4), 283–290.

Storey, Bryan C. (1995). The role of mantle plumes in continental breakup: case histories from Gondwanaland. *Nature*, *377*(6547), 301. https://doi.org/10.1038/377301a0

Sutarno, D. (2005). Development of Robust Magnetotelluric Impedance Estimation: a Review. *Indonesian Journal of Physics*, *16*(3), 11.

Swain, G., Barovich, K., Hand, M., Ferris, G., & Schwarz, M. (2008). Petrogenesis of the St Peter Suite, southern Australia: Arc magmatism and Proterozoic crustal growth of the South Australian Craton. *Precambrian Research*, *1–4*(166), 283–296. https://doi.org/10.1016/j.precamres.2007.07.028

Swanberg, C. A., & Combs, J. (1986). Geothermal drilling in the Cascade Range: Preliminary results from a 1387-m core hole, Newberry Volcano, Oregon. *Eos, Transactions American Geophysical Union*, *67*(29), 578–580. https://doi.org/10.1029/EO067i029p00578

Swanberg, C. A., Walkey, W. C., & Combs, J. (1988). Core hole drilling and the “rain curtain” phenomenon at Newberry Volcano, Oregon. *Journal of Geophysical Research: Solid Earth*, *93*(B9), 10163–10173. https://doi.org/10.1029/JB093iB09p10163

Swanson-Hysell, N. L., Burgess, S. D., Maloof, A. C., & Bowring, S. A. (2014). Magmatic activity and plate motion during the latent stage of Midcontinent Rift development. *Geology*, *42*(6), 475–478. https://doi.org/10.1130/G35271.1

Thiel, E. (1956). Correlation of gravity anomalies with the Keweenawan geology of Wisconsin and Minnesota. *Geological Society of America Bulletin*, *67*(8), 1079–1100.

Thiel, S., & Heinson, G. (2013). Electrical conductors in Archean mantle—Result of plume interaction? *Geophysical Research Letters*, *40*(12), 2947–2952. https://doi.org/10.1002/grl.50486

Thiel, S., Heinson, G., Reid, A., & Robertson, K. (2016). Insights into Lithospheric Architecture, Fertilisation and Fluid Pathways from AusLAMP MT. *Australian Society of Exploration Geophysicists Extended Abstracts*, *2016*(1), 1–6. https://doi.org/10.1071/aseg2016ab261

Tietze, K., Ritter, O., & Egbert, G. D. (2015). 3-D joint inversion of the magnetotelluric phase tensor and vertical magnetic transfer functions. *Geophysical Journal International*, *203*(2), 1128–1148. https://doi.org/10.1093/gji/ggv347

Tikhonov, A. N. (1950). On determining electrical characteristics of the deep layers of the Earth's crust. *Doklady*, *73*(2), 295–297.

Tréhu, A., Morel-à-l'Huissier, P., Meyer, R., Hajnal, Z., Karl, J., Mereu, R., et al. (1991). Imaging the midcontinent rift beneath Lake Superior using large aperture seismic data. *Geophysical Research Letters*, *18*(4), 625–628. https://doi.org/10.1029/91GL00826

Tumanski, S. (2007). Induction coil sensors—a review. *Measurement Science and Technology*, *18*(3), R31. https://doi.org/10.1088/0957-0233/18/3/R01

Tuncer, V., Unsworth, M. J., Siripunvaraporn, W., & Craven, J. A. (2006). Exploration for unconformity-type uranium deposits with audiomagnetotelluric data: A case study from the McArthur River mine, Saskatchewan, CanadaUranium exploration with AMT. *Geophysics*, *71*(6), B201–B209. https://doi.org/10.1190/1.2348780

Turcotte, D. L., & Emerman, S. H. (1983). Mechanisms of active and passive rifting. *Tectonophysics*, *94*(1), 39–50. https://doi.org/10.1016/0040-1951(83)90008-2

Tuttle, O. F., & Bowen, N. . (1958). *Origin of Granite in the Light of Experimental Studies in the System NaAlSi3O8–KAlSi3O8–SiO2–H2O* (Vol. 74). Geological Society of America. https://doi.org/10.1130/MEM74

Tyburczy, J. A., & Fisler, D. K. (1995). Electrical Properties of Minerals and Melts. In *Mineral Physics & Crystallography: A Handbook of Physical Constants* (pp. 185–208). American Geophysical Union (AGU). https://doi.org/10.1029/RF002p0185

Utada, H., & Munekane, H. (2000). On galvanic distortion of regional 3-D MT impedances On galvanic distortion of regional three-dimensional magnetotelluric impedances. *Geophysical Journal International*, *140*(2), 385–398. https://doi.org/10.1046/j.1365-246x.2000.00014.x

Van Schmus, W. R., & Hinze, W. J. (1985). The midcontinent rift system. *Annual Review of Earth and Planetary Sciences*, *13*, 345.

Vervoort, J. D., Wirth, K., Kennedy, B., Sandland, T., & Harpp, K. S. (2007). The magmatic evolution of the Midcontinent rift: New geochronologic and geochemical evidence from felsic magmatism. *Precambrian Research*, *157*(1–4), 235–268. https://doi.org/10.1016/j.precamres.2007.02.019

Vincent, P., Bowles-Martinez, E., & Schultz, A. (2018). *A Multisensor Plume Monitoring Schema for Carbon Sequestration Sites in Subsurface Engineered-Natural Systems* (NETL Technical Report Series No. NETL-TRS-2-2018) (p. 48). Albany, Oregon, USA: U.S. Department of Energy, National Energy Technology Laboratory.

Vozoff, K. (1991). 8. The Magnetotelluric Method. In *Electromagnetic Methods in Applied Geophysics* (Vols. 1–0, pp. 641–712). Society of Exploration Geophysicists. https://doi.org/10.1190/1.9781560802686.ch8

Waibel, A. F., Frone, Z. S., & Blackwell, D. D. (2014). *Geothermal Exploration of Newberry Volcano, Oregon* (No. DOE-Davenport-0002833). Davenport Newberry, Stamford, CT (United States). https://doi.org/10.2172/1182676

Wannamaker, P., Hohmann, G., & SanFilipo, W. (1984). Electromagnetic modeling of three-dimensional bodies in layered earths using integral equations. *GEOPHYSICS*, *49*(1), 60–74. https://doi.org/10.1190/1.1441562

Wannamaker, P. E., Stodt, J. A., & Olsen, S. L. (1996). Dormant state of rifting below the Byrd Subglacial Basin, West Antarctica, implied by magnetotelluric (MT) profiling. *Geophysical Research Letters*, *23*(21), 2983–2986. https://doi.org/10.1029/96GL02887

Wannamaker, P. E., Stodt, J. A., Pellerin, L., Olsen, S. L., & Hall, D. B. (2004). Structure and thermal regime beneath the South Pole region, East Antarctica, from magnetotelluric measurements. *Geophysical Journal International*, *157*(1), 36–54. https://doi.org/10.1111/j.1365-246X.2004.02156.x

Ward, S., & Hohmann, G. (1988). 4. Electromagnetic Theory for Geophysical Applications. In *Electromagnetic Methods in Applied Geophysics* (Vols. 1–0, pp. 130–311). Society of Exploration Geophysicists. https://doi.org/10.1190/1.9781560802631.ch4

Weidelt, P. (1985). Construction of conducance bounds from magnetotelluric impedances. *Geophysics*, *57*, 191–206.

White, R., & McKenzie, D. (1989). Magmatism at rift zones: the generation of volcanic continental margins and flood basalts. *Journal of Geophysical Research: Solid Earth*, *94*(B6), 7685–7729.

White, R. S. (1992). Crustal structure and magmatism of North Atlantic continental margins. *Journal of the Geological Society*, *149*(5), 841–854.

White, R. S., & McKenzie, D. (1995). Mantle plumes and flood basalts. *Journal of Geophysical Research: Solid Earth*, *100*(B9), 17543–17585.

White, Robert S. (1997). Mantle temperature and lithospheric thinning beneath the Midcontinent rift system: evidence from magmatism and subsidence. *Canadian Journal of Earth Sciences*, *34*(4), 464–475. https://doi.org/10.1139/e17-038

White, Robert S., Spence, G. D., Fowler, S. R., McKenzie, D. P., & Westbrook, G. K. (1987). Magmatism at rifted continental margins. *Nature*, *330*, 439–444.

Whitmeyer, S. J., & Karlstrom, K. E. (2007). Tectonic model for the Proterozoic growth of North America. *Geosphere*, *3*(4), 220–259.

Wunderman, R. L., Wannamaker, P. E., & Young, C. T. (2018). Architecture of the hidden Penokean terrane suture and Midcontinent rift system overprint in eastern Minnesota and western Wisconsin from magnetotelluric profiling. *Lithosphere*, *10*(2), 291–300. https://doi.org/10.1130/L716.1

Yang, B., Egbert, G. D., Kelbert, A., & Meqbel, N. M. (2015). Three-dimensional electrical resistivity of the north-central USA from EarthScope long period magnetotelluric data. *Earth and Planetary Science Letters*, *422*, 87–93. https://doi.org/10.1016/j.epsl.2015.04.006

Yee, K. (1966). Numerical solution of initial boundary value problems involving maxwell's equations in isotropic media. *IEEE Transactions on Antennas and Propagation*, *14*(3), 302–307. https://doi.org/10.1109/TAP.1966.1138693

Yoshino, T. (2010). Laboratory Electrical Conductivity Measurement of Mantle Minerals. *Surveys in Geophysics*, *31*(2), 163–206. https://doi.org/10.1007/s10712-009-9084-0

Zhdanov, M. S. (2017). *Foundations of Geophysical Electromagnetic Theory and Methods* (2nd ed.). Elsevier. https://doi.org/10.1016/C2014-0-02307-6

Zhdanov, M. S., Smith, R. B., Gribenko, A., Cuma, M., & Green, M. (2011). Three-dimensional inversion of large-scale EarthScope magnetotelluric data based on the integral equation method: Geoelectrical imaging of the Yellowstone conductive mantle plume. *Geophysical Research Letters*, *38*(8), L08307. https://doi.org/10.1029/2011GL046953

Zucca, J. J., & Evans, J. R. (1992). Active high-resolution compressional wave attenuation tomography at Newberry Volcano, Central Cascade Range. *Journal of Geophysical Research: Solid Earth*, *97*(B7), 11047–11055. https://doi.org/10.1029/92JB00492

Appendix A: Newberry Volcano data and model fits

This appendix is available digitally through OSU archives. It contains the data for the 195 stations used in the Newberry inversion presented as plots of apparent resistivity and phase for the off-diagonal components of the impedance tensor (Z_{xy} and Z_{yx}). The forward response of our final model is shown on each plot as a solid line. A map is given to provide station locations.

Appendix B: Midcontinent data and model fits

This appendix is available digitally through OSU archives. It contains the data for 241 stations used in the Midcontinent inversion presented as plots of apparent resistivity and phase for the off-diagonal components of the impedance tensor (Z_{xy} and Z_{yx}). The forward response of our final model is shown on each plot as a solid line. A map is given to provide station locations.